
Dissertation zur Erlangung des Doktorgrades
der Fakultät für Chemie und Pharmazie
der Ludwig-Maximilians-Universität München

Investigation into the feasibility of a DNA based radiosensitive device

Florian Thomas Heimbach

aus

Bamberg, Deutschland

2021

Erklärung

Diese Dissertation wurde im Sinne von § 7 der Promotionsordnung vom 28. November 2011 von Herrn Philip Tinnefeld betreut.

Eidesstattliche Versicherung

Diese Dissertation wurde eigenständig und ohne unerlaubte Hilfe erarbeitet.

Braunschweig, 17.03.2021

Florian Heimbach
.....

Dissertation eingereicht am	30.03.2021
1. Gutachterin / 1. Gutachter:	Prof. Dr. Philip Tinnefeld
2. Gutachterin / 2. Gutachter:	Prof. Dr. Don C. Lamb
Mündliche Prüfung am	18.05.2021

Table of Contents

Summary	1
Zusammenfassung	3
1 Introduction	5
2 Theoretical Background	9
2.1 The DNA Molecule	9
2.1.1 DNA Molecular Structure	9
2.1.2 DNA Radiation Lesions	11
2.2 Charge Transport in DNA	13
2.2.1 Microhydration	14
2.2.2 Surface Interaction	15
2.2.3 Radiation lesions	16
2.2.4 DNA Electrode Linking	17
2.2.5 DNA Four-Way Junction	19

Table of Contents

2.3	Electrokinetic Phenomena	20
2.3.1	Dielectrophoresis	20
2.3.2	AC Electro-osmosis	23
2.3.3	Electrothermal Fluid Flow	26
2.4	Molecular Dynamics	29
2.4.1	Force Field	30
2.4.2	Motion and Timestep	31
2.4.3	Thermodynamics	32
3	Experimental Methods	35
3.1	DNA Origami Technique	35
3.2	DNA Origami Structure Trapping	37
3.2.1	Nanoelectrodes	37
3.2.2	DEP Trapping	38
3.2.3	DEP Trapping Recipe	39
3.3	λ -DNA Bridge Preparation	41
3.3.1	Microelectrodes	42
3.3.2	Trapping Recipe	42
3.4	Electrical Impedance Spectroscopy	44
3.4.1	Lock-in Amplifier	44
3.4.2	Measurement Setup	45
4	λ-DNA Experiments	53
4.1	Irradiation with Electrons	55
4.1.1	Setup	55
4.1.2	Results	56
4.2	Irradiation with Alpha-Particles	56
4.2.1	Am-241 Source	56

4.2.2 Microbeam Facility	61
4.3 Conclusions	62
5 MD Simulation of microhydrated DNA Bundles	65
5.1 Setup	65
5.2 Results	67
5.3 Conclusions	73
6 DNA Origami Structure Experiments	75
6.1 DNA Origami Structure Trapping	77
6.1.1 DNA-Gold linkers	78
6.1.2 DNA Origami Structure with Protective Coating	80
6.1.3 DEP with a series resistor	82
6.1.4 DNA overlapping with Gold Nanostructures	85
6.2 Conclusions	86
7 Conclusions & Outlook	91
Appendix	95
A DNA Origami Structure Designs	97
B MD Simulation of microhydrated DNA Bundles	101
Danksagung	129

List of Abbreviations

4WJ	DNA four-way junction / Holliday junction
A	Adenine
AC	Alternating Current
AFM	Atomic Force Microscopy
bp	Base Pair
C	Cytosine
CI	Confidence Interval
CL	Cross Link
DC	Direct Current
DEP	Dielectrophoresis
DSB	Double Strand Break
dsDNA	Double Stranded DNA
EDL	Electrical Double Layer
EO	Electro-osmosis
ESD	Electrostatic Discharge
FF	Force Field
G	Guanine
MD	Molecular Dynamics
NPT	Isothermal-Isobaric Ensemble
NVT	Canonical Ensemble

List of Abbreviations

PLL	Poly-L-Lysine
QC	Quantum Chemistry
QM/MM	quantum mechanics / molecular mechanics
RMS	Root Mean Square
ROS	Reactive Oxygen Species
SAM	Self Assembled Monolayer
SB	DNA Strand Break
SEM	Scanning Electron Microscopy
SPICE	Simulation Program with Integrated Circuit Emphasis
SSB	Single Strand Break
ssDNA	Single Stranded DNA
STX	Immobile Stacked-X
T	Thymine
TCEP	Tris(2-Carboxyethyl)phosphine
TEM	Transmission Electron Microscopy
vdW	van der Waals

Summary

In this work, the application of deoxyribonucleic acid (DNA) as a radiosensitive detector material is investigated. The aim is to bridge a measurable physical quantity with the severity of radiation damages on the biochemical stage. Radiation damages, which are expressed in alterations of the molecular structure of the DNA, can influence the charge transport properties of the molecule. The electrical conductivity is therefore a measure for the magnitude of the radiation damage.

DNA samples consist of a substrate material with gold electrodes of nano- or microscale dimensions and of DNA molecules contacted between these electrodes. Experiments were performed with two types of DNA samples. λ -DNA molecules of several micrometer length suspended in air and single DNA origami structures trapped via dielectrophoresis.

λ -DNA samples were provided by San Diego State University. The samples are expected to have non-uniform conductivity values, due to differences in number and alignment of the DNA strands. Therefore, an exact quantitative analysis of the radiation effects might not be possible. Nevertheless, the effects of different radiation qualities were studied on these samples. Changes of conductivity were monitored in situ during irradiation. The experiments showed that the conductivity of DNA is indeed sensitive to radiation. For the application as a detector material, a quantitative relation between the amount of DNA damage and the change in conductivity needs to be established.

Single DNA origami structures can be electrically contacted using dielectrophoretic trapping. Experiments were carried out to investigate whether samples can be produced which retain ohmic conductivity in dry conditions. This investigation was accompanied by molecular dynamics simulations of microhydrated, multilayered DNA

Summary

molecules. These can give insight under which conditions the DNA molecules keep their regular helical structures. It was found that tightly packed multilayered structures were indeed much more stable than individual or loosely packed strands. However, stable helical structures as in the case of fully hydrated states, were still only achieved for very high hydration levels in the simulation. To further increase the resilience of the DNA origami structures, they were covered with a layer of poly-L-lysine (PLL). It has been shown in studies that PLL coatings stabilize DNA origami structures against buffers of low salt concentrations. Experiments with these samples showed ohmic conductivity in dry conditions. The measured resistance values were in the range of several megaohm. A frequently observed phenomenon was the local destruction of the substrate material and electrodes after DEP trapping. The destruction was the result of high electrical currents. This indicates that the DNA origami structures can possess even higher values of electrical conductivity. Therefore, experiments with current limitation during DEP trapping should be the subject of future experiments. The subsequent step would be to test the influence of different radiation qualities and doses on the conductivity of these samples.

Zusammenfassung

In dieser Arbeit wird die Anwendung von Desoxyribonukleinsäure als strahlensensitives Detektormaterial untersucht. Ziel ist es eine Verbindung zwischen einer messbaren physikalischen Größe und dem Ausmaß des Strahlenschadens auf der biochemischen Ebene zu finden. Strahlenschäden, welche sich durch Änderungen der molekularen Struktur der DNA äußern, können die Ladungstransporteigenschaften von DNA-Molekülen verändern. Die elektrische Leitfähigkeit kann daher als Maßstab für die Größe des Strahlenschadens genutzt werden.

DNA-Proben bestehen aus einem Substrat mit Nano/Mikrometer messenden Gold-elektroden und DNA-Molekülen, welche zwischen den Elektroden kontaktiert sind. Es wurden Experimente mit zwei Arten von DNA-Proben durchgeführt. Diese sind λ -DNA Moleküle von mehreren Mikrometern Länge, frei hängend kontaktiert, und einzelnen DNA-Origami Strukturen, welche mittels Dielektrophorese kontaktiert wurden.

Die λ -DNA Proben wurden von der San Diego State University bezogen. Diese Proben haben meist uneinheitliche Leitfähigkeitswerte, da sie sich in der Anzahl und Ausrichtung der DNA-Moleküle unterscheiden können. Hierdurch ist eine quantitative Analyse der Strahleneffekte wahrscheinlich nicht möglich. Gleichwohl wurden die Effekte verschiedener Strahlenqualitäten an den DNA-Proben untersucht. Die Veränderung der Leitfähigkeit wurde in situ während der Bestrahlung gemessen. Die Versuche zeigen, dass die Leitfähigkeit von DNA tatsächlich sensitiv bezüglich Strahlung ist. Damit eine Anwendung als Detektormaterial möglich ist, muss noch eine quantitative Verbindung zwischen dem Ausmaß des DNA-Schadens und der Änderung der Leitfähigkeit gefunden werden.

Einzelne DNA-Origami Strukturen können per dielektrophoretischem Einfang elektrisch kontaktiert werden. Es wurden Versuche durchgeführt, um zu untersuchen, ob so Proben hergestellt werden können, die in einer trockenen Umgebung eine ohmsche Leitfähigkeit aufweisen. Diese Untersuchungen wurden durch Molekulardynamik-Simulationen von mikrohydrierten, mehrlagigen DNA-Molekülen begleitet. Diese Simulationsrechnungen können helfen einen Einblick zu gewinnen, unter welchen Bedingungen die DNA-Moleküle ihre regelmäßige helikale Struktur behalten. Es wurde festgestellt, dass dicht gepackte, mehrlagige Strukturen tatsächlich deutlich stabiler waren als einzelne, oder lose gepackte Stränge. Jedoch wurden eine stabile helikale Struktur, wie sie im voll hydrierten Zustand auftritt, auch hier nur im Falle sehr hoher Hydrierungsgrade erreicht. Um die Widerstandsfähigkeit der DNA-Origami Strukturen weiter zu verbessern wurden diese mit einer Schicht aus poly-L-Lysin umhüllt. Es wurde in Studien gezeigt, dass PLL Schutzschichten DNA-Origami Strukturen in Pufferlösungen mit niedrigem Salzgehalt stabilisieren. Diese Proben zeigten in unseren Experimenten ohmsche Leitfähigkeiten in trockener Umgebung. Die gemessenen elektrischen Widerstandswerte bewegten sich im Bereich einiger Megaohm. Ein häufig beobachtetes Phänomen war die lokale Zerstörung von Substrat und Elektroden nach dem DEP Einfang. Diese wurde durch hohe elektrische Ströme hervorgerufen und weist darauf hin, dass die DNA-Origami Strukturen sogar noch höhere elektrische Leitfähigkeiten besitzen könnten. Daher soll in folgenden Experimenten den DEP Einfang dieser Strukturen mit begrenzter Stromstärke untersucht werden. Der darauffolgende Schritt wäre den Einfluss verschiedener Strahlenqualitäten auf die Leitfähigkeit dieser Proben zu testen.

Chapter 1

Introduction

Monitoring radiation damage offers unique challenges in the field of physics, chemistry and biology alike. This is due to the complex processes involved in radiation damage. The absorbed dose is a purely physical quantity and therefore more information on the biological level are required to determine the harmfulness of the exposure. To account for the biological effect of different radiation qualities, radiation weighting factors are introduced[1].

Radiobiological studies indicate that the harmfulness of a radiation type is related to its efficiency to produce double strand breaks in DNA[2]. DNA damages can occur due to endogenous as well as external effects, with ionizing radiation being the main source of external damages. Since DNA is the primary radiation target regarding biological damages, a new concept for radiation detection using DNA as detector material is investigated in this work. The physical quantity to be measured is the electrical conductivity of the DNA, which may provide information on the molecular structure of the DNA.

The electrical conductivity of DNA became the topic of many scientific discussions around the turn of the millennium. There was some evidence that the double helical DNA is a suitable medium for electron and hole transport[3, 4, 5]. The mechanism for long range charge transport is believed be a combination of tunneling and hopping[6]. In the DNA helix, tight stacking of the base pairs results in delocalized π orbitals,

which provide an efficient way for charge transport. This π stacking is very sensitive to the sequence-dependent conformation and dynamics of the DNA molecule. If base stacking becomes irregular, charge transport rates will decrease significantly.

The goal of this work is to measure the degree of radiation damage in the DNA molecule. As stated above, the regular stacking of the base pairs is essential for the charge transport. Ionizing radiation can damage the molecular structure of DNA which can lead to the disruption of π stacking and, therefore, to a decrease of charge transport rates. Complex strand breaks like double strand breaks are of special interest due to their cytotoxicity[2]. However, other radiation damages such as cross links can also affect charge transport rates[7].

For the use of a DNA based radiation detector it is important that the DNA structure was intact before irradiation. Otherwise, this initial bottleneck in charge transport may overshadow the effects of the radiation exposure. The investigation of suitable DNA samples and preparation methods are therefore an integral part of this thesis.

Direct conductivity measurements of DNA under dry conditions yielded results ranging from insulating[8, 9] to semiconducting[4] and ohmic conducting behavior[5]. The diversity of these results can be traced back to varying experimental conditions. In its natural environment, DNA is always in a liquid solution. Conductivity measurements, however, require a dry environment, to avoid a bias of the measurement due to the conductivity of the solution. Experimental factors such as DNA alignment, sequence and environment may also influence the experimental results.

Two methods showed promising results in producing DNA samples with ohmic characteristics. Dielectrophoretic trapping was applied successfully to DNA origami structures by Shen et al. to produce single molecular samples[10]. They discovered that DNA trapping can result in the formation of 'nanocanyons'. These nanocanyons can be produced by high electric currents eroding the electrodes and underlying substrate material. The erosion only takes place on the scale of the DNA origami structure size. This indicates that high rates of charge transport occur in the DNA origami structures.

A second approach for the fabrication of DNA samples was developed by Kassegne et al.[11]. Here, λ -DNA molecules were attached between electrode pairs, which are separated from the substrate by a layer of photoresist. The photoresist layer is etched away, except underneath the electrodes, allowing the DNA to form a free hanging structure. Interaction with the substrate material, which can deform the DNA molecule[12], are therefore eliminated. A determination of the exact number of

DNA strands is difficult, as a visualization of the trapped DNA is at present not feasible. This is, however, detrimental for the production of samples with reproducible impedance characteristics.

The electrical contacts between the metal electrodes and the DNA molecule was established by means of thiol linkers. Experiments performed by other groups indicate that the implementation of thiol linkers enable much higher conductivity[11, 8]. Conventional thiol linkers attach the DNA backbone to the metal electrode. Experimental findings indicate that a direct linkage to the DNA base can promote the charge transport[13].

Another part of this thesis will be the irradiation of DNA samples. It needs to be considered that DNA conductivity is very sensitive to all kinds of environmental factors. To separate the irradiation effects from the environmental factors, a reference measurement with an unirradiated sample is required. An interesting subject of study will be how the DNA reacts to different radiation qualities.

Theoretical Background

This chapter covers a variety of background knowledge important for the understanding of this work. Especially, the DNA molecule and some of its properties will be discussed. The chapter also contains a brief overview of the basics of molecular dynamics simulations.

2.1 The DNA Molecule

DNA is a macromolecule found in almost every cell of living organisms. These molecules contain hereditary information encoded into their chemical structure and can therefore be considered as the very basic building block of life.

2.1.1 DNA Molecular Structure

DNA is a chain-like polymer, which forms a double helical structure under normal physiological conditions[14]. The helix is made up of two strands that hybridize. The strands are in turn made up of four different nucleotides. Each is composed of a phosphate group, a five-carbon sugar and one of four nucleobases. The phosphate group and sugar build up the so-called backbone of the DNA. The four nucleobases are adenine (A), cytosine (C), guanine (G) and thymine (T). Adjacent nucleotides

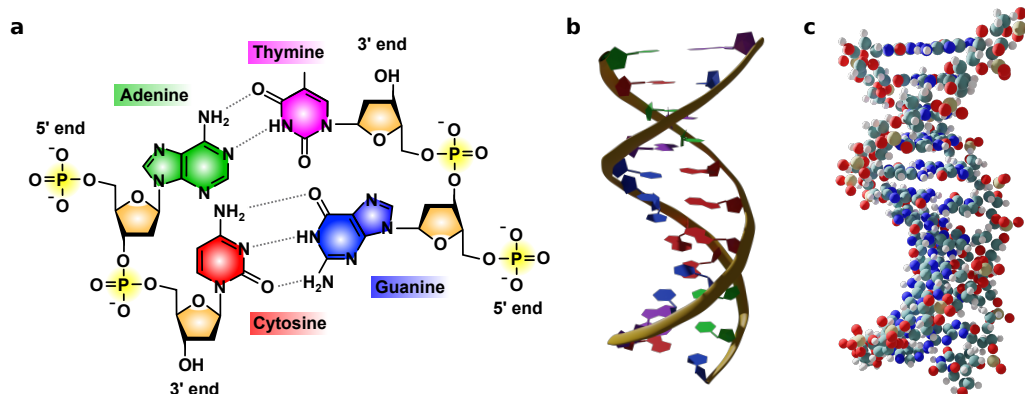


Figure 2.1: The molecular structure of the DNA. Image **a** depicts the basic components of the DNA as a skeletal formula. The helical form of a 12 bp B-DNA is shown in the images **b** and **c** as a ribbon diagram and as individual atoms, respectively.

are connected by a covalent bond between the sugar of one nucleotide and the phosphate of the next. This forms a polynucleotide strand called single stranded DNA (ssDNA). Two of these single strands can bind together, forming a double stranded DNA (dsDNA). The formation of a double strand follows specific patterns: adenine only binds to thymine and cytosine only to guanine. These pairs are also called Watson-Crick pairs or more generally base pairs (bp). Hydrogen bonds are formed between bases in Watson-Crick pairs (see figure 2.1). These have been generally accepted as the driving force for the formation of stable DNA double strands. In a recent paper however, evidence was reported that this is mainly caused by hydrophobic effects[15].

DNA is most commonly found in a right-handed helical conformation called B-DNA[16]. Other conformations include the also right-handed A-DNA and the left-handed Z-DNA. The conformation is influenced by several environmental conditions as well as by the DNA-sequence.

The geometrical structure of the DNA molecule can be described using so called helical parameters[17]. These parameters describe the geometry of the nucleobases. The nomenclature distinguishes between intra-base pair and inter-base pair parameters. The first group characterizes deviations from a planar arrangement within a pair of nucleobases. The second describes the orientation of two base-pairs stacked on top of each other. A selection of inter-base helical parameters is shown in figure 2.2.

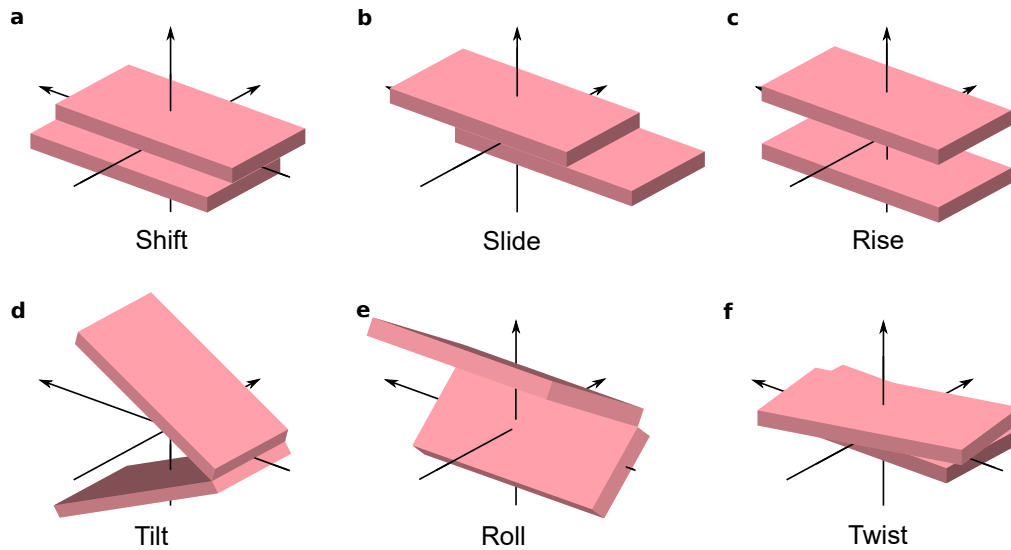


Figure 2.2: Schematic diagram of selected helical parameters. The parameters **a** shift, **b** slide, **c** rise, **d** tilt, **e** roll and **f** twist all belong to the inter-base pair category. They describe the stacking of two consecutive base pairs[18].

2.1.2 DNA Radiation Lesions

Due to its high energy, ionizing radiation can cause lesions in DNA molecules and alter their structure. In a cell, this can result in genetic instability, which may lead to genetic divergences or diseases such as cancer and other hereditary diseases. The majority of DNA damages are induced endogenously. These are rather homogeneously distributed. Radiation induced lesions are especially dangerous, because ionizing radiation has a much higher chance of producing clustered lesions.

The initial step of DNA damages caused by ionizing radiation is the physical energy dissipation. This takes place on very short timescales in the order of 10^{-16} seconds. The collision of particle, or electromagnetic radiation with molecules of matter can cause ionization, or excitation via energy transfer. The molecules, excited in the physical stage, are prone to chemical changes. Additional to these direct effects, there is a group of indirect effects. Here the primary radiation does not interact with the DNA molecule itself, but with the medium, mostly water, in its vicinity. This causes the creation of free reactive oxygen species (ROS), such as hydroxyl radicals, which can diffuse to the DNA molecule and affect it[19]. An illustration of direct and indirect action of radiation on DNA is shown in figure 2.3.

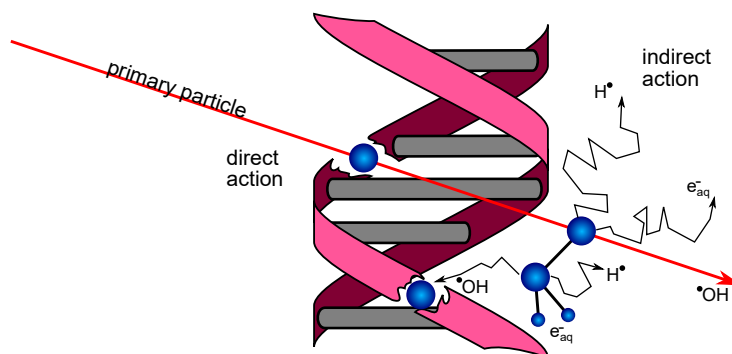


Figure 2.3: Direct and indirect action of radiation on DNA. Direct action includes all events of interaction between the primary particle or a secondary electron and the target. Indirect action comprises the interaction of free radicals produced via radiolysis of the surrounding water with the target.

DNA lesions include strand breaks (SB), crosslinks (CL) and base damages, or base modifications. The latter is also able to indirectly lead to strand breakage.

Damage to the sugar moiety can lead to damages such as abasic sites, or strand breaks in the DNA molecule[20]. At an abasic site, the DNA backbone is still intact with the base either totally removed, or only a fraction of the base remaining. Strand breaks are generally distinguished into single strand breaks (SSB) and double strand breaks (DSB). Both arise due to separation of the DNAs sugar phosphate backbone. A strand break is regarded a DSB when two SSBs occur on opposing strands, separated by not more than 10 base pairs. They are believed to be the most deleterious lesion induced by ionizing radiation. DSBs are also a characteristic of radiation since only few are produced by endogenous means[21, 22].

Under oxidative stress, nucleotides can bind together to form cross links. Interstrand CLs connect bases on different strands, whereas intrastrand CLs occur between bases on the same strand. Mostly, CLs are formed by crosslinking agents which possess two independently reactive groups within the same molecule. Ionizing radiation is also known to produce crosslinks, via ROS[23, 24]. Depending on the environment, this can also lead to crosslinks between DNA and protein molecules.

Direct or indirect interaction of radiation and a nucleoside can cause base damages. Excitation or ionization can trigger the base to undergo chemical changes, resulting in a variety of possible modified bases[25]. Unlike abasic sites, damaged bases still result in a stable double helical structure of the DNA[26, 27].

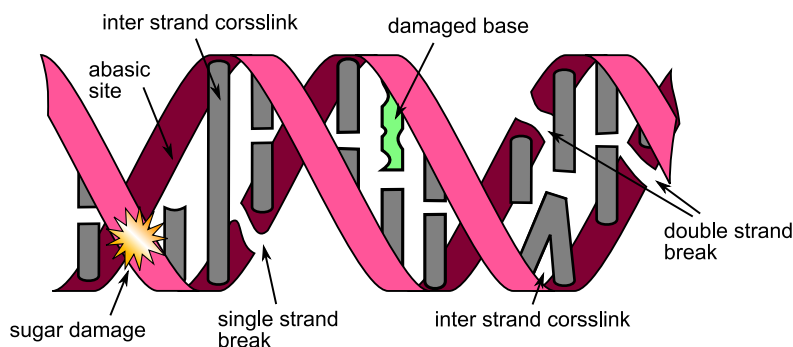


Figure 2.4: Schematic representation of different DNA lesions produced by ionizing radiation

2.2 Charge Transport in DNA

Already in 1953 it was discussed that DNA might be able to promote charge transport[28]. The proposed explanation was that the delocalized π -orbitals in the aromatic rings of adjacent bases can couple with each other in the direction of the helical axis. This so-called π -stacking or base-stacking lowers the band gap enough to allow charge transport along the helical axis. This effect, however, is very sensitive to the DNAs structure and dynamics.

Two theories for the charge transport through dsDNA were formulated: Superexchange, or coherent tunneling from donor to acceptor through the DNA bridge and charge hopping between discrete base orbitals[29]. Coherent tunneling works as a direct step mechanism. The charge transfer occurs through a series of base pairs in which nearly all the lowest unoccupied molecular orbitals are occupied. The charge transfer rate is exponentially dependent on the distance between donor and acceptor. Such a distance dependence was indeed examined for short oligonucleotides, regardless of the nucleotide sequence[30, 31]. For DNA strands longer than a few base pairs, however, it is extremely unlikely that superexchange is the main charge transport mechanism.

Charge transport seen over longer DNA molecules can be explained by charge hopping. The charge moves along the DNA strand through short tunneling steps between neighboring guanine nucleotides[6]. The charge localizes in a guanine radical $G^{\bullet+}$ since guanine has the lowest ionization potential among the DNA bases. The charge transport can be seen as a series of tunneling steps between guanine over AT

bases. Therefore, the charge transfer rate shows a much weaker, linear, dependence on the distance between donor and acceptor. This mechanism is, however, very sensitive to the DNA sequence. Long intervening tracks of AT between GC bases have a significant impact on charge transfer rates. It was found that charge transfer induced guanine oxidation decreases steeply with distance, for less than three TA bases between the guanine bases. When the guanine bases were separated by more than three bases however, the oxidation rate exhibited a more shallow distance dependence[32]. This suggests a mechanism shift from tunneling at short distances to a mechanism based on thermal hopping at long distances.

Regardless of how the charge transfer takes place, the consensus is that continuous base-stacking throughout a DNA duplex is important[33]. Reduced charge transfer rates are observed in DNA with perturbations to their helical structure, for instance in the form of mismatches[34, 35] or bulges[36]. On the other hand, abasic sites[37] or single-stranded overhangs[38] have been found to not prevent charge transfer, although a reduction of charge transfer rates might be possible. The influence of important environmental and structural effects on the charge transport properties will be discussed in more detail in the following subsections.

2.2.1 Microhydration

One major environmental factor is the hydration of the DNA. DNA, as found in the nucleus of eukaryotic cells, is surrounded by an aqueous solution. In its original physiological condition, DNA forms a stable double helix with continuous base stacking. Such a setup is, however, not feasible for conductivity measurements, due to the current flow through the solution. In air, the degree of hydration is correlated with the ambient air humidity. The number of water molecules N_w per DNA nucleobase can be expressed as

$$N_w = \frac{44RH}{(1 - RH)(1 + 19RH)} + N_0, \quad (2.1)$$

where RH is the ambient humidity[39, 40] and N_0 the number of water molecules in the 0th hydration layer. This layer consists of about 5 water molecules per nucleobase. This relationship was observed for humidity levels between 0 % and 80 % RH. Above 80 % RH, it is assumed that the DNA is practically completely surrounded by water.

Multiple experiments have been reported in the literature that investigate the effect of humidity on DNA conductivity[41, 42, 43, 44, 45]. The general agreement is that the conductivity increases with increasing humidity levels. However, this dependency does not follow a general rule. One major factor appears to be how the DNA molecules are assembled (e.g. monolayer, bundle, single molecule, ...). Conductivity of bundles of multiple DNA molecules did show a strong dependence with humidity[41]. At the same time, it was found that thick “ropes” of DNA do not change their conductivity with varying humidity[46].

In a study by Wolter et al.[47], the structure of short 7 bp oligonucleotides was simulated in a microhydrated state using a combined quantum mechanical and molecular mechanical approach. The simulation supported the experimental results. At low humidity levels, the DNA could not keep its helical structure. It was concluded that the decrease in conductivity results from structural irregularities in these conditions. This is in agreement with the recent discovery that a hydrophilic environment is crucial for the formation of dsDNA[15].

2.2.2 Surface Interaction

In many experiments DNA is either immobilized on a mica surface[44] or lies on a silicon oxide substrate[45]. The forces between DNA and surface can vary, dependent on the substrate material and treatment of the surface[48].

A. Yu. Kasumov et al.[12] found that λ -DNA immobilized on mica showed electrically insulating behavior. However, if a thin (about 0.5 nm) layer of discontinuous polymer film was first deposited on the surface, the DNA showed conductive behavior. Furthermore, the measured height of DNA on bare mica was 1 nm while the height on the treated surface was 2 nm. Their interpretation was that the deposition of the polymer film decreased hydrophilicity of mica and thus its interaction with DNA. This interaction resulted in a deformation of the DNA helix. The irregular stacking of base pairs due to this deformation caused the poor electrical conductivity. The same effect is to be expected for silicon oxide surfaces. Especially after cleaning with oxygen plasma, these surfaces have high hydrophilicity[49]. Free hanging DNA molecules do not suffer from the interaction between DNA and the substrate surface. This may also be the case for thick “ropes” of DNA[46]. It is assumed that the inner DNA helices in such an assembly keep their regular π -stacking.

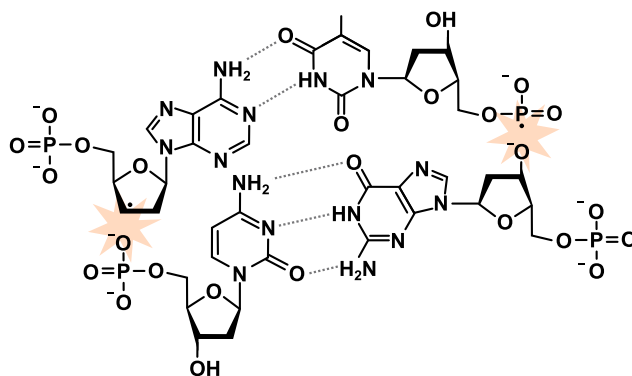


Figure 2.5: Two DNA strand breaks illustrated in skeletal formula. The depicted strand breaks are two possible outcomes from dissociative electron attachment of the phosphate group[54].

2.2.3 Radiation lesions

Strand Breaks

Strand breaks induced by ionizing radiation are of high physiological importance due to their role in cancer development[50]. Their influence on DNA conductivity is, therefore, of special interest for this work. SBs are alterations of the molecular structure of the DNA backbone. They are caused by the incision of bonds at C3 or C5 atoms of the DNA pentose. While the charge transport in DNA happens across nucleobases, deterioration of conductivity due to strand breaks may occur due to a decreasing regularity in π -stacking in the damaged DNA.

Yamaguchi et al.[51] investigated single SBs in short 12 bp oligonucleotides using molecular dynamics simulations. They found that this simple lesion has little effect on base stacking over the simulation time of 1 ns. In a similar study with 8 bp oligonucleotides over 10 ns, conformational changes showed up with a delay of a few nanoseconds[52]. SSBs should therefore be expected to affect DNA conductivity.

Double strand breaks are more complex lesions which are expected to cause even higher instability of the DNA helical structure. As mentioned above, the two SSB's which comprise the DSB are separated by not more than ten base pairs. The thermal stability of these ten, or less, base pairs may not be sufficient to keep the bases paired[53]. This can even lead to the DNA separating into two strands with single stranded overhangs at the damaged site.

Base Modifications

Molecular dynamics (MD) simulation of oligonucleotides with various modified bases showed little impact on base stacking[27, 55]. Since the bases are, however, directly involved in charge transfer, base modifications can still impact electrical conductivity, as does the DNA sequence. This is confirmed by studies of oxidative damage transport in short dsDNA containing base modifications[56]. It was found that modifications can change charge transfer rates, however the direction of the change depends on the type of base modification. Long AT sequences show poor conductivity, as was previously explained. Charge transfer rates were observed to increase, when a 7-deazaA modification was included into the sequence. In a similar way 7-deazaG was found to reduce conductivity. Interestingly, both modifications have a stabilizing effect on the helical structure[57]. Overall, it can be concluded that a decrease in the ionization potential of the bases enhances the charge transport and vice versa.

Inter- and intrastrand crosslinks have diverging effects on the DNA molecule. While interstrand CLs are found to have a stabilizing effect on the helical structure[58], intrastrand CLs destabilize the double helix[59]. A theoretical study on the electronic properties of AT interstrand crosslinks revealed that even though hole transfer rates were unaffected, electron transfer rates were significantly reduced[7]. Therefore, crosslinks in either form are expected to have a negative effect on DNA conductivity.

2.2.4 DNA Electrode Linking

Shortly after DNA was found to permit charge flow, the linking of the molecule to electrodes became the topic of research. Probably the most common type of DNA-Gold linkage occurs via thiol ends. Here the DNA is functionalized with a thiol group. The sulfur atom of the thiol can build a covalent bond to gold, which grants high mechanical stability[60].

A literature survey shows that experiments with thiol anchoring groups generally exhibit lower resistance values than unthiolized molecules. For example, experiments for short-range conductivity in 30 bp dsDNA were conducted by Kang et al.[61] and Porath et al.[4]. Kang et al. employed thiol linkers and measured resistance values around 100 M Ω . Porath et al. obtained semiconducting results with a 2 G Ω resistance. Similar behavior was observed for long-range conductivity. Kassegne

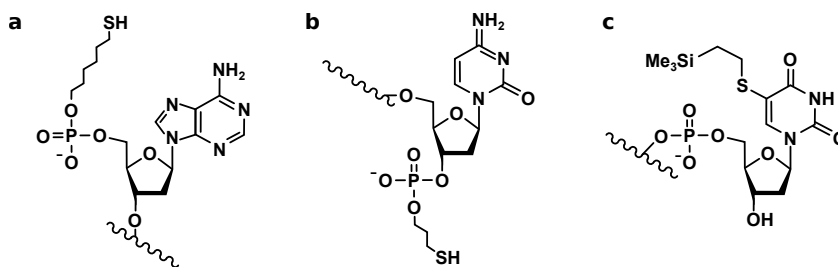


Figure 2.6: Selected variations of thiolated DNA in skeletal formula. The figure shows different possibilities for thiol modification of DNA. Image **a** depicts a 5'-thiol modification (thiohexyl; C6) and **b** a 3'-thiol (C3). Image **c** shows a thiolated nucleotide, namely a thymidine base bearing a (trimethylsilyl)ethyl protected thiol at its 5-position.

et al.[11] measured ohmic resistance values around $10\text{ M}\Omega$ over $10\text{ }\mu\text{m}$ with thiol linkers. Braun et al.[8], on the other hand, observed insulating behavior over $15\text{ }\mu\text{m}$ without thiol linkers.

Most often, the thiol groups are located at the 5' or 3' end of the DNA (referring to the position of the carbon in the ribose sugar of the DNA backbone). While such a configuration does permit current flow[61, 62, 11] it might act as a limiting factor in the conductivity measurement. As shown in figure 2.6, the thiol is bound to the DNA backbone. Charge is transported in DNA, however, through the π -orbitals of the bases. The presence of a non-conjugated alkyl chain between the thiols and π -system, results in weak overlap of their electronic orbitals. DNA can also be functionalized with thiol functionalized bases, as was done by Liu et al.[13]. They found that this anchoring results in reduced electrical resistance for dsDNA compared to conventional thiol anchors.

The DNA molecule itself can also be used as an anchoring group. Unpaired DNA bases can adsorb to gold surfaces where the affinity decreases in the order of $G > A > C > T$. [63] Chains of consecutive adenine bases, so called polyA groups, preferentially adsorb on gold surfaces with high affinity[64, 65, 66]. In the literature review, no publication was found that employ polyA anchoring groups for conductivity measurements. As with thiolated nucleobases, this method would provide strong overlap between the electronic orbitals of gold and the π -system of the adenine chain. The former, however, have the advantage of being implemented directly into a double strand.

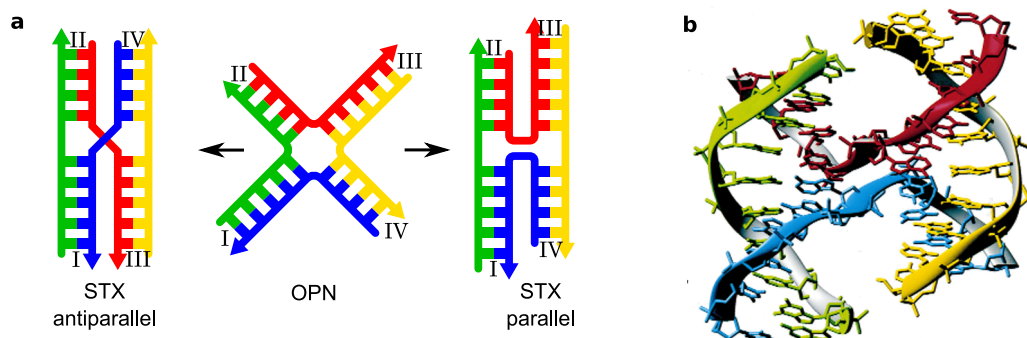


Figure 2.7: Schematic representation of the Holliday junction. Image **a** shows the canonical stacked-X (STX, shown left and right) and open-X (shown in the middle) conformations of a Holliday junction. The STX form is further differentiated by either an antiparallel or parallel directionality. A parallel STX junctions is also shown in image **b** as a ribbon diagram[71].

2.2.5 DNA Four-Way Junction

The DNA four-way junction (4WJ), also known as the Holliday junction, is an intertwinning crossroad junction of four DNA double strands[67]. These are commonly used in the assembly and design of DNA origami structures. DNA origami structures often contain hundreds of Holliday junctions[68]. Here the structure is found in the parallel immobile stacked-X (STX) form, as shown in figure 2.7. It was found, that oxidative damage can be transferred across Holliday junctions[69, 70]. The results showed that charge can migrate along the helical axis, but not between the two coaxial strands. These results are in agreement with studies of the molecular structure of DNA 4WJs. Either form showed continuous base stacking for the outer strands[71, 72]. It can therefore be excluded, that Holliday junctions would prevent charge transport along a DNA origami structure. Since only one strand is available across the junction, however, the rate might be reduced. This should also depend on the bases involved. A high G rate in the coaxial strand, for example, would make it the preferred path for the charge anyway. It should also be noted that the expected charge transfer rates across the unpaired part of a 4WJ would be higher than in a single strand, due to its better stability.

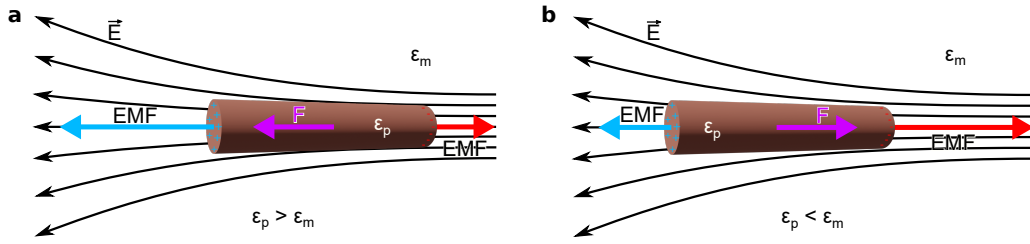


Figure 2.8: Schematic illustration of positive (a) and negative (b) dielectrophoresis

2.3 Electrokinetic Phenomena

2.3.1 Dielectrophoresis

Dielectrophoresis (DEP) describes the effect in which particles are moved by polarization forces produced by an inhomogeneous electric field[73]. The electric force on a charge is proportional to the field strength. Due to the inhomogeneity of the electric field, each side of the polarized particle experiences a different force. This results in a net force in the direction of the field gradient, called dielectrophoretic force. This effect doesn't require the particle to be charged itself. If the particle has a net charge, an electrophoretic force is acting as well. This effect, however, can disappear in an AC electric field. If the frequency is sufficiently high, the field oscillations result in a time-averaged zero force. Depending on the polarizability of the particle and the medium, DEP can either be 'positive' or 'negative'. 'Positive DEP' means, that the resulting force is directed towards areas of high field gradient. This is the case, if the particle has higher polarizability than the medium. In the opposite case, if the medium has higher polarizability than the particle, the DEP force is directed towards areas of low field gradient. This is called 'negative DEP'.

To express the DEP force, it is first assumed that particle and medium behave as a dipole. The dipole moment \mathbf{p} of a particle in an electric field \mathbf{E} can be expressed by the equation

$$\mathbf{p} = \alpha \mathbf{E}, \quad (2.2)$$

where α is the effective polarizability of the particle. The polarizability is often described with the help of the Clausius-Mosotti factor CM[74]. For the case of a spherical particle of permittivity ϵ_p in a medium of the permittivity ϵ_m , the complex CM factor is given as

$$\text{CM} = \frac{\varepsilon_p^* - \varepsilon_m^*}{\varepsilon_p^* + 2\varepsilon_m^*}. \quad (2.3)$$

The complex permittivity ε^* considers the conduction and dielectric energy losses of the particles. For a particle with the relative permittivity ε_p' and conductivity σ_p , the complex permittivity is

$$\varepsilon_p^* = \varepsilon_0 \varepsilon_p' - i \frac{\sigma_p}{\omega}, \quad (2.4)$$

with ε_0 being the dielectric constant and ω the angular frequency. The polarizability for a spherical particle can be expressed as

$$\alpha = 3V\varepsilon_m \text{Re}(\text{CM}), \quad (2.5)$$

where V is the volume of the particle and $\text{Re}(\text{CM})$ the real part of the Clausius-Mosotti factor. The force on a polarized particle in an electric field is

$$\mathbf{F}_{\text{DEP}} = (\mathbf{p} \cdot \nabla) \mathbf{E} = \frac{\alpha}{2} \nabla (|\mathbf{E}|^2). \quad (2.6)$$

Inserting equation 2.5 into equation 2.6 yields the time-averaged force

$$\langle \mathbf{F}_{\text{DEP}} \rangle = 2\pi\varepsilon_m r_p^3 \text{Re}(\text{CM}) \nabla (|\mathbf{E}|^2), \quad (2.7)$$

where r_p is the particle radius. For longer particles such as DNA molecules, an prolate ellipsoid is a more accurate representation (see figure 2.9). In this case, the DEP force is given by

$$\langle \mathbf{F}_{\text{DEP}} \rangle = \frac{4}{3} \pi a b^2 \varepsilon_m \frac{\varepsilon_p - \varepsilon_m}{Z \varepsilon_p + (1 - Z) \varepsilon_m} \nabla (|\mathbf{E}|^2), \quad (2.8)$$

with the depolarization factor $Z = \frac{b^2}{2a^2 e^3} \left[\ln \left(\frac{1+e}{1-e} \right) - 2e \right]$. Here, $2a$ and $2b$ are the width and height of the ellipsoid, respectively. The eccentricity e is defined by $e = \sqrt{1 - (b^2/a^2)}$ [75].

To formulate an equation of motion, we assume Stokes drag to be valid[76]. The change of momentum of a particle with mass m , influenced by a force \mathbf{F} can be expressed as

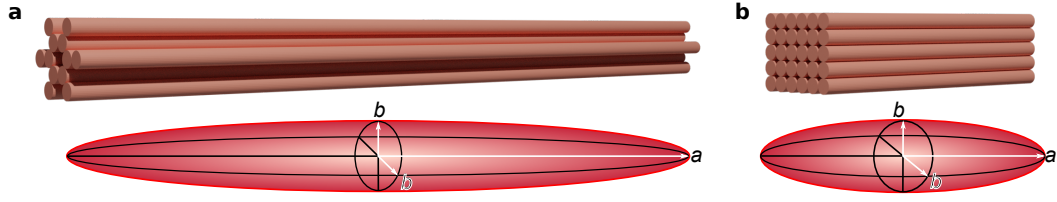


Figure 2.9: DNA as ellipsoid shapes

$$m \frac{d\mathbf{u}}{dt} = -\gamma(\mathbf{u} - \mathbf{v}) + \mathbf{F}. \quad (2.9)$$

Here \mathbf{u} is the particle velocity, \mathbf{v} the fluid flow velocity and γ is the fluid friction factor. For simplicity, it is assumed that fluid drag works as if the particle was spherical with an effective radius b . The fluid friction factor can then be expressed as $\gamma = 6\pi\eta b$, with η being the viscosity of the medium. For constant \mathbf{F} and \mathbf{v} , the velocity of a particle with an initial velocity \mathbf{u}_0 is

$$\mathbf{u} = \left(\mathbf{u}_0 - \mathbf{v} - \frac{\mathbf{F}}{\gamma} \right) e^{-\frac{t}{\tau_a}} + \mathbf{v} + \frac{\mathbf{F}}{\gamma} \quad (2.10)$$

at the time t . The characteristic time of acceleration $\tau_a = m/\gamma$ is typically much smaller than the time scales of observation (~ 1 s). The particle can therefore be considered to travel with its terminal velocity

$$\mathbf{u} = \mathbf{v} + \frac{\mathbf{F}}{\gamma}. \quad (2.11)$$

The second term accounts for the velocity induced by the force \mathbf{F} . The DEP-induced velocity of such a particle follows from equation 2.8 as

$$\mathbf{v}_{DEP} = \frac{4\pi ab^2 \epsilon_m}{3\gamma} M \nabla |\mathbf{E}|^2, \quad (2.12)$$

with $M = \frac{\epsilon_p - \epsilon_m}{Z\epsilon_p + (1-Z)\epsilon_m}$.

For further analysis a simplified system illustrated in figure 2.10 is assumed[76]. Here the electrical field lines between the two co-planar electrodes are semi-circular. The electrical field is than given by

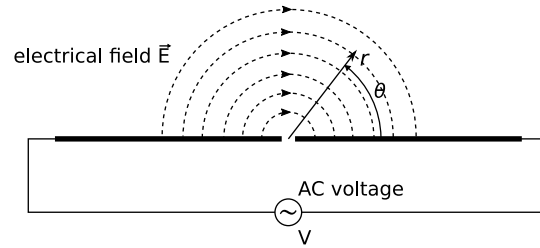


Figure 2.10: Schematic diagram of the simplified system

$$\mathbf{E} = \frac{V_{rms}}{\pi r} \mathbf{u}_\theta, \quad (2.13)$$

with \mathbf{u}_θ being the unit vector of the θ coordinate. With this description for the electric field, the absolute value for the DEP-induced velocity is

$$|\mathbf{v}_{DEP}| = \frac{4ab\epsilon_m V_{rms}^2}{9\pi^2\eta r^3} |M|. \quad (2.14)$$

2.3.2 AC Electro-osmosis

Alternating current (AC) electro-osmosis (EO) is an electrokinetic phenomenon. It is observed in micro- and nanoelectrode structures subjected to AC voltages in aqueous solutions. The name is derived from the similar direct current (DC) electro-osmotic effect. Both effects are based on the formation of an electric double layer (EDL) at the interface of a liquid electrolyte and the surface of a charged object[77, 78]. The ions in the electrolyte accumulate near the surface, forming a diffuse layer with an exponential voltage drop. This effect doesn't require the electrolyte to have a net charge. In DC EO the surface charge of an electrode causes a redistribution of the ions in the liquid. In the case of AC EO, a redistribution of ions may arise due to the electric potential over the electrodes[79]. This potential also causes an electric field, in which the ions experience an electric force. The direction of the fluid flow is always tangential to the electrodes and independent of the direction of the electric field. Due to viscous forces, the ions driven by this electric force cause the rest of the fluid to be dragged along with them.

An electric field \mathbf{E} is determined by the gradient of the electric potential V :

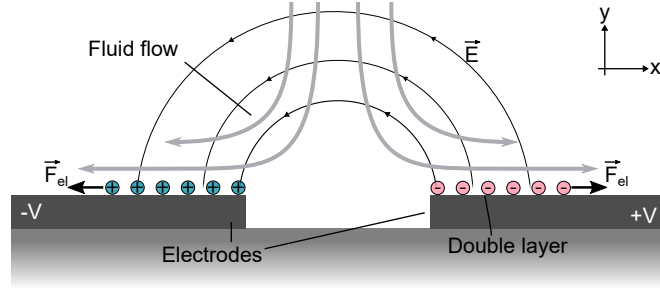


Figure 2.11: Schematic illustration of the AC electro-osmotic effect

$$\mathbf{E} = -\nabla V. \quad (2.15)$$

According to Ohm's law, the current density \mathbf{J} is proportional to the electric field:

$$\mathbf{J} = \sigma \mathbf{E}. \quad (2.16)$$

For static conditions, the gradient of the current density vanishes:

$$\nabla \cdot \mathbf{J} = 0. \quad (2.17)$$

Equations 2.16 and 2.15 yield

$$\nabla \cdot \mathbf{J} = \sigma \nabla \cdot \mathbf{E} = -\sigma \nabla^2 V = 0. \quad (2.18)$$

The boundary condition on the EDL surface can be formulated as [78, 80]

$$\sigma \frac{\partial V}{\partial \mathbf{y}} = \frac{\partial q_{EDL}}{\partial t}, \quad (2.19)$$

with q_{EDL} being the surface charge of the EDL. In equation 2.19, it is presumed that lateral currents along the EDL are negligible. For a sufficiently small voltage drop across the double layer, a linear relation between the charge and the voltage can be assumed:

$$q_{EDL} = C_{EDL}(V - V_{el}). \quad (2.20)$$

C_{EDL} is the capacitance per unit area of the EDL and V_{el} the voltage applied to the electrode. The boundary condition, formulated in equation 2.19, can contain complex parts. Therefore, V and σ are complex quantities. Equation 2.19 written with complex numbers becomes:

$$\sigma \frac{\partial V}{\partial \mathbf{y}} = i\omega q_{EDL} = i\omega C_{EDL}(V - V_{el}). \quad (2.21)$$

The fluid flow velocity \mathbf{v} can be estimated using the Helmholtz-Smoluchowski formula[78]

$$\mathbf{v} = -\frac{\varepsilon}{\eta} \Delta V_d \frac{\partial V}{\partial x} = -\frac{\varepsilon}{\eta} \Delta V_d \mathbf{E}_t, \quad (2.22)$$

with ε being the permittivity, η the fluid viscosity, ΔV_d the voltage drop across the diffuse layer and \mathbf{E}_t the component of the electrical field tangential to the electrode. Since the velocity normal to the electrodes is zero, equation 2.22 gives the tangential velocity. The time averaged fluid velocity is then[76]

$$\langle v_x \rangle = \frac{\varepsilon}{2\eta} \Lambda \text{Re} [\Delta V_d \mathbf{E}_t^*] = -\frac{\varepsilon}{4\eta} \Lambda \frac{\partial}{\partial x} |\Delta V_d|^2. \quad (2.23)$$

The asterisk marks the complex conjugate. In the Stern model a capacitive double layer consists out of a Stern, or compact layer and a diffuse layer[81]. The ratio between the voltage drop across the diffuse layer to the total voltage drop across the EDL is expressed using the empirical factor

$$\Lambda = \frac{C_S}{C_S + C_D}. \quad (2.24)$$

The capacities per unit of area C_S and C_D are the capacities of the Stern and diffuse layers, respectively. With this the voltage drop ΔV_d can be estimated using simple circuit theory[76]:

$$\Delta V_d = \Lambda \frac{V_{rms}/2}{1 + i\pi C\omega r/2\sigma}, \quad (2.25)$$

where $C = \Lambda C_D$. Therefore, the velocity due to AC electro-osmosis from equation 2.23 becomes

$$v_{EO} = \Lambda \frac{\varepsilon V_{rms}^2}{8\eta r} \frac{\Omega^2}{(1 + \Omega^2)^2} \quad (2.26)$$

with the non-dimensional frequency

$$\Omega = \Lambda \frac{\omega C_D \pi r}{2\sigma} \quad (2.27)$$

The surface capacitance C_D can be derived using the Debye-Hückel model as

$$C_D = \frac{\varepsilon_m}{\lambda_D} \quad (2.28)$$

with the Debye length $\lambda_D = \sqrt{\frac{\varepsilon_m k_B T}{6\pi a \eta \sigma}}$.

2.3.3 Electrothermal Fluid Flow

Electrothermal fluid flow originates from Joule heating causing a temperature gradient inside the fluid. In the case of two nanoelectrodes, this flow arises due to the high electrical field in between the electrodes.

Equation 2.18 in its simplest form is known as the Laplace equation for a homogeneous medium:

$$\nabla^2 V = 0. \quad (2.29)$$

The temperature rise can be estimated by solving the following balance equation[82, 83]:

$$\rho_m c_p \langle \mathbf{v} \rangle \nabla T + \rho_m c_p \frac{\partial T}{\partial t} = k \nabla^2 T + \sigma |\mathbf{E}|^2, \quad (2.30)$$

where ρ_m is the mass density, c_p the specific heat, k the thermal conductivity and σ the electrical conductivity of the medium. It can be assumed, that the fluid flow does not affect the temperature profile[83]. Therefore, equation 2.30 becomes

$$k \nabla^2 T + \sigma |\mathbf{E}|^2 = 0. \quad (2.31)$$

For a characteristic length of the system l it can be estimated that $\nabla^2 T \sim \Delta T / l^2$ and $E = V_{rms} / l$. V_{rms} is the RMS voltage. In the case of the nanoelectrode system, l would be the length of the electrode gap. This approximation in the electric field equation 2.31 gives

$$k \frac{\Delta T}{l^2} \sim \sigma \left(\frac{V_{rms}}{l} \right)^2. \quad (2.32)$$

Therefore, the temperature rise can be estimated according to

$$\Delta T \sim \frac{\sigma V_{rms}^2}{k}. \quad (2.33)$$

In a solution with an electrical and thermal conductivity of $300 \mu\text{S/cm}$ [10] and $0.6 \text{ W/(m}\cdot\text{K)}$ [84], respectively, a RMS voltage of 1 V between the electrodes would cause a temperature rise of about 0.05 K.

The density of electrical forces \mathbf{f}_e on a liquid can be expressed as[85]

$$\mathbf{f}_e = \rho_q \mathbf{E} - \frac{1}{2} |\mathbf{E}|^2 \nabla \epsilon + \frac{1}{2} \nabla \left[\rho_m \left(\frac{\partial \epsilon}{\partial \rho_m} \right)_T |\mathbf{E}|^2 \right], \quad (2.34)$$

with the charge density ρ_q and the permittivity of the fluid ϵ . The first term on the right-hand side of equation 2.34 represents the Coulomb force and the second the dielectric force. The third term describes electrostriction and can be neglected in an incompressible fluid[83]. Temperature changes due to Joule heating are very small in a nano- and microelectrode systems. Consequently, gradients $\nabla \epsilon$ and $\nabla \sigma$ can also be considered small, so that

$$\nabla \epsilon \approx \frac{\partial \epsilon}{\partial T} \nabla T \quad (2.35)$$

and

$$\nabla \sigma \approx \frac{\partial \sigma}{\partial T} \nabla T. \quad (2.36)$$

Due to the small gradients in permittivity and conductivity[76], the electric field can be expanded to

$$\mathbf{E} = \mathbf{E}_0 + \mathbf{E}_1 \quad (2.37)$$

where $|\mathbf{E}_1| \ll |\mathbf{E}_0|$,

$$\nabla \cdot \mathbf{E}_0 \quad (2.38)$$

and

$$\nabla \cdot \mathbf{E}_1 + \left(\frac{\nabla \sigma + i\omega \nabla \varepsilon}{\sigma + i\omega \varepsilon} \right) \cdot \mathbf{E}_0 = 0. \quad (2.39)$$

The time-averaged electrical force density can be expressed as[83]

$$\langle \mathbf{f}_e \rangle = \frac{1}{2} \frac{\varepsilon(\alpha - \beta)}{1 + (\omega\tau)^2} (\nabla T \cdot \mathbf{E}_0) \mathbf{E}_0 - \frac{1}{4} \varepsilon \alpha |\mathbf{E}_0|^2 \nabla T, \quad (2.40)$$

with

$$\alpha = \frac{1}{\varepsilon} \frac{\partial \varepsilon}{\partial T} \approx \frac{1}{\varepsilon} \frac{\nabla \varepsilon}{\nabla T}, \quad (2.41)$$

$$\beta = \frac{1}{\sigma} \frac{\partial \sigma}{\partial T} \approx \frac{1}{\sigma} \frac{\nabla \sigma}{\nabla T}, \quad (2.42)$$

and

$$\tau = \frac{\varepsilon}{\sigma}. \quad (2.43)$$

The change in temperature for such a system is [83]

$$\Delta T = \frac{\sigma V_{rms}^2}{2\kappa} \left(\frac{\theta}{\pi} - \frac{\theta^2}{\pi^2} \right) \quad (2.44)$$

with κ being the thermal conductivity of the fluid and θ the angle measured from one electrode in the simplified system (see fig. 2.10). The insertion of equations 2.13 and 2.44 in equation 2.40 yields the electric force density as

$$\langle \mathbf{f}_e \rangle = \left(\frac{\alpha - \beta}{1 + (\omega\tau)^2} - \frac{\alpha}{2} \right) \frac{\varepsilon \sigma V_{rms}^2}{4\kappa (\pi r)^3} \left(1 - \frac{2\theta}{\pi} \right) \mathbf{u}_\theta. \quad (2.45)$$

The motion of an incompressible liquid can be expressed by the NavierStokes equations

$$\nabla \cdot \mathbf{v} = 0 \quad (2.46)$$

and

$$\rho_m \left(\frac{\partial v}{\partial t} + (v \cdot \nabla) v \right) = -\nabla p + \eta \nabla^2 v + \langle f_E \rangle. \quad (2.47)$$

The left-hand side of equation 2.47 describes the convection. This term can be neglected for a very low Reynolds number

$$\text{Re} = \frac{\rho_m v l}{\eta} \sim \frac{|\rho_m (v \cdot \nabla) v|}{|\eta \nabla^2 v|}, \quad (2.48)$$

which is typical for microsystems. Using the equation for the average electric force density (Eq. 2.45) and the NavierStokes equations (Eq. 2.46 and Eq. 2.47), the description for the radial velocity for the simplified system[83] can be obtained:

$$v_r = \left(\frac{\alpha - \beta}{1 + (\omega\tau)^2} - \frac{\alpha}{2} \right) \frac{\varepsilon\sigma V_{rms}^2}{2\kappa\pi^3 r} \left[-\frac{1}{2} \left(\theta - \frac{\theta^2}{\pi} \right) - \frac{\pi}{12} [\cos(2\theta) - 1] \right]. \quad (2.49)$$

The maximum velocity occurs at $\theta = \pi/2$. For that angle, the right hand side term becomes $\pi/24$:

$$|v_{max}| = \left| \frac{(\alpha - \beta)}{1 + (\omega\tau)^2} + \frac{1}{2}\alpha \right| \frac{\varepsilon\sigma V_{rms}^4}{96\pi^2\kappa\eta r}. \quad (2.50)$$

For the cases $\varepsilon\omega/\sigma \ll 1$ and $\varepsilon\omega/\sigma \gg 1$ the velocity can be estimated as

$$v_{max} \approx \frac{\varepsilon\sigma V^4}{96\pi^2\kappa\eta r} |\beta| \quad (2.51)$$

and

$$v_{max} \approx \frac{\varepsilon\sigma V^4}{192\pi^2\kappa\eta r} |\alpha|. \quad (2.52)$$

2.4 Molecular Dynamics

Molecular dynamics aims to mimic the natural motion of molecular systems with computer simulations. Due to limited computational power, a compromise between accuracy and efficiency is necessary. This section aims to give a brief overview about basic elements of molecular dynamics simulation. The focus lies on methods used in this work.

2.4.1 Force Field

An accurate description of molecular properties requires the solution of the relativistic time-dependent Schrödinger equation. This task is only possible with approximations in the case of large polyatomic molecules. The method based on force fields is a possible approach if the focus lies on the geometric structure. In the molecular mechanics approach atoms are treated as classical particles. The potential energy of the system is calculated using the Born-Oppenheimer approximation. In the molecular mechanics approach, the energy of the molecular system is divided in covalent and non-covalent energies.

$$E = E_{covalent} + E_{noncovalent} \quad (2.53)$$

For biomolecules, the covalent energy typically comprises energies for bond stretching E_{bond} , bending E_{angle} and torsion $E_{dihedral}$:

$$E_{covalent} = E_{bond} + E_{angle} + E_{dihedral}. \quad (2.54)$$

Stretching and bending can be estimated using harmonic potentials. The above energies depend on the force constant and equilibrium bond lengths which are either derived from experiments or theoretical calculations[86]. This approach has the limitation that bonds cannot be broken. The consideration of bond breakage requires a more complex method, such as the reactive force field approach[87], or a quantum chemical (QC) approach. In case of dihedrals, a harmonic potential cannot be assumed.

The non-covalent energy includes electrostatic Coulomb, as well as van der Waals (vdW) interactions.

$$E_{noncovalent} = E_{Coulomb} + E_{van\ der\ Waals} \quad (2.55)$$

Coulomb interactions are computed using charges centered at each atom which are derived from QC calculations of the whole molecule. The van der Waals term represents a combination of the vdW force and Pauli repulsion. It is approximated with $6 - 12$ Lennard-Jones potentials. The calculation of the non-covalent contributions requires substantial computing time for large biomolecules. For van der Waals interaction, this problem can be solved with a cut-off distance, as the vdW force rapidly

decreases with distances. At a certain cut-off distance, the energy contribution of the vdW force can be estimated to be zero. A similar approach can be used for electrostatic forces. The much more shallow decrease requires a more sophisticated approach such as the particle-mesh-Ewald method[88].

The individual energies combined with the necessary parameter sets are the input quantities of the force field method. If the initial geometry is known, the total energy of a molecule can be calculated.

2.4.2 Motion and Timestep

Molecules and atoms at finite temperatures are in constant motion and not fixed at their equilibrium positions. The molecular dynamics simulation uses Newton's equations of motion.

$$\vec{F}_i = m_i \vec{a}_i = m_i \frac{\delta^2 \vec{r}_i}{\delta t^2} \quad (2.56)$$

The vector \vec{a}_i is the acceleration acting on the atom i with mass m_i at the position \vec{r}_i . The force is the negative gradient of the energy:

$$\vec{F}_i = - \frac{\delta E(\vec{r}_i)}{\delta \vec{r}_i}. \quad (2.57)$$

The equations of motion are differential equations of second order. The equations are solved numerically by introducing a time step Δt . For this purpose, various methods can be applied. The simplest method is the Euler algorithm. Another method, which was used in this work, is the leapfrog integration method[89]. Positions and velocities are calculated alternately, with velocities being updated with an offset of half a timestep.

$$\vec{r}(t) \rightarrow \vec{v}(t + 1/2\Delta t) \rightarrow \vec{r}(t + \Delta t) \rightarrow \vec{v}(t + 3/2\Delta t) \rightarrow \dots \quad (2.58)$$

Current velocities and positions are then calculated by

$$\vec{v}(t + \Delta t) = \vec{v}(t - 1/2\Delta t) + \vec{a}(t) \Delta t \quad (2.59)$$

and

$$\vec{r}(t + \Delta t) = \vec{r}(t) + \vec{v}(t + 1/2\Delta t) \Delta t. \quad (2.60)$$

The numerical precision depends on the choice of the time step. When choosing a timestep it also needs to be considered that the fastest motion in the system has to be included. In biomolecular systems this is usually the vibration of C-H bonds. The vibration period is about 10 ns. Bearing those considerations in mind, the time step should be chosen as high as possible to reduce the computational time[90].

2.4.3 Thermodynamics

MD simulations were performed for canonical and isothermal-isobaric thermodynamic ensembles to consider environmental conditions. In the former case the number of particles N , the volume of the simulation box V and the temperature T are kept constant. Canonical ensembles are therefore called NVT ensembles. In the case of isothermal-isobaric ensembles the pressure p is kept constant instead of the volume. These ensembles are also called NPT ensembles. The number of particles and size of the simulation box stay constant during the simulation. Therefore, the conservation of N and V requires no further effort. Temperature and pressure conservation, on the other hand, need to be regulated. This is called temperature, or pressure coupling respectively.

The relationship between the temperature and kinetic energy of the system E_{kin} is described by

$$E_{kin} = \frac{1}{2} m \langle v^2 \rangle = \frac{3}{2} k_B T, \quad (2.61)$$

where k_B is the Boltzmann constant and $\langle v^2 \rangle$ the average of the squared atom velocities. The temperature can therefore be regulated by scaling the atom velocities in the system. At the very start of a simulation, velocities are assigned to the atoms in a system. These velocities are then constantly regulated during the simulation to keep the system at the desired temperature. One way to implement temperature coupling is a Berendsen thermostat[91]. This couples the system to an external heat bath with the temperature T_{ref} .

$$\frac{dT}{dt} = \frac{1}{\tau} (T_{ref} - T) \quad (2.62)$$

The time constant τ is a measure for how tightly the system and the heat bath are coupled to each other. The deviations from the target temperature are calculated as

$$\Delta T = \frac{\Delta t}{\tau} (T_{ref} - T). \quad (2.63)$$

Using equation 2.61, one can deduce the relation

$$\Delta T = (\lambda^2 - 1) T, \quad (2.64)$$

with the scaling factor

$$\lambda = \sqrt{1 + \frac{\Delta t}{\tau} \left(\frac{T_{ref}}{T} - 1 \right)}. \quad (2.65)$$

Temperatures are then corrected by applying the scaling factor to the velocities in the system.

The same method can be used to regulate the pressure in the system. Pressure coupling is realized by scaling the volume of the simulation box.

This chapter introduces various experimental techniques used in this work. It contains sample preparation and measurement methods as well as descriptions of the experimental setup for impedance spectroscopy.

3.1 DNA Origami Technique

This technique was first published in 2006 by Paul Rothemund[92] and can be used to fold DNA into arbitrary two- and three-dimensional shapes, so called DNA origami structures. A long ssDNA is folded with the aid of multiple shorter oligonucleotides,

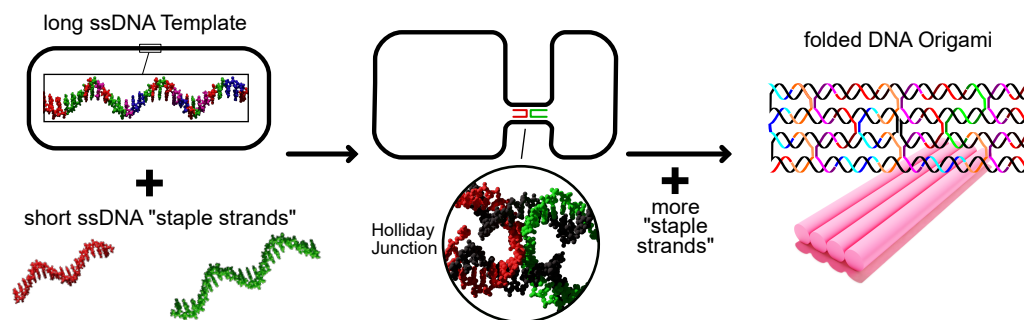


Figure 3.1: Illustration of the DNA origami technique

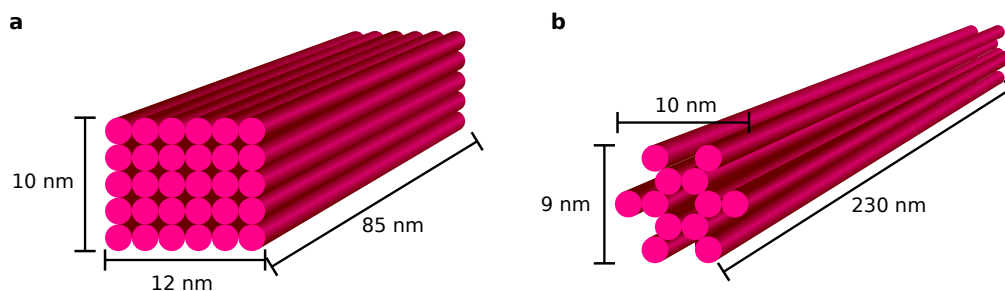


Figure 3.2: 30HB and 12HB DNA origamis structures. Images **a** and **d** show drawings of the two DNA origami structures.

so called staple strands. For the long strand usually a viral DNA strand with around 7 to 9 kbp length is used. Since the exact sequence of this viral DNA is known it can be used as a scaffold for the DNA origami structure. This exploits the specificity of Watson-Crick base pairing, acting like a key and lock principle. The staple strands bind to specific places of the long DNA, stapling together certain regions (see figure 3.1). A computer program can calculate the staple strands necessary to fold the scaffold strand into the desired shape. DNA components are then mixed together, heated and cooled down to room temperature. While cooling down, the staple strands hybridize with the viral DNA generating billions to quadrillions of identical DNA origami structures per microliter.

The DNA origami technique offers, therefore, the benefits of high yields with geometric homogeneity and easily programmable two- and three-dimensional shapes. As the staple strands can be chemically modified, DNA origami structures are often used as templates for functional nanomaterials. Organization of these nanomaterial can achieved with a high spatial resolution of ~ 5 nm, due to the specificity of Watson-Crick base pairing. This makes the DNA origami technique an attractive method for “bottom-up” nanofabrication[93]. As such, applications of DNA origami structures include electronics[94, 95], as microscopy standards[96, 97] and molecular diagnostics[98, 99]. DNA origami structures have also been implemented into “top-down” nanofabrication[100, 101].

In this work, 12-helix bundle (12HB) and 30-helix bundle (30HB) DNA origami structures were used. The former were produced at the LMU Munich by the Tinnefeld lab and the latter by Tilbit nanosystems[102]. Drawings of the two structures are shown in figure 3.2. Both DNA origami structures were designed using the caDNAno[103] software. The 12HB structure was designed in a honeycomb lattice

3.2. DNA Origami Structure Trapping

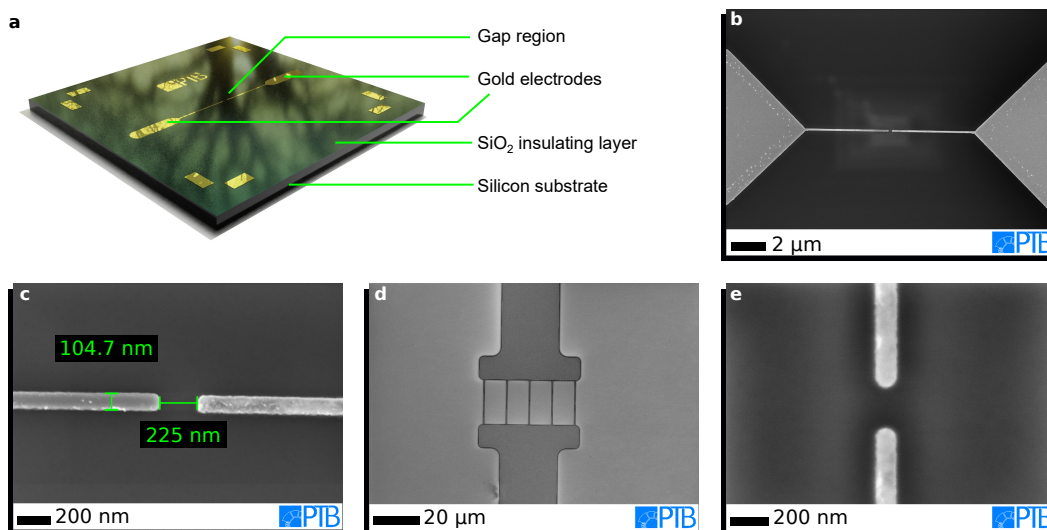


Figure 3.3: Silicon chips with gold nanoelectrodes. Image **a** shows a chip used for experimentation. The scanning electron microscopy (SEM) images in **b** and **c** show an examples of a single gap configuration and the images in **d** and **e** an example of a multigap configuration.

with the p8064 scaffold strand. A detailed description of the folding and purification procedure can be found in [104]. Since the DNA origami structures will be used to support electric currents, this straight, rod like shape was chosen. The multilayered structure might also be beneficial for charge transport, since the inner strands can better maintain their regular stacked form in dry ambient conditions. The 30HB was designed in a square lattice with the p7560 scaffold strand. It has a tighter packaged structure than the 12HB which might make it more resilient against the effects of microhydration. The production and purification of the 30HB structures is described in [10]. Sequence maps of both DNA origami structures are shown in the figures A.1 and A.2 in the appendix.

3.2 DNA Origami Structure Trapping

3.2.1 Nanoelectrodes

The challenge of measuring the electrical properties of single molecules lies in the task of how they can be connected to the measuring instruments (3.4.2). The connection requires special electrodes to bridge the molecules to our macroscopic mea-

Dielectrophoresis	$\frac{4ab\epsilon_m V_{rms}^2}{9\pi^2 \eta r^3} M t$
AC electro-osmosis	$\Lambda \frac{\epsilon V_{rms}^2}{8\eta r} \frac{\Omega^2}{(1+\Omega^2)^2} t$
Electrothermal	$\frac{\epsilon \sigma V^4}{96\pi^2 \kappa \eta r} \left \frac{\alpha - \beta}{1 + (\omega\tau)^2} - \frac{\alpha}{2} \right t$
Brownian displacement	$\sqrt{\frac{k_B T}{3\pi a \eta}} \cdot t [76]$

Table 3.1: Sources of displacement during DEP capture and corresponding equations. The equations listed are the equations 2.14, 2.26 and 2.50 multiplied with the time t .

surement devices. The fabrications of the electrodes was achieved by electron beam lithography, physical vapor deposition and reactive ion etching[105]. Silicon-wafers were used as a substrate material. These are (100) p-type, boron doped wafers with a resistivity of 1-10 Ωcm and a total thickness of 381 μm . The electrodes consist of a 20 nm gold layer on top of a 5 nm platinum layer. Gold is used for its poor chemical reactivity. The platinum acts mainly as an adhesive layer. For insulation, a 600 nm silicon oxide layer is thermally grown on the silicon substrate. The fabrication was carried out at the Physikalisch-Technische Bundesanstalt in Germany by the Weimann group.

The electrodes were designed in a “fingertip” shape, as shown in figure 3.3. To account for the stochastic nature of the DNA capture probability, a special configuration with multiple electrode pairs was employed. This provides five electrode pairs in an electrically parallel arrangement as shown in figure 3.3 c.

3.2.2 DEP Trapping

The trapping is based on the dielectrophoretic effect, as explained in section 2.3.1. Not only the dielectrophoretic force, but also electrothermal forces, electro-osmotic forces, gravity, buoyancy and Brownian displacement act on the DNA molecule. An overview of the displacement, caused by these influences is shown in table 3.1. The displacements from electrokinetic phenomena have been discussed in section 2.3. Table 3.1 contains also the displacement due to the Brownian motion. Although gravity and buoyancy[76] are also sources of displacement, they only play a minor role for the case of DNA capture.

To overcome the displacement due to the Brownian motion, electric fields of sufficient strength are required. Figure 3.4 shows the displacements in 1 s for DEP and the Brownian motion against the characteristic length. For a voltage in the order of 1 V,

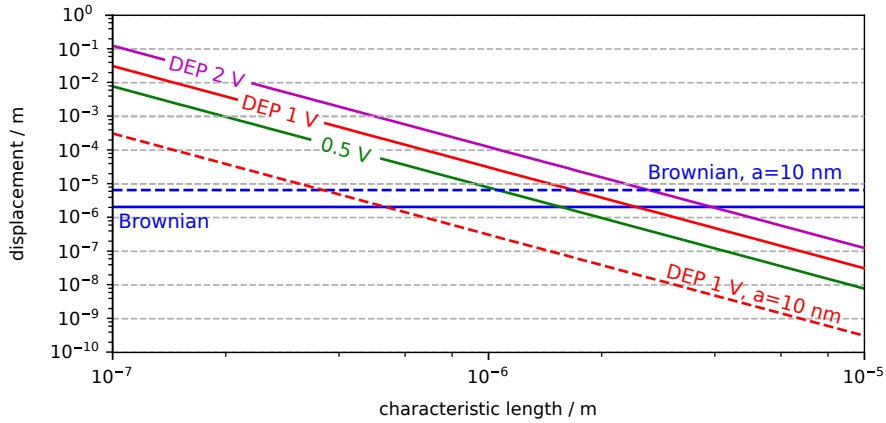


Figure 3.4: Particle displacements in 1 s versus the characteristic length for Brownian motion and DEP forces. The displacements were calculated using the equations listed in table 3.1. For all curves the parameter values $T = 298$ K, $\eta = 1 \cdot 10^{-3}$ Pa \cdot s, $\varepsilon_m = 80 \cdot \varepsilon_0$ and $\varepsilon_p = 8 \cdot \varepsilon_0$ [106] were used. The green, red and magenta lines show the corresponding displacements for values of 0.5 V, 1 V and 2 V for V_{rms} , respectively. The solid lines are calculated with $a = 100$ nm and the dashed lines with $a = 10$ nm. In all cases a geometry of $b = c = 1/10 \cdot a$ was assumed.

DEP can work on a micrometer scale. This length becomes significantly shorter for smaller particles. Here higher voltages would be required. Similar results were found by Tuukanen et al. in 2007 for the trapping of 100 bp dsDNA molecules[107].

Apart from Brownian motion, the electrothermal fluid flow can have a major impact on DEP experiments. Figure 3.5 shows the electrothermal displacement in 1 s for solutions of different salt concentrations. To keep the electrothermal displacement, which interferes the DEP trapping, small a low conducting buffer solution is required. High frequency values can also help mitigate electrothermal effects.

The displacement due to electro-osmosis shows a similar behavior as the electrothermal effect. The influence of EO for different solutions and frequencies is shown in figure 3.6. However, the conductivity of the solution has only a minor effect. EO effects can be avoided using sufficiently high frequencies.

3.2.3 DEP Trapping Recipe

The DNA origami structures are stored in a buffer solution containing 20 mM $MgCl_2$. To avoid interference with electrothermal and electro-osmotic effects, the

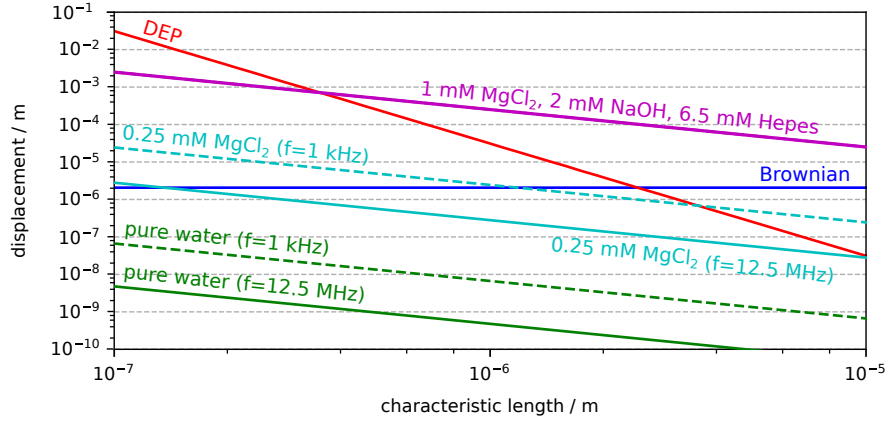


Figure 3.5: Particle displacements in 1 s due to electrothermal forces versus the characteristic length for various solutions. The displacements are shown for frequencies values of 12.5 MHz and 1 kHz. For the 1 mM MgCl₂, 2 mM NaOH and 6 mM Hepes (sol2) solution, the displacements at these frequencies are almost identical. The parameter values $\sigma_{\text{H}_2\text{O}} = 5.5 \cdot 10^{-6} \text{ S/m}$, $\beta_{\text{H}_2\text{O}} = 52.97 \cdot 10^{-3} \text{ K}^{-1}$ [108], $\sigma_{\text{sol1}} = 3.14 \cdot 10^{-3} \text{ S/m}$, $\beta_{\text{sol1}} = 22.5 \cdot 10^{-3} \text{ K}^{-1}$ [109], $\sigma_{\text{sol2}} = 347 \cdot 10^{-3} \text{ S/m}$ and $\beta_{\text{sol2}} = 21.1 \cdot 10^{-3} \text{ K}^{-1}$ [80] were used for pure water, a 247 μM MgCl₂ solution (sol1) and the sol2 solution, respectively. Other parameter values are $T = 298 \text{ K}$, $b = c = 1/10a = 10 \text{ nm}$, $V_{\text{rms}} = 1 \text{ V}$, $\eta = 1 \cdot 10^{-3} \text{ Pa} \cdot \text{s}$, $\kappa = 0.59 \text{ Wm}^{-1}\text{K}^{-1}$, $\varepsilon_m = 80 \cdot \varepsilon_0$, $\varepsilon_p = 8 \cdot \varepsilon_0$ and $\alpha = 4.53 \cdot 10^{-3} \text{ K}^{-1}$ [110]. For salt concentrations $C \ll 1 \text{ M}$, discrepancies in permittivity between the different solutions can be neglected[111].

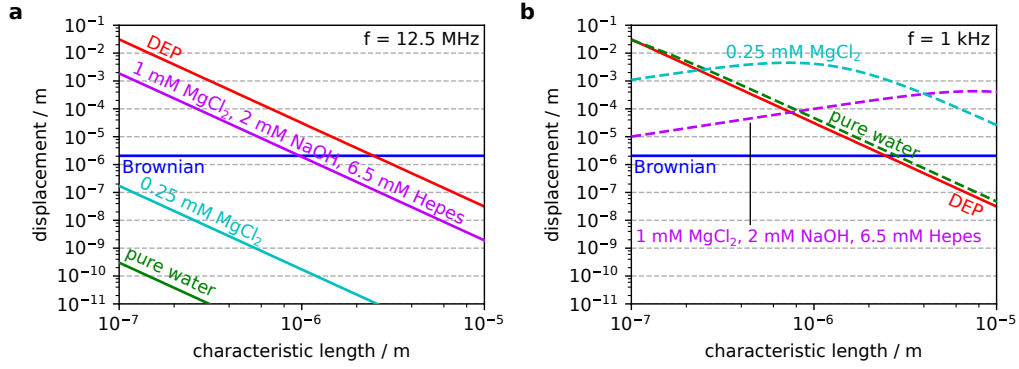


Figure 3.6: Particle displacements in 1 s due to electro-osmosis versus the characteristic length for various solutions. The EO displacements in figure **a** and **b** were calculated using equation for AC electro-osmosis from table 3.1 for $f = 12.5$ MHz and $f = 1$ kHz, respectively. The used parameters are $\sigma_{\text{H}_2\text{O}} = 5.5 \cdot 10^{-6}$ S/m, $\sigma_{\text{sol1}} = 3.14 \cdot 10^{-3}$ S/m, $\sigma_{\text{sol2}} = 347 \cdot 10^{-3}$ S/m, $T = 298$ K, $b = c = 1/10a = 10$ nm, $V_{\text{rms}} = 1$ V, $\eta = 1 \cdot 10^{-3}$ Pa \cdot s, $\kappa = 0.59$ Wm $^{-1}$ K $^{-1}$, $\epsilon_m = 80 \cdot \epsilon_0$ and $\Lambda = 0.25$ [76].

DNA origami structures are transferred into pure water before DEP trapping is performed. This is accomplished via spin-filtering in 3 steps. Each step includes a 1:11 dilution, resulting in a final 15 μM MgCl $_2$ concentration. Amicon® Ultra 100K centrifugal filters from Merck KGaA were used for this purpose.

The nanoelectrode chips are cleaned in an oxygen plasma prior to the trapping procedure. This removes light organic impurities from the surface. The electrodes were connected to the measurement instrument via mechanical pressing with metallic probes. To prevent drying during the DEP procedure, the sample stage was placed in a water-saturated environment. A sinusoidal AC voltage with 1 V_{rms} and 12.5 MHz[10] was applied to the electrodes. A 3 μl droplet of DNA origami structures, suspended in the trapping buffer, was then applied on the nanoelectrodes. After a trapping time of 5 min, the voltage was shut off. The electrodes were short-circuited against each other. This prevents high voltage stress due to electrostatic discharge. The sample was then dried in a nitrogen stream.

3.3 λ -DNA Bridge Preparation

DNA can be suspended between electrodes to form a free-hanging bridge. The electrodes are elevated from the substrate by an intermediated layer of photoresist.

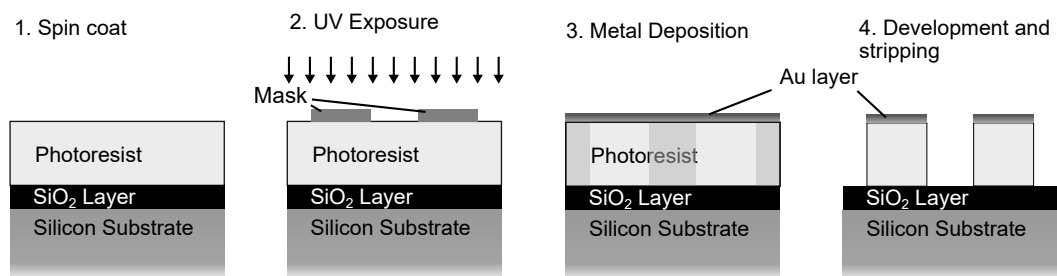


Figure 3.7: Production steps of microelectrodes on top of a photoresist layer

Interactions with the substrate, which can decrease charge transport properties of the DNA, are therefore prevented. This method was developed by Sam Kassegne et al.[11].

3.3.1 Microelectrodes

Interaction with the substrate can have a major impact on the helical structure of a DNA molecule. This interaction can be avoided with free hanging structures, which require special electrode chips as shown in figure 3.7. Here the electrodes are not deposited directly onto the substrate. Instead an additional layer of photoresist acts as a spacer between the electrode and substrate material. The photoresist layer is only present underneath the electrode areas. DNA strands connected to the electrodes can therefore form a free hanging bridge.

The electrode chips were acquired from Sam Kassegne at the San Diego State University. A detailed description of the manufacturing process can be found in [11].

3.3.2 Trapping Recipe

The gap region is first incubated with a solution, containing short double stranded oligonucleotides. These are functionalized with thiol groups. Prior to incubation, the oligonucleotide solution is run through tris(2-carboxyethyl)phosphine (TCEP) gel for thiol reduction[113]. The oligonucleotides form a self-assembled monolayer (SAM), covering the entire gap region. Afterwards the remnants are removed by drying the chip in a nitrogen stream. This is followed with a second incubation step with DNA ligase and long dsDNA molecules. For the former, the Rapid DNA Ligation Kit from Thermo Fisher[114] was used. For the latter, linear λ -DNA molecules with 48 kbp,

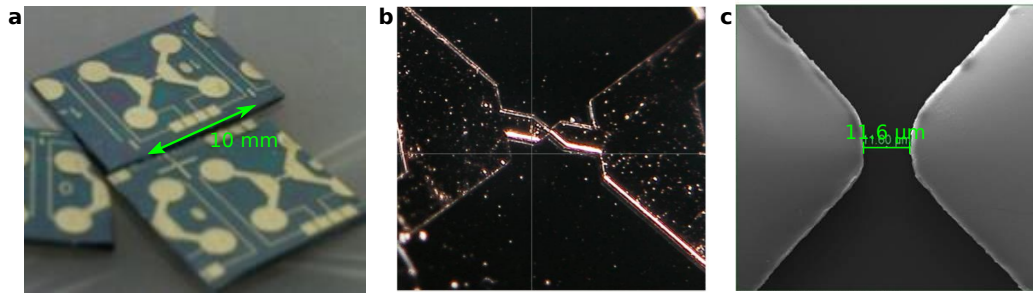


Figure 3.8: Photographs and SEM image of microelectrode chips. Images **a** and **b** show photographs of multiple microelectrode chips after production and a single gap, respectively. The SEM image **c** shows an electrode gap with the brighter areas showing the gold electrodes. All images were taken from [112].

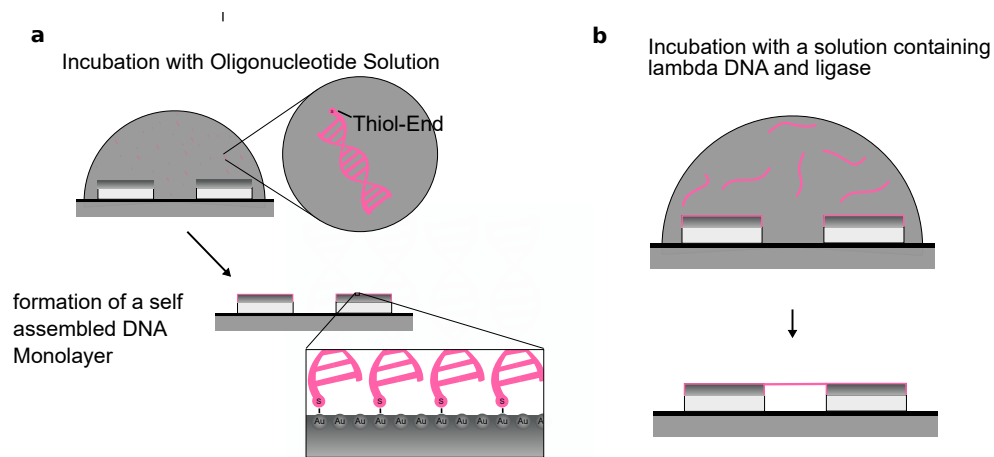


Figure 3.9: Illustration of the principle of DNA bridge preparation

purchased from New England Biolabs[115], were employed. These are about $12\ \mu\text{m}$ in length as is the gap between the electrodes. Prior to usage, the λ -DNA strands were end repaired to be blunt ended, using the End-It DNA End-Repair Kit from Biozym Scientific[116]. The incubation time is one hour. During that time, the λ -DNA can combine with the oligonucleotides in the SAM. The ends of the two DNA molecules attach through the DNA ligation process[117]. A bridge is formed if one strand attaches on both sides. During the incubation, an electric voltage of $1\ \text{V}_{\text{rms}}$ is applied to the electrodes for 30 s in steps of 15 minutes. This attracts the strands towards the electrode gap (see section 2.3.1), increasing the chance of successful capture. The number of DNA strands, getting attached to both electrodes varies stochastically. It can be influenced by the concentration of the λ -DNA solution. After the trapping procedure, the chip is rinsed with ultrapure water and dried in a nitrogen stream.

3.4 Electrical Impedance Spectroscopy

3.4.1 Lock-in Amplifier

The lock-in technique allows for the measurement of small signals hidden in a noisy background[118, 119]. This is achieved by using a reference signal. In a first step the noisy input signal is multiplied with the reference signal. This first step is often called down-mixing or heterodyne/homodyne detection. The multiplied signal is then fed through an adjustable low-pass filter. This filter isolates the signal at the frequency of interest from all other frequency components. The second step is called demodulation or phase-sensitive detection. The reference signal can either be generated by the lock-in amplifier itself or must be provided by an external source[120].

For the application of a lock-in amplifier, the signal of interest has to have a known frequency and stable phase[121]. DC signals can also be measured, if they can be modulated with an AC reference signal[121]. For the latter, usually a sine wave is used[120]. Here demodulation enables selective measurements at the fundamental frequency or its harmonics. Square waves can also be used as the reference signal. However, beside the fundamental frequency, all odd harmonics of the signal are also captured. This can potentially introduce measurement errors.

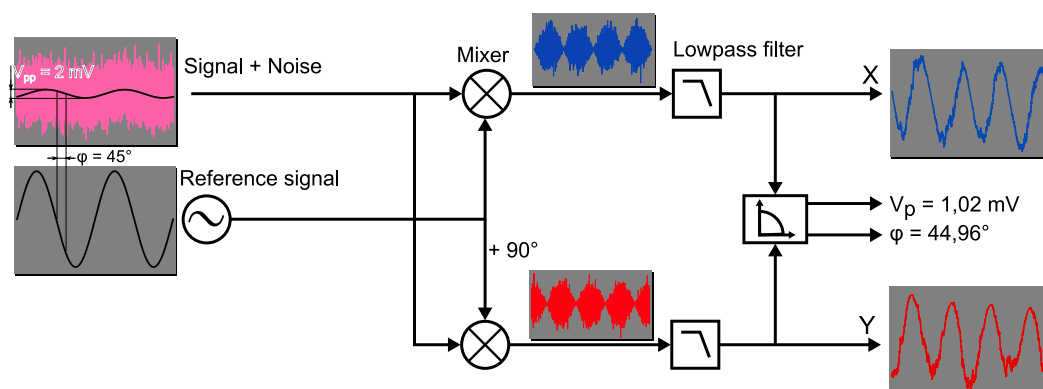


Figure 3.10: Principle of operation of a lock-in amplifier

3.4.2 Measurement Setup

The measurement setup is configured for characterization of DNA via electrical impedance spectroscopy. DNA samples typically have high electrical impedance values. However, the application of high voltages has to be avoided as it could lead to the destruction of the sensitive electrodes, or modification of the DNA itself[122]. These requirements can be met when a lock-in amplifier is employed. The AC voltage applied to the sample acts as the reference signal. The lock-in amplifier measures the current answer at the same frequency (see subsection 3.4.1).

Two electrical impedance spectroscopy setups were used in this work. These are shown in figure 3.11. The earlier setup used an external voltage source in combination with a lock-in amplifier. A Keysight 33210A waveform/function generator[123] was used as the voltage source. This provided the sine voltage applied to the sample. For current measurement, an Ametek 7230 DSP lock-in amplifier[124] was used. As shown in 3.11 a), source, lock-in amplifier and sample were connected in line. The voltage source also provides a TTL trigger signal, as reference signal for the lock-in amplifier.

Later experiments used a MFLI lock-in amplifier from Zurich Instruments[125]. This device incorporates a lock-in amplifier as well as a signal generator. The reference signal is therefore internally provided. The MFLI also has a lower input impedance than the Ametek 7230. Especially for impedance measurements, this input impedance is the major source of uncertainties. The setup is illustrated in figure 3.11 b). During the recording of an impedance spectrum, 10 measurements are taken per frequency value. The average value and bias-corrected standard deviation is calculated by gen-

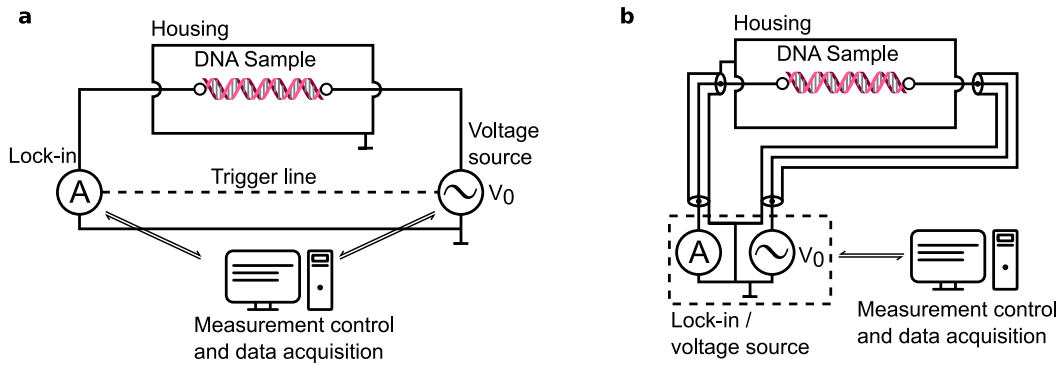


Figure 3.11: Measurement setups for impedance spectroscopy

erating a histogram from the measured values and fitting a normal distribution[125]. If not stated otherwise, spectra shown in this work were measured using the MFLI lock-in amplifier.

In both setups, the voltage V_0 is applied to the sample and the lock-in amplifier in series. The sample is mounted in a sample holder inside a metal housing. Copper spring contacts are employed to connect the electrodes to the measurement circuit. The impedance spectrum of the sample holder is shown in figure 3.12. The spectrum resembles that of a capacitor with an effective capacity of 3.5 fF. The drop in phase around 10 kHz and 500 kHz is caused by the input impedance of the Lock-In amplifier. The amplification of the input signal was decreased above 10 kHz. This also decreases the input impedance, causing the jump in the spectrum at 10 kHz.

A sample, consisting of an electrode chip and the DNA material, is connected parallel to the setup capacitance. In this work DNA origami structures and λ -DNA molecules are used as samples. The two samples types employ electrode chips of different composition. The main difference is an additional photoresist layer between the electrodes and substrate material for the λ -DNA samples. Therefore, the chips vary in their impedance characteristics.

In both cases the empty chips (i.e. electrode chips without DNA) display a much higher effective capacitance than the sample holder. This is caused by the chip geometry. The sandwiched structure of gold electrode pads, insulating layer and silicon substrate form a capacitor.

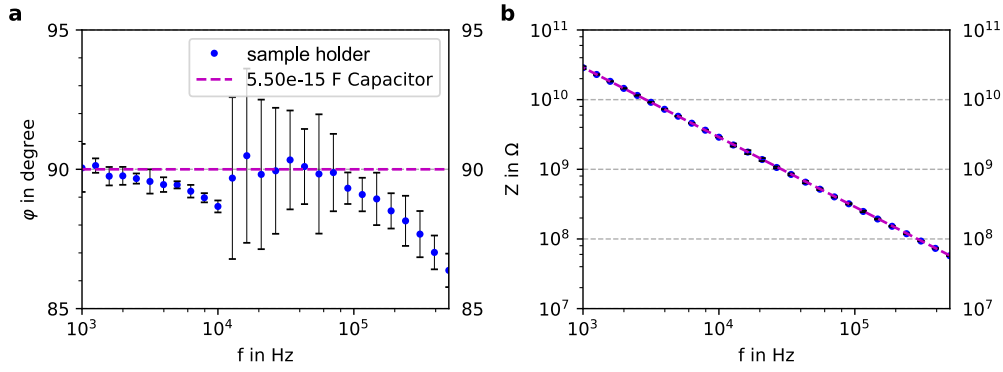


Figure 3.12: Impedance spectra of the sample holder and an empty electrode chip. Graph **a** shows the phase and **b** the corresponding impedance value over the frequency for the measurement setup without an electrode chip. The magenta line represents the impedance spectrum of a 3.5 fF capacitor. Error bars represent the 95% confidence interval (CI).

Nanoelectrode Chips

The nanoelectrode chips have a 600 nm insulating SiO_2 layer. The pad areas have a size of 0.275 mm^2 each. Considering a parallel plate capacitor, the capacitance can be calculated using

$$C = \varepsilon_0 \varepsilon_r \frac{A}{d}. \quad (3.1)$$

In this case, the capacitance for one electrode-substrate configuration would amount to around 16 pF. Both capacitances are in series, amounting for a total capacitance of 8 pF. The measured impedance spectrum is shown in figure 3.13. The spectrum does indeed mainly resemble that of a capacitor. The capacitance is approximately half of the calculated value of 8 pF. This deviation is most likely caused by the finite resistivity of the silicon substrate. The drop around 1 kHz can be explained by multiple parallel stages of capacitors and resistors in series. Due to the planar geometry of the electrodes and the substrate, the current path from electrode to electrode is not the same everywhere. Therefore, multiple parallel stages are required to describe the characteristics. Here only two parallel stages were used. For even more stages the simulated curve would converge even more to the measured spectrum.

The second stage consists of the capacitor C_2 in series to the resistor R_2 . The latter represents the ohmic resistance of the silicon substrate. A $1.4 \text{ k}\Omega$ resistance value

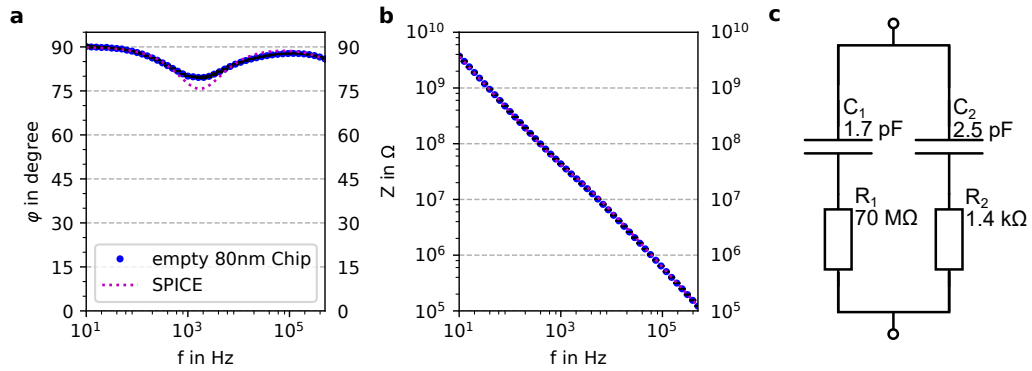


Figure 3.13: Impedance spectrum of an empty nanoelectrode chip. Graphs **a** and **b** show the phase and impedance values over the frequency for an empty nanoelectrode chip. The magenta line represents the impedance spectrum of a equivalent circuit shown in image **c**. The values for the equivalent circuit were calculated using the simulation program with integrated circuit emphasis (SPICE) software LTspice from Linear Technology. Uncertainty bars represent the 95% confidence interval.

fits the measured spectrum of the nanoelectrode chip and is realistic for the present geometry.

The electrodes themselves also have an ohmic resistance. To determine this resistance, reference chips without electrode gaps were manufactured. That means that the fingertip electrodes were one continuous nanostructure, electrically connecting the electrode pads. The resistances of these chips were measured with a Fluke 79III handheld multimeter and amounted to 450 Ω . It can be assumed that the major contribution to this resistance comes from the continuous fingertip electrode, due to its small cross section. In a regular electrode chip the DNA would, therefore, be connected parallel to the chip's capacitance and in series to the so determined electrode resistance, as shown in figure 3.14.

Voltage loss can occur during measurements, causing the voltage at the sample to deviate from the voltage applied by the voltage source. These deviations can be estimated by using the equivalent circuit in figure 3.14. The measurement devices allow measurements in the frequency range up to 500 kHz. The actual deviation depends on the sample resistance. This is especially important for low resistance values. Above 1 M Ω , the deviation is minuscule.

The voltage losses can also be relevant for DEP trapping, since a reduced voltage at the electrodes results in weaker DEP forces. For DEP trapping, higher frequencies of

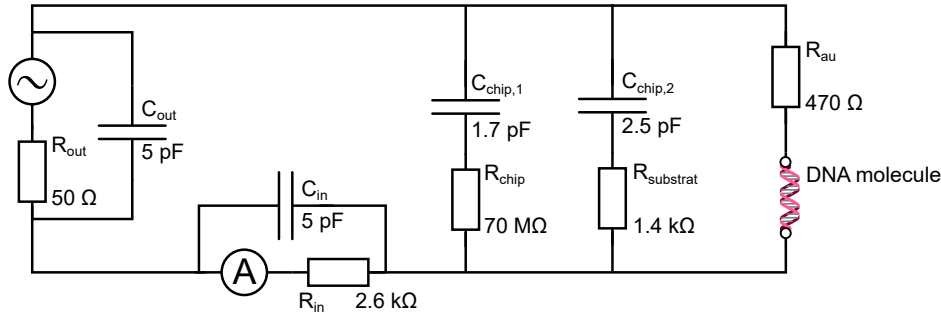


Figure 3.14: Equivalent circuit of the nanoelectrode measurement setup

around 10 MHz are used. Additionally, a water droplet of a few microliter is applied to the gap region. This affects the electrical characteristics of the setup, as can be seen in figure 3.15. As was the case for the empty chip, a multiple stages model would provide a better agreement with the measured spectrum. The additional 7 nF capacitance in the equivalent circuit in figure 3.15 is most likely caused by an electrical double layer at the metal/fluid border. The 5 M Ω resistor is the electrical resistance of the fluid. Due to this resistance, the contribution of EDL capacitance to the total impedance is minuscule at frequencies higher than 100 kHz. For these higher frequencies only a slight shift by 0.5 pF can be measured.

The voltage across the electrode gap can be estimated, using the equivalent circuit depicted in figure 3.15 c by means of a SPICE simulation. If only the sample holder and the electrode chip are used, the voltage loss is again negligibly small.

DEP experiments by Shen et al. [10], showed regular destruction of the electrodes. This was most likely caused by high currents during DEP trapping. A series resistor can be used to suppress such high currents. Such a resistor, however, can cause a significant voltage loss. In this case, the necessary electric field strength for DEP trapping may not be reached. The loss can be compensated, by a higher applied voltage. The loss and necessary compensation voltage values for this setup are displayed in figure 3.16.

Microelectrode Chips

The microelectrodes were fabricated on a silicon substrate with a 1.5 μm layer of SiO₂. In contrast to the nanoelectrode chips described above the microelectrodes

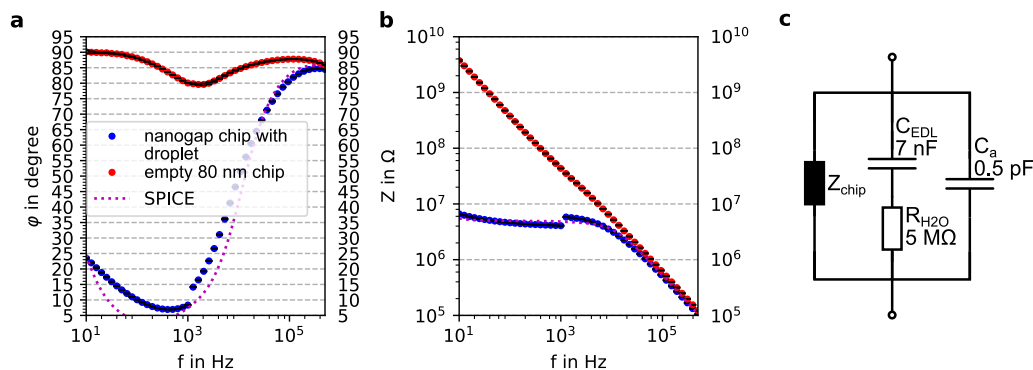


Figure 3.15: Impedance spectrum of an empty nanoelectrode chip and one with a $3 \mu\text{l}$ droplet of water. Graphs **a** and **b** show the phase and impedance values over the frequency for two nanoelectrode chips. The blue line represents a chip with a $3 \mu\text{l}$ droplet of Milli-Q[®] water applied to the gap region. The red line represents an empty nanoelectrode chip. The magenta line represents the impedance spectrum of an equivalent circuit shown in image **c**. The values for the equivalent circuit were calculated using the SPICE software LTspice. Error bars represent the 95% CI.

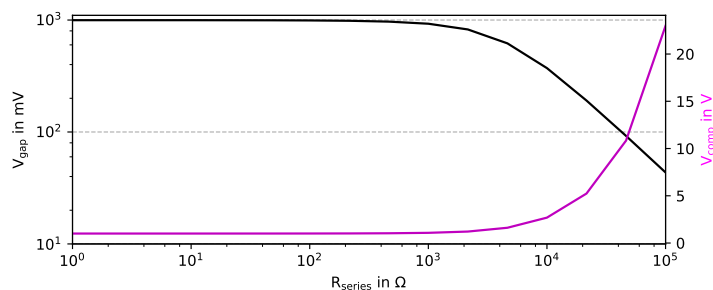


Figure 3.16: Voltage loss arising due to the usage of a series resistor. Gap voltage V_{gap} and compensation voltage V_{comp} as a function of the value of the series resistor R_{series} . The values are calculated using a SPICE simulation. The simulation was performed for an applied voltage of 1 V, which is also the effective voltage that shall be achieved by means of the compensation voltage.

3.4. Electrical Impedance Spectroscopy

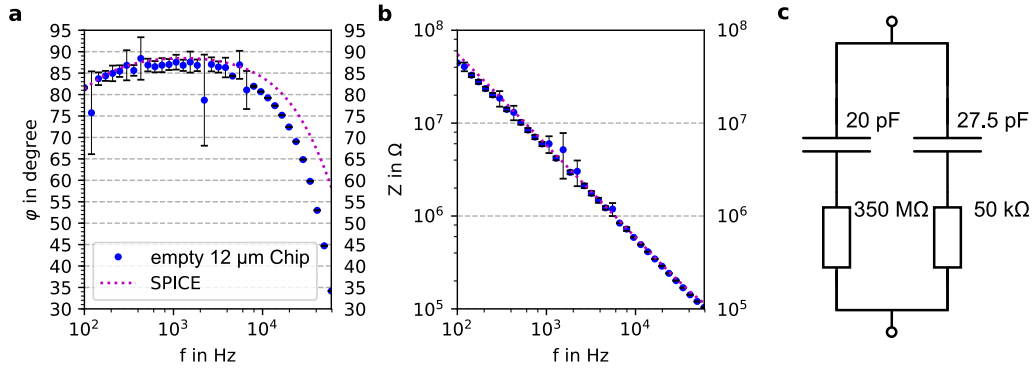


Figure 3.17: Impedance spectrum of an empty microelectrode chip. Figures **a** and **b** show the phase and impedance values over the frequency for an empty microelectrode chip. The dotted magenta line represents the impedance spectrum of an equivalent circuit shown in image **c**. The values for the equivalent circuit were calculated using the SPICE software LTspice. Uncertainty bars represent the 95% confidence interval.

have an additional layer of photoresist between the gold electrodes and the silicon oxide surface. The photoresist layer has a height between 50 μm and 100 μm . The electrode surface of a single electrode has an area of around 12 mm^2 . Using equation 3.1 and considering the serial circuit configuration, a capacitance around 4 pF is expected. The measured spectrum is shown in figure 3.17.

λ -DNA Experiments

Measurements with λ -DNA samples and the experimental results will be described in this chapter.

The samples were delivered by San Diego State University. A sample comprised a silicon chip with a SiO_2 surface layer, gold electrodes and the DNA material. The electrodes are manufactured on top of a photoresist layer. This layer acts as a spacer between the substrate surface and the electrodes. The latter are covered with short, thiolated oligonucleotide. 12 μm long λ -DNA strands form a free hanging rope between the two electrodes. A description of the sample preparation is given in section 3.3.

These samples have a typical impedance of several $\text{M}\Omega$ but can vary in their impedance spectra. Figure 4.1 shows the impedance spectra of a few selected samples. Differences between the samples can arise from varying numbers of attached strands and incomplete formations of electrical contacts. The number of DNA molecules depends on the concentration of λ -DNA used during the preparation[11].

The λ -DNA samples were exposed to radiation of different quality. During irradiation the impedance spectra were continuously measured. In all cases, a reference sample was measured simultaneously. The reference samples were not exposed to the radiation but were kept in the same environments as the irradiated samples.

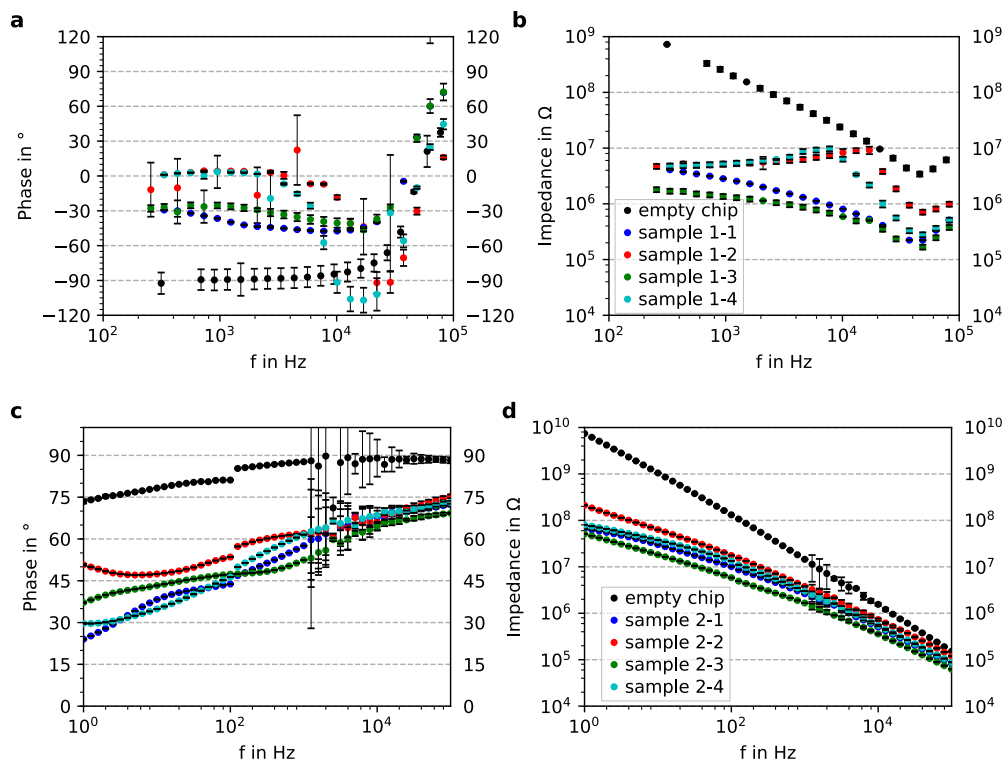


Figure 4.1: Impedance spectra of λ -DNA samples. Figures **a** and **c** show the phase and **b** and **d** the impedance values for different DNA samples against the frequency. The samples 1-1 to 1-4, shown in figures **a** and **b**, are from an earlier batch and measured with the setup utilizing the Ametek 7230 DSP lock-in amplifier. The samples 2-1 to 2-4, shown in figures **c** and **d**, are from a later batch and measured with the setup utilizing the MFLI lock-in amplifier. Uncertainty bars represent the 95% confidence interval.

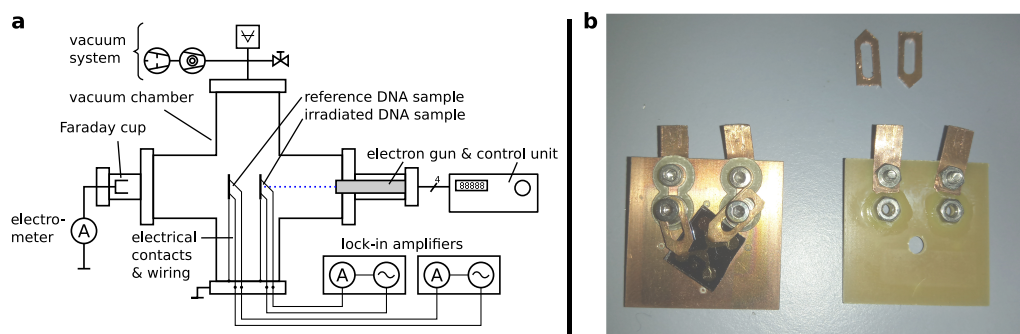


Figure 4.2: Experimental setup for electron irradiation of DNA. Image **a** shows a sketch of the experimental setup with the major components. The photograph in **b** shows the sample holders with electrical contacts to the DNA samples. These were placed in a metallic rack inside the vacuum chamber. Both the rack and the copper surfaces of the sample holders were grounded.

4.1 Irradiation with Electrons

4.1.1 Setup

An EQ 22/35 electron gun purchased from SPECS Surface Nano Analysis GmbH [126] was used as a radiation source. The operation of the electron gun requires a vacuum with a pressure below 10^{-5} Pa. Both the irradiated and reference samples were mounted in the same vacuum chamber. The reference sample was placed behind the sample holder of the irradiated sample. The impedance spectra of the samples were measured using the MFLI lock-in amplifiers before and after the irradiation. The electric currents due to the electron beam did not allow for measurements during irradiation.

The electron beam direction was adjusted before each irradiation using a Faraday cup and an aperture at the position of the irradiated sample. The irradiation was done with 1 keV electrons. During the irradiation, the focused beam was scanned over a 10 mm by 10 mm area. The center of this area was aimed at the electrode gap of the irradiated sample. The electron flux was $2.5 \cdot 10^9 \frac{1}{\text{s} \cdot \text{mm}^2}$. The irradiation time was 5 min per irradiation cycle. Considering a target area of 10 nm by 12 μm , 90,000 primary electrons are expected to hit the target in five minutes.

4.1.2 Results

A change of impedance is expected when the DNA is brought in a vacuum, due to the absence of humidity. However, the DNA samples showed irreversible changes when brought back into an air-filled environment.

Figure 4.3 shows the change of the impedance spectra of an irradiated and a reference sample over multiple irradiation cycles. After each irradiation the vacuum chamber was vented with air. The spectra in figure 4.3 were measured after the sample was kept in air for several hours afterwards.

Changes in impedance occurred in both the reference and irradiated samples. The biggest change happened during the first irradiation cycle. This was the case for both samples and found repeatedly when samples were placed inside a vacuum. After this step, the spectra deviated only slightly from that of an empty chip. This change was irreversible. It is therefore most likely that the DNA bridges were at least partially destroyed during either evacuation or venting of the vacuum chamber. Slight changes toward a more capacitive behavior are observed every time when the samples are introduced into a vacuum.

The conclusion is that λ -DNA samples do not remain intact under vacuum conditions. Samples with DNA origami structures thus might be better suited for experiments in vacuum.

4.2 Irradiation with Alpha-Particles

4.2.1 Am-241 Source

Experimental Setup

Irradiation was performed using a ^{241}Am source. The experimental setup is shown in figure 4.4. Both, source and samples, were kept in air at room temperature. The reference sample was shielded from the radiation by an aluminum plate.

A ^{241}Am naturally emits α -particles with an average energy of 5.485 MeV. The source, used for the experiments, is sealed with a 10 μm thick mylar foil, causing an energy loss of the radiation. The sealed ^{241}Am source emits α -particles with an average energy of 3.5 MeV. DNA sample and source had a distance of 2 cm. At this distance, the energy of the α -particles impinging on the DNA was reduced to

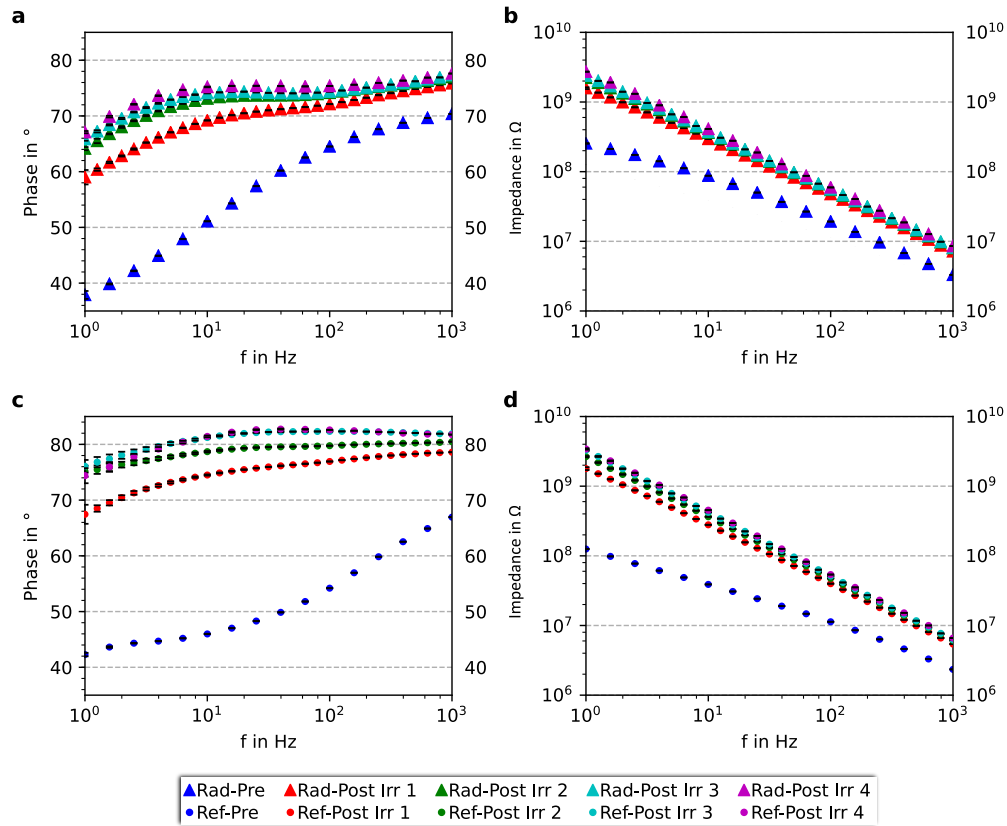


Figure 4.3: Frequency dependence of the phase (a, c) and impedance (b, d) of λ -DNA samples. The triangles represent a sample which has been irradiated with 1 keV electrons and the dots represent the unirradiated reference sample. The blue symbols refer to both samples before irradiation. The red, green, cyan and magenta symbols refer to the samples after each successive irradiation cycle. The samples were irradiated in a vacuum with the reference sample being present in the same vacuum chamber during irradiation but shielded from the electron beam. The measurements of the impedance spectra were performed in an ambient air atmosphere.

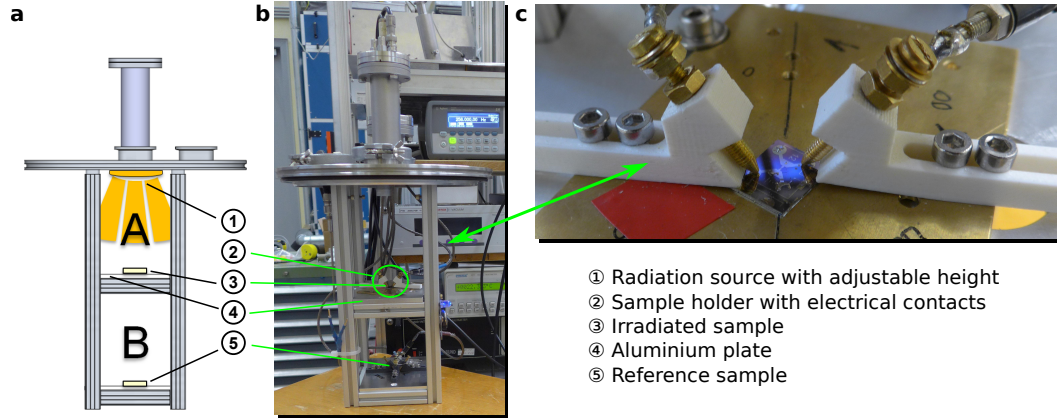


Figure 4.4: Sketch and photographs of the experimental setup for the irradiation with the ^{241}Am source. Image **a** shows a schematic view and **b** a picture of the setup. The closeup photograph **c** shows the sample, sample holder and electrical contacts.

150 keV. The reduction in energy resulted from the energy loss in the air gap. This energy loss was calculated using the SRIM code[127].

The ^{241}Am source had an activity A of 0.5 MBq. The radiation was emitted isotropically. Assuming a point source, the average rate of incoming particles \dot{n} is approximately given by

$$\dot{n} = A \cdot \frac{F_{\text{DNA}}}{F_{\text{sphere}}}, \quad (4.1)$$

where F_{DNA} is the area of the DNA sample and F_{sphere} the surface area of a sphere with a radius equal to the distance between the source and the sample. Equation 4.1 can also be expressed by using the solid angle Ω_{DNA} covered by F_{DNA} as

$$\dot{n} = A \cdot \frac{\Omega_{\text{DNA}}}{2\pi}. \quad (4.2)$$

The DNA sample was assumed to have a length of 12 μm and a width of 10 nm, resulting in a rate of incoming particles \dot{n} of about $1.08 \cdot 10^{-7}\text{s}^{-1}$. This is roughly one particle hitting the DNA directly every 24h in average. The samples were continuously irradiated for 28 days. The measurements were conducted in air at room temperature.

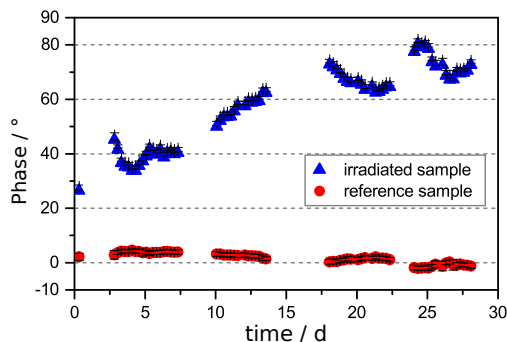


Figure 4.5: Temporal development of the phase response during irradiation with the ^{241}Am source. The data points represent the average values of the phase response for frequencies ranging from 250 Hz to 350 Hz. Gaps in the timeline were caused by instrument failure due to technical difficulties.

Results

Figure 4.5 shows the temporal development of the phase response of the samples with and without irradiation. The reference sample did not exhibit a change in general trend. The irradiated sample, however, showed an impedance spectrum closer to a capacitor after irradiation. This suggests that the irradiated DNA was destroyed. Figures 4.6 **a** and 4.6 **b** show the impedance and phase response of the irradiated sample (Rad) and the reference sample (Ref) before and after irradiation, respectively. After the irradiation time, the reference sample exhibited a higher impedance, which was probably caused by aging of the DNA strands. This aging leads to an increase of the ohmic resistance. In the case of a high ohmic resistance, capacitors play a dominant role already at low frequencies. Such behavior is responsible for the drop in phase and impedance that can be seen above 1 kHz. The irradiated sample, on the other hand, showed a capacitive behavior similar to that of an empty chip. This indicates that the reference sample as well as the irradiated sample had undergone degradation over time. The irradiated sample, however, degraded at a much faster rate, barely conducting current after the irradiation. This change in electrical properties is demonstrated in Figure 4.6 **b** - 4.6 **e**. Diagrams (**a**) and (**b**) show the equivalent circuits of the experiments. For better understanding, the circuits have been simplified to qualitatively demonstrate the influence of major components on the output signal. Figures 4.6 **c** and 4.6 **d** show the calculated signals in comparison to the measured data.

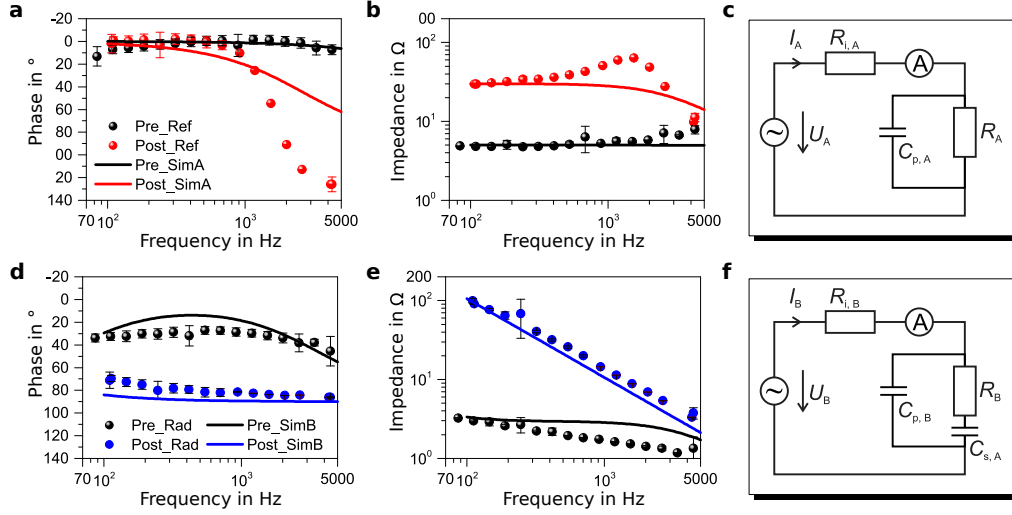


Figure 4.6: Frequency dependence of the phase and impedance of an irradiated (Rad) and reference (Ref) sample before and after irradiation with the ^{241}Am source. Images c and f show the corresponding simplified equivalent circuits of the experiments with the reference sample and irradiated sample, respectively. Here, $R_i = R_{i,A} = R_{i,B} = 100\ \Omega$ represents the input resistances of the lock-in amplifiers measuring the currents I_A and I_B . R , C_p and C_s represent the electrical quantities for the DNA samples, including the electrode chip. The resistance R_A increased during the measurement time from $5\ \text{M}\Omega$ to $30\ \text{M}\Omega$, while its parallel capacitor $C_{p,A}$ increased from $0.7\ \text{pF}$ to $2\ \text{pF}$. Simultaneously, the resistance of the irradiated sample R_B increased from $3\ \text{M}\Omega$ to $1\ \text{G}\Omega$, while $C_{p,B} = 15\ \text{pF}$ and $C_{s,B} = 1\ \text{nF}$ remained the same. The solid lines in the graphs show the calculated frequency dependencies calculated using the SPICE software LTSpice in comparison to the measured data.

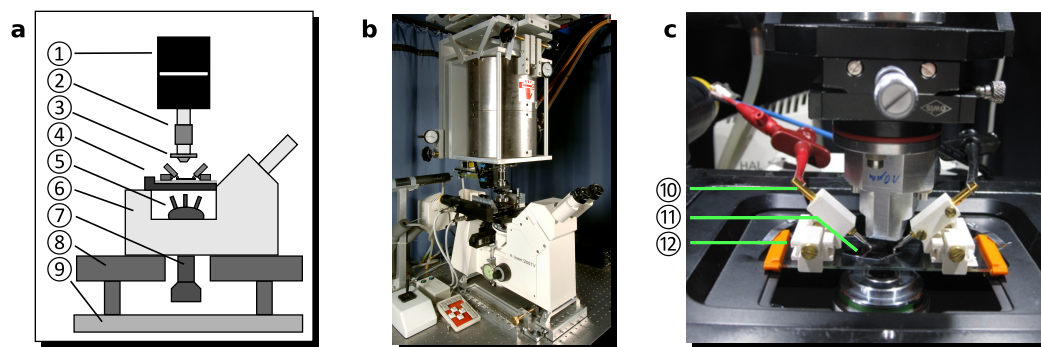


Figure 4.7: Setup for the microbeam irradiation. Image **a** shows a sketch and **b** a photograph of the setup for the microbeam experiment. A closeup photograph of the sample holder is shown in **c**. 1. Quadrupole doublet. 2. Bellows for vertical movement. 3. Vacuum window. 4. X-Y-stage. 5. Objective turret and detectors. 6. Inverse microscope. 7. CCD camera. 8. Optical table. 9. Basement floor. 10. Spring contacts. 11. DNA sample. 12. Glass slide.

4.2.2 Microbeam Facility

Experimental Setup

The measurements were also conducted with 8 MeV alpha particles produced by a microbeam[128]. The microbeam is capable of producing a narrow beam with a diameter of only a few micrometers with high precision. Due to this focused beam, a much higher rate of direct hits on the DNA target can be achieved, in contrast to the irradiation with the ^{241}Am source. AC impedance spectroscopy was, once again, used to measure the electrical properties of DNA samples during irradiation. The experimental setup is shown in Figure 4.7. The distance between the DNA sample and the vacuum window was 4 cm. After passing through the vacuum window and 6 mm of air, the alpha particles arrived at the sample with average energies of 5.8 MeV. This energy was calculated using SRIM code. The samples were mounted on glass slides for better positioning. The reference sample was placed approximately 50 cm away from the irradiated sample so that it could not be hit by the radiation. The beam had a diameter of $6\ \mu\text{m}$ in the focus at the exit window and about $130\ \mu\text{m}$ at the position of the DNA target. The rate of particles was 8000 particles per second, such that approximately 120 particles hit the sample per hour. This allowed considerably shorter irradiation times compared to those in the previous experiments with the ^{241}Am source. The duration of the

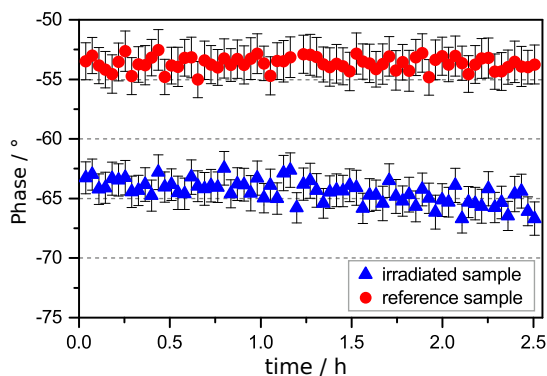


Figure 4.8: Phase response as a function of time for the irradiated and reference sample during microbeam irradiation. The plotted data are averaged values of the phase response for frequencies between 250 Hz and 350 Hz.

irradiation for the measurement was 2.5 h.

Results

The temporal development of the phase response of an irradiated and a reference sample is shown in Figure 4.8. The response of the irradiated sample showed a steady decline, while the response of the reference sample remained constant. The frequency response of an irradiated and a reference sample before and after the irradiation time is shown in Figure 4.9. Unlike the samples in the previous ^{241}Am experiment, the DNA does not appear to be fully destroyed by the radiation. However, a noticeable difference between the response of the irradiated and the reference samples can be seen. During the comparatively short measurement time, the reference sample did not experience a measurable degradation. The irradiated sample, however, exhibited a decrease in the phase response which indicates that the DNA was damaged by the radiation[129, pp. 4-5].

4.3 Conclusions

λ -DNA samples were irradiated with electrons and alpha particles. In the first case, a vacuum environment was necessary to operate the electron source. The vacuum environment lead to a damage of the DNA samples even before radiation exposure. This altered the structure so much that radiation damages had no measurable influence on the conductivity.

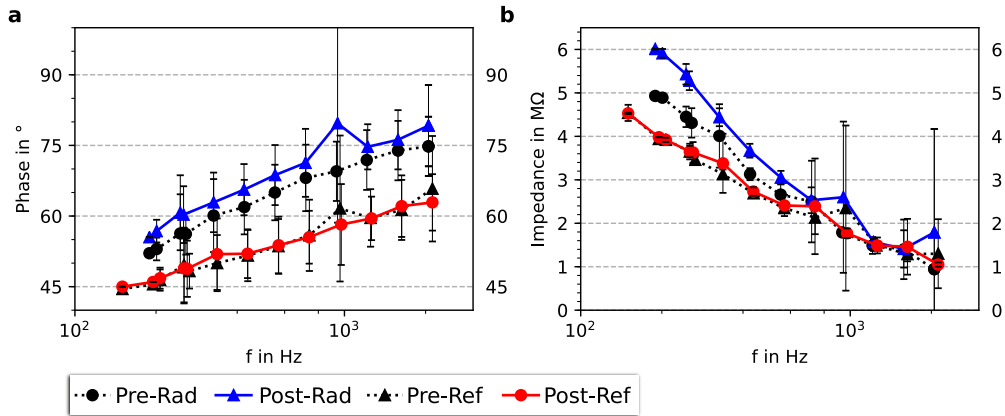


Figure 4.9: Frequency dependency of the impedance (a) and phase (b) of the irradiated (Rad) and reference (Ref) sample before and after irradiation with the microbeam. The duration of the irradiation was 2.5 h.

The irradiation experiments with alpha particles did not need a vacuum environment. Here the samples were kept at room temperature in dry air. Radiation exposure did affect the conductivity. The influence of other environmental factors can be ruled out, since an unirradiated reference sample was measured simultaneously. These reference samples did not exhibit conductivity changes unlike the irradiated samples.

The irradiation with an americium source did show strong effects on the DNA conductivity. After irradiation, the sample did not exhibit ohmic conductivity. Ohmic behavior was still measured for the reference sample. However, it should be noted that the reference sample experienced a decrease in conductivity as well. This was most likely caused by aging processes over the 28 days irradiation time.

Microbeam irradiation experiments were conducted in a much shorter time of a few hours. This was possible by the much higher particle fluence of the microbeam source. In this time, a change towards a more capacitive impedance spectrum was measured. Here no changes in impedance due to aging or other environmental effects were observed.

During the microbeam irradiation an estimated number of 300 alpha particles hit the DNA target directly. Compared to that, only 24 estimated direct hits on the DNA occurred during the 28 days ^{241}Am irradiation. Still, much higher changes in conductivity were measured in the latter case. First, aging of the samples might contribute to this result. Secondly, the alpha particles from the americium source

had a lower energy when arriving at the DNA target. Direct interactions from the 150 keV particles from the ^{241}Am source should have a higher chance of causing DSBs than the 5.8 MeV particles from the microbeam[130]. And third, the comparison so far only amounts for direct interactions.

An estimation of the secondary electron exposure for a comparison between the two sources is not a trivial task. This would require a more elaborate method, like Monte-Carlo track-structure simulation. However, a quantitative comparison would also require samples with reproducible impedance spectra and will therefore be postponed till such experimental results exist.

MD Simulation of microhydrated DNA Bundles

As discussed in chapter 2.2.1, microhydration can have a significant impact on the DNA's molecular structure and, therefore, its charge transport properties. A better understanding of this phenomenon can help mitigate this effect. All impairing effects on the DNA helix can overshadow the effects of radiation damages and are therefore to be avoided when possible.

It was found that bundles of DNA suffer less from these effects than single helices[46, 41]. This suggests that neighboring DNA molecules have a stabilizing effect on each other. To further investigate this effect, different setups of DNA bundles were simulated with molecular mechanics in microhydrated states.

5.1 Setup

The basis is a 51 bp dsDNA with a random sequence as shown in table 5.1. A structure file was generated, using the na-server[131]. This generates an ideal B-DNA in the pdb-file format. The file was then converted into the Gromacs format, using the tools provided by the Gromacs software. If it is not stated otherwise, all steps are performed using tools from the Gromacs software.

To prepare the system, first the strand was placed in the center of a rectangular box with periodic boundary conditions. The size was chosen such that the distances

MD Simulation of microhydrated DNA Bundles

Strand A: 5'-AGC TCT AAT ATG TAG CCC CGA CCC GGG TTG TAT AAA
AAA GGT GTA ACG ACG-3'

Strand B: 3'-TCG AGA TTA TAC ATC GGG GCT GGG CCC AAC ATA TTT
TTT CCA CAT TGC TGC-5'

Table 5.1: Investigated 51 bp sequence for MD calculations

between DNA and the boundary were at least 1 nm. Subsequently the box was filled with water molecules. For the simulation the 3-point SPC-E model[132] was used. Sodium counterions were then introduced into the system to neutralize the negatively charged backbone. This was done by replacing water molecules with the Na^+ -ions, until the system was electrically neutral.

Simulations were performed using the CHARMM27[133] force field. All bonds, which involve hydrogen, were constraint to their preferred length using LINCS[134]. This allowed the usage of a timestep of 2 ps. A Verlet type cutoff-scheme[89] was used for Coulomb and Van der Waals interaction with a cutoff distance of 1 nm. Long range electrostatics were handled with the PME method.

The system was first relaxed by running a steepest-descents energy minimization. In the second step, the system was coupled to a 300 K heat bath using a velocity-rescaling thermostat[135]. Initial velocities were randomly drawn from a Maxwell-distribution at 300 K. This NVT simulation was then run for 100 ps. Subsequently the system was set up in a NPT ensemble. Temperature regulation was realized with a velocity-rescaling thermostat. The pressure was coupled to a Parrinello-Rahman barostat[136]. This regulates the pressure to 1 bar by isotropic scaling of the box dimensions. This last equilibration step was run for 100 ps. The production simulation was then run for 20 ns. The simulation was set up in an NVT ensemble with the same parameters as in the equilibration.

Seven different configurations of DNA bundles were investigated. These are shown in figure 5.1. Starting point was the previously equilibrated 51 bp dsDNA, without ions and water. The molecule was duplicated and shifted by 2 nm in the respective direction. Afterwards the system was solvated, ionized and equilibrated, analog to the single double-strand. Microhydration was achieved by removing water molecules down to a certain number of water molecules per nucleotide. This number N_W was determined by equation 2.1. For each nucleotide, water molecules were sorted by the distance between their O-atom and the P-atom of the nucleotide. Only the closest N_W molecules were chosen to remain. Double picks of H_2O molecules by adjacent

nucleotides was avoided.

The number of ions in the system was kept constant. In DNA molecules and other polyelectrolytes the ion concentration near the surface stays high, especially near the negatively charged phosphate groups[137, 138]. This high local concentration is usually not the same as the ion concentration in the bulk solvent. For low levels of ion concentration, it has been shown that the structural stability of DNA is decreased[139, 140].

All systems were simulated in five microhydrated states. The single dsDNA and the 9-Helix bundle were additionally simulated as a fully solvated system. Table 5.2 gives an overview of these states. The simulations were run for 20 ns. Snapshots of the system coordinates, velocities and energies were taken every 20 ps.

5.2 Results

The snapshots, taken during the simulation, were analyzed using the CURVES+[141] software package. Only the last 10 ns of the simulation were used. The first and last ten base pairs of each strand were also excluded from the analysis. Figure 5.2 shows the occurring helical parameters of a single DNA double helix. The spread of the parameters becomes wider at lower hydration levels. This suggests that the helical structure becomes less stable if fewer water molecules are in its surrounding. Even at high hydration levels, the stability does not reach that of a fully hydrated state.

As previously stated, experiments indicate that the helical stability increases in bundles of multiple DNA strands (see section 2.2.1). A stabilizing effect can be

State	N_W	RH
Micro1	3	< 0 %
Micro2	6	14 %
Micro3	9	76 %
Micro4	12	86 %
Micro5	15	90 %
Fully Solvated	-	> 100 %

Table 5.2: Microhydrated states simulated with molecular dynamics. N_W is the number of water molecules per nucleotide in the system. The corresponding relative humidity RH was calculated with equation 2.1. It should be noted that equation 2.1 is not accurate for $RH > 80$ %.

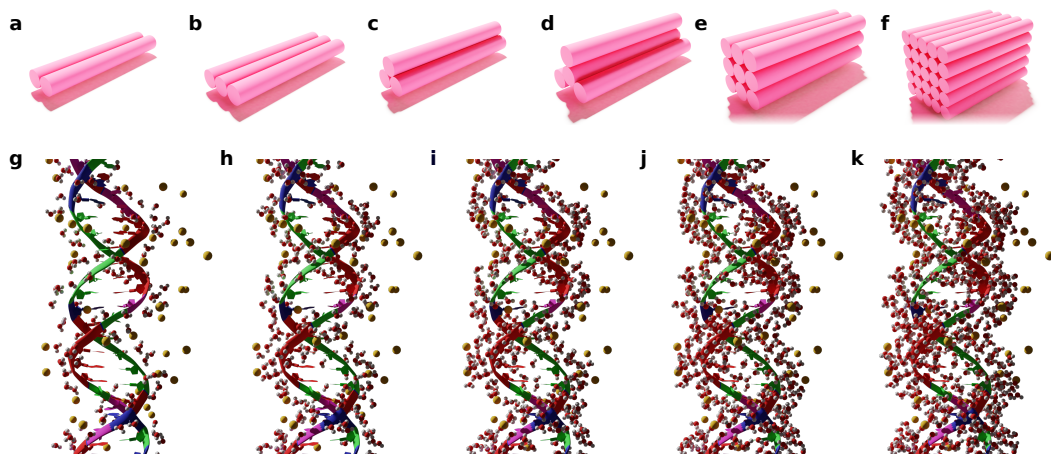


Figure 5.1: DNA configurations studied using MD simulations. Images **a** to **f** illustrate the helix arrangement at the start of the simulations. These will be called two helices (**a**), three helices (**b**), triangle (**c**), tristar (**d**), 9-helix-bundle or 9HB (**e**) and 25-helix-bundle or 25HB (**f**). A section of a single helix at hydration states Micro1 to Micro5 (see table 5.2) is shown in images **g** to **k**.

observed even with two parallel strands, as shown in figure 5.3. The graphs show the distribution of the intrastrand parameters for a single dsDNA and bundles of two and three parallel double strands in the 'micro3' solvation state. These distributions were fitted with Gaussian distributions for easier comparison between the simulation results. The distributions were narrower the more strands were in the simulation. This hints toward a more stable DNA helix. However, none of these setups reached the stability of a fully solvated strand. This was also not achieved for the 'micro5' solvation state at a relative humidity over 80 %.

The results of multilayered DNA structures are shown in figure 5.4. The graphs show the average value and the standard deviation of the Gaussian fits to the individual distributions. The trend of higher stability with a higher number of strands continues. However, the tighter packed 9HB and 25HB structures are more stable than the 'Tristar' setup. Even these show discrepancies in stability at low hydration levels to the fully solvated state. The strands maintain their regular stacking only at high hydration levels.

The parameters shown in figure 5.4 were those of the center strand of the respective bundle. Figure 5.5 shows the helical parameters for strands at different positions in the '25HB' at various hydration levels. It was expected that the strands on

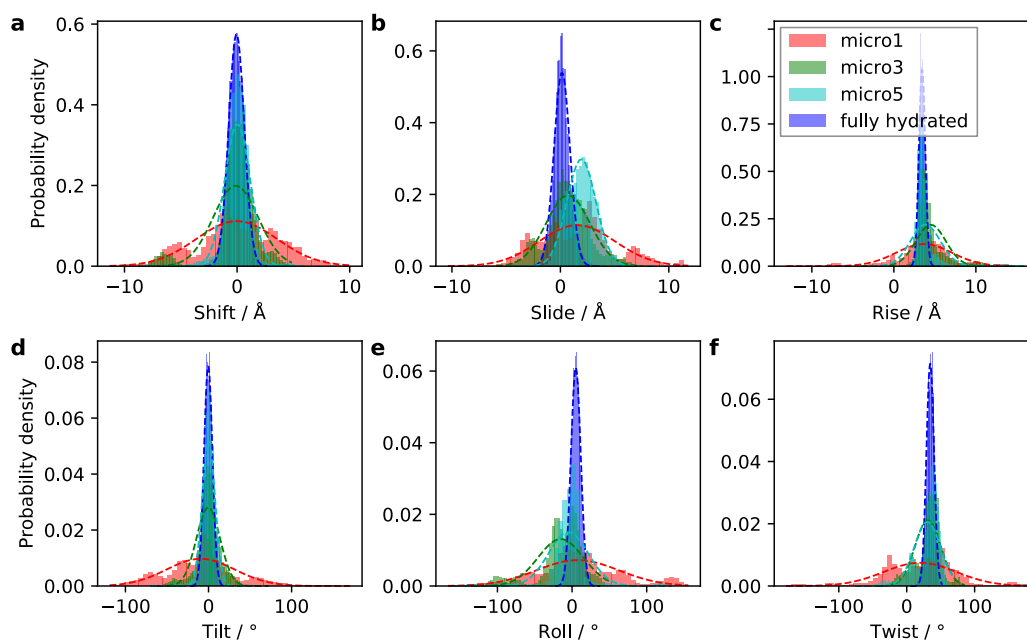


Figure 5.2: Helical parameters for a single DS in a fully hydrated and two microhydrated systems. The values are gathered from MD simulation snapshots via the CURVES+[141] software. The occurring helical parameters for a single dsDNA molecule are shown. The molecule is 51 bp long, from which the first and last five base pairs were excluded from the analysis. The dashed lines show corresponding Gaussian fits.

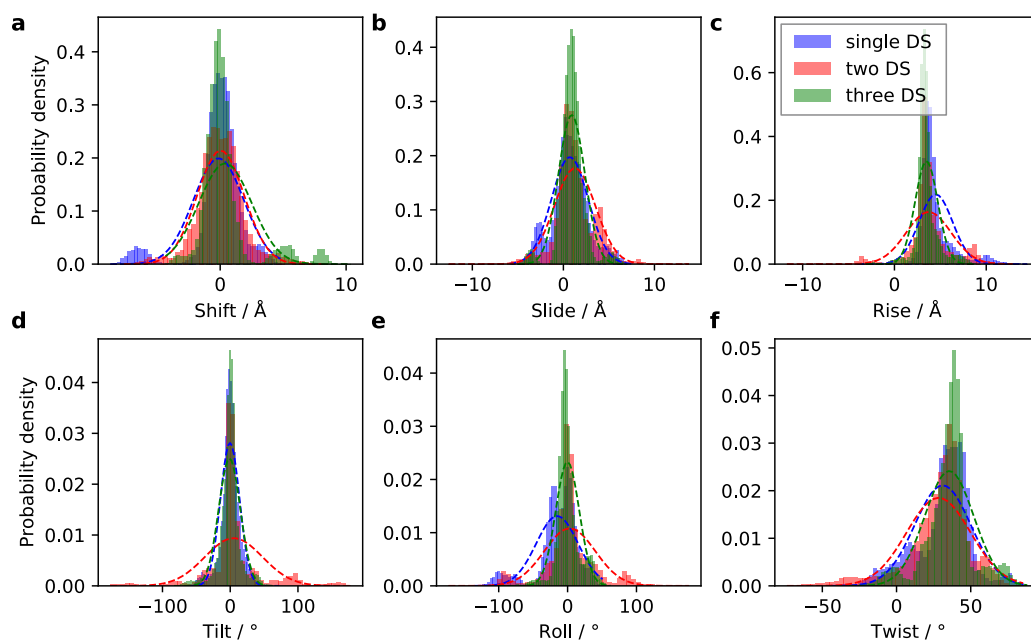


Figure 5.3: Helical parameters of a single DS and bundles of two and three molecules. The values are gathered from MD simulation snapshots via the CURVES+[141] software. The occurring helical parameters for a single dsDNA molecule and the two and three helices setups are shown. In the last case, only the parameters for the center molecule are shown. All three systems are in the 'micro3' hydration state. The molecules are 51 bp long, from which the first and last five base pairs were excluded from the analysis. The dashed lines show corresponding Gaussian fits.

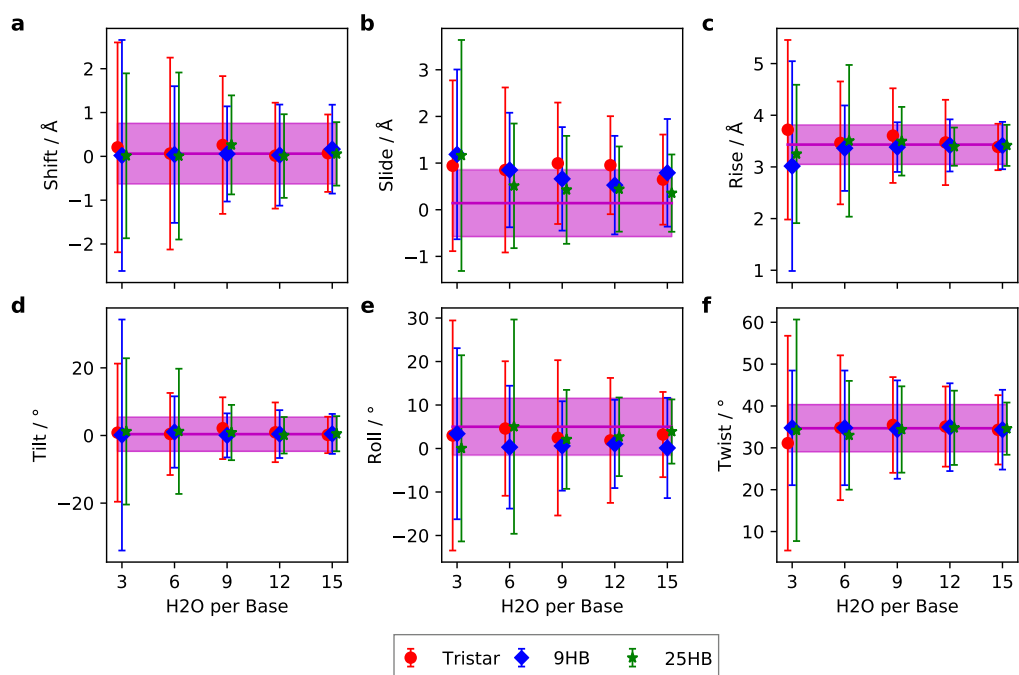


Figure 5.4: Helical parameters for multilayered setups at various hydration grades. The values are gathered from MD simulation snapshots via the CURVES+[141] software. The helical parameters for the 25HB, 9HB and Tristar setup are shown. The symbols show the average values and the bars the standard deviations. The magenta lines depict the average values of the parameters for a fully solvated system and the magenta areas illustrate the respective standard deviations.

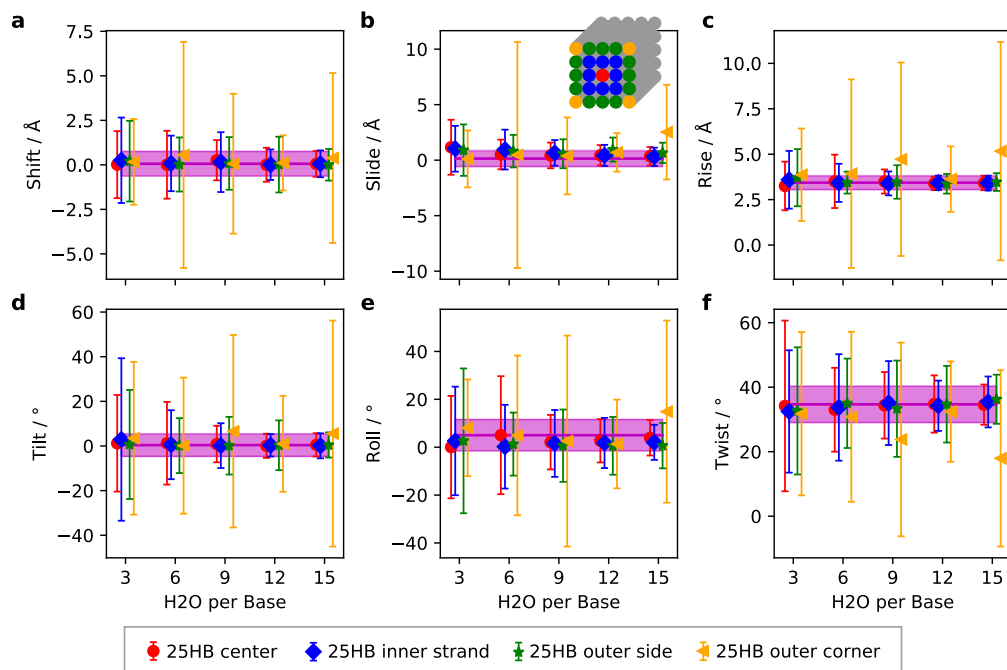


Figure 5.5: Helical parameters for different strands in the 25HB setup at various hydration grades. The values are gathered from MD simulation snapshots via the CURVES+[141] software. The helical parameters for strands at different positions of the 25HB setup are shown. The inlay graphic in the upper center shows the position of the respective strands. The symbols show the average values and the bars represent the standard deviation of the respective parameter. The magenta lines represent the average values of the parameters for a fully solvated system and the magenta areas depict the respective standard deviations.

the outside act as a protective layer for the inner strands. However, the discrepancy between the outer strands on the sides and the inner strands is only small. The corner strands on the other hand, show a high degree of disorder. This result indicates that most strands of such a bundle can contribute to the charge transport. As mentioned before, this is only valid for a sufficient level of hydration.

Another interesting point was that long sequences of AT bases were observed to be less stable. The simulated DNA molecule contained a 9 bp AT chain. Figure 5.6 shows a) the single dsDNA and b) the center molecule of the 25HB. The snapshots are taken from simulations of the micro1 hydration level at 15 ns. In both cases, base stacking is significantly reduced at the AT sequence. In a) the DNA is even unwinding.

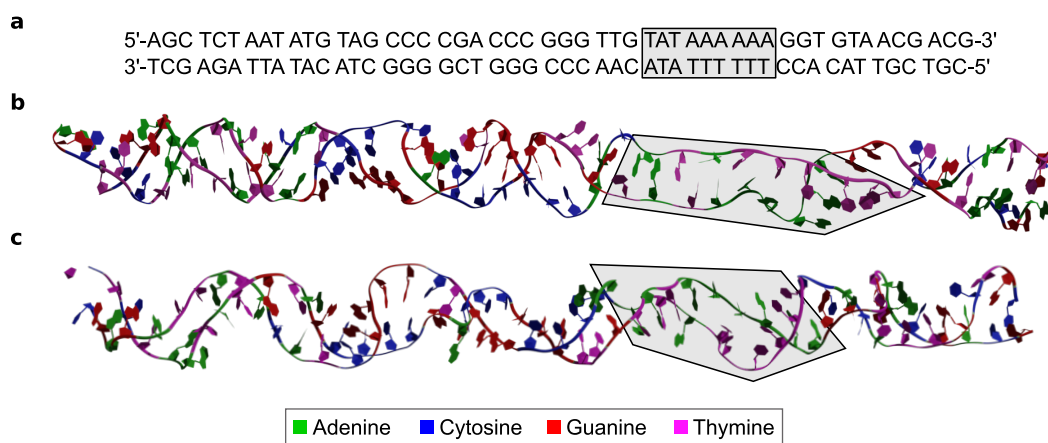


Figure 5.6: Snapshots of microhydrated DNA strands. The sequence of the simulated DNA strands is shown in **a**. Both snapshots were taken at the 15 ns mark of the simulation. The snapshot in **b** was taken from the single DS and the snapshot in **c** from the center molecule of the 25HB. Both are in the micro1 hydration state. Water molecules and ions are not shown. In image **c** the surrounding DNA strands are also not shown.

5.3 Conclusions

It was shown that microhydration does have a major effect on DNA base stacking. Single DNA strands showed a significant reduction in stability with decreasing hydration levels. The same phenomenon was present for small bundles of DNA strands. Even at high hydration levels, a reduced stability can be observed. Only the tightly packed, multilayered 25HB and 9HB systems did retain the stable helix and only at high hydration levels over 80% RH. Experimental data in the literature suggest that this effect is stronger for even bigger bundles[46]. In this case, the DNA might retain its stability even at lower hydration levels.

The results also indicate that high GC contents promote the retaining of the regular helical geometry. This is also in line with experimental findings[142, 143, 144]. High GC contents are well known to be advantageous for charge transport. This is, however, believed to be a result of the lower ionization potential of guanine.

From these findings it can be concluded that multilayered, tightly packed DNA molecules should be best suited for conductivity measurements in dry conditions. However, high humidity levels, or further improvement of the structures are required to fully retain their regular π -stacked form.

DNA Origami Structure Experiments

In this chapter the experimental studies and findings for sample preparation with DNA origami structures will be explained.

Experiments were carried out with two different DNA origami structures: a so called 12-helix bundle and a 30-helix bundle. Both have simple, rod like shapes with 12 and 30 parallel DNA strands, respectively. The 12HB was designed in a honeycomb lattice and the 30HB in a square lattice. Drawings, as well as atomic force microscopy (AFM) and transmission electron microscopy (TEM) pictures of the structures, are shown in figure 6.1.

Based on previous published experiments[10, 13, 107, 145, 42, 45, 41], two major factors for DNA charge transport were identified. First the linkage of the DNA to the electrode plays a major role. This was discussed in subsection 2.2.4.

The ends of the structures have functionalized groups for attachment to the gold electrodes. Experiments were carried out with thiol and polyA functionalization.

The 12HB Thiol sample employs hexanethiol linkage groups. The DNA origami structures possess six thiol groups on each side. Here, the sulfur atom is attached to a chain of six carbon atoms. This chain is in turn connected to the phosphorous group of the DNA backbone.

Consecutive single stranded adenine chains (polyA chains) have been shown to adsorb on gold surfaces with high affinity[64, 65, 66]. As described in section 2.2.4 the

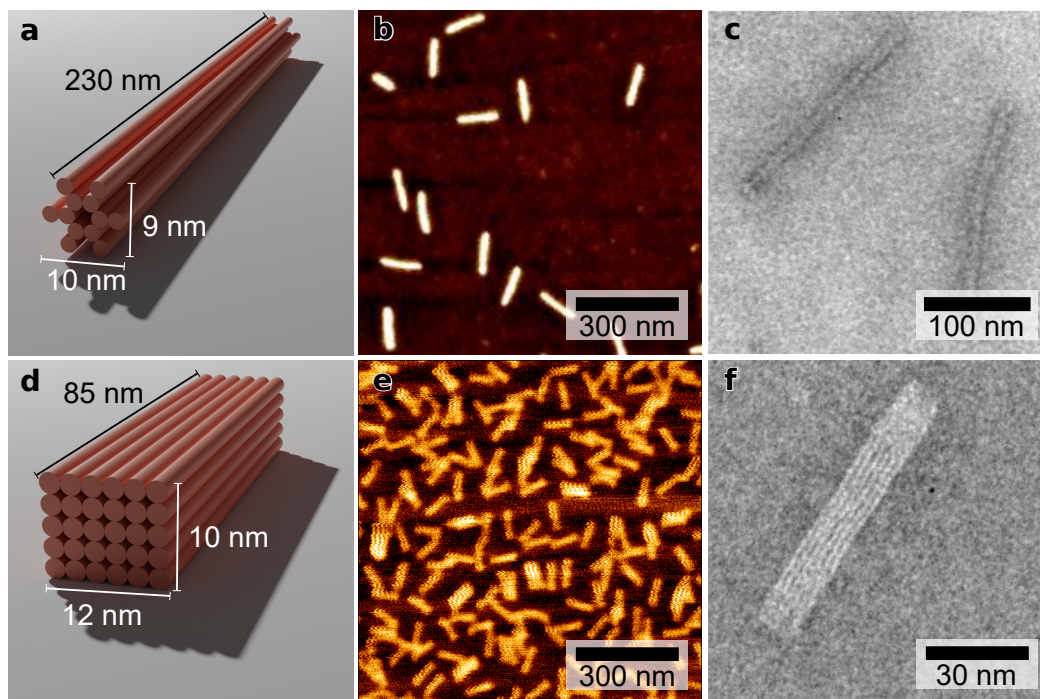


Figure 6.1: 12HB and 30HB DNA origami structures. Images **a** and **d** show drawings of the two DNA origami structures. AFM and TEM images of immobilized DNA origami structures are shown in **b** and **e**, and **c** and **f**, respectively.

6.1. DNA Origami Structure Trapping

Sample	Functionalization
12HB Thiol	5' Thiol-C6-SH, 3' Thiol-C3-SH
12HB PolyA	6A, 10A, 14A
30HB	Thiol-C6-SH
30HB PLL	Thiol-C6-SH & PLL coating

Table 6.1: DNA origami structure samples with functionalizations

polyA groups link the electrodes to the nucleoside's π -orbital, potentially enabling higher charge transport rates.

Second the environmental conditions need to be considered. Salt concentration, hydration level and interaction with the substrate surface can alter the helical structure of the DNA. All of these items have been further discussed in section 2.2. The compact structure of parallel helices in the 12HB and 30HB provides a stabilizing effect. This was explored for low hydration levels in chapter 5.

Additionally, 30HB structures were equipped with a poly-L-lysine coating. The PLL layer has been shown to preserve the DNA origami structure in low salt concentration and provides protection against nuclease degradation[146]. A similar protective effect of the layer can be expected from microhydration and DNA surface interaction.

6.1 DNA Origami Structure Trapping

Trapping of DNA origami structures between conducting nanostructures was achieved by the DEP method as described in section 3.2. During the experiments, the buffer solution was identified as a key factor for the success of trapping. For the storage of DNA origami structures, buffer solutions of high ionic strength are commonly used. These are, however, inadequate for DEP trapping. This is most likely due to AC electro-osmosis and electrothermal fluid flow acting against the DEP forces (see section 2.3.2 and 2.3.3).

Buffers with low ionic strength, on the other hand, can lead to denaturation of the DNA structures[147, 148, 146]. However, this effect varies with the exact structure. For buffer exchange, spin filtering was used, which does not affect DNA origami structures [149]. As shown in figure 6.2, the solution does not alter the geometry or concentration of the DNA origami structures even in a buffer with just 1.2 μM MgCl_2 concentration. Similar results were reported by V. Linko et al in 2015 [150]. Experiments were also carried out with DNA origami structures coated with a PLL

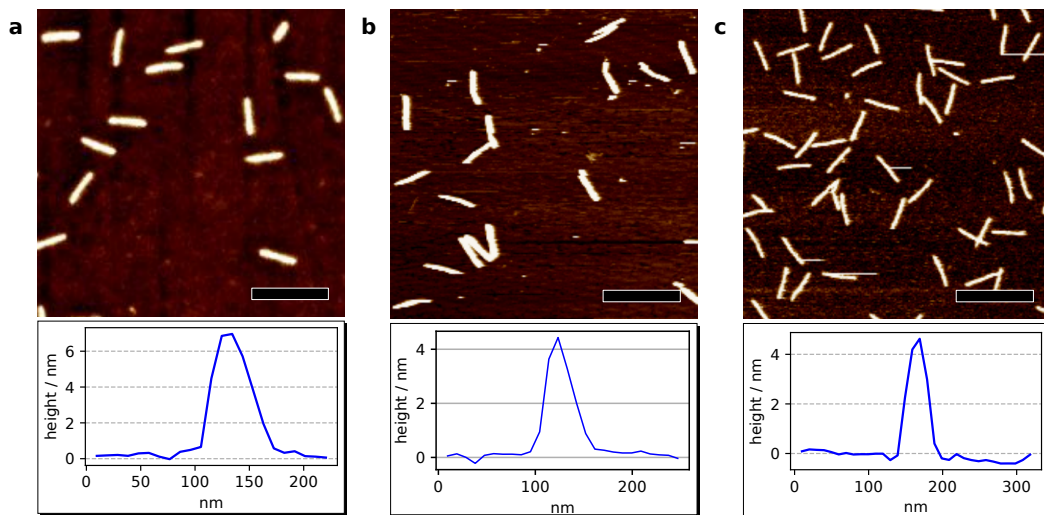


Figure 6.2: 12HB DNA origami structures stored at different levels of salt concentration. AFM images of immobilized 12HB structures on mica surface. Previous to immobilization the 12HB's were kept in a **a** 12.5 mM **b** 0.6 mM and **c** 1.2 μ M MgCl₂ solution. The scale bars are 500 nm and height scales 4 nm.

layer. There is evidence that the coating prevents DNA origami structure degradation in the presence of low salt concentrations[146]. Nevertheless, an influence on the helical structure of the individual DNA strands cannot be excluded.

The goal of the trapping is the production of uniform DNA samples. Ideally, only one DNA origami structure should be trapped in between the electrodes. This requires a sample solution of low concentration. At higher concentrations, overcrowding of the gap region with DNA origami structures occurs. Too low concentrations, on the other hand, drastically reduce the rate of successful trapping. Therefore, a good balance has to be found.

6.1.1 DNA-Gold linkers

Trapping was performed with 12HB DNA origami structures. In the literature, the contact between DNA and the electrode was identified as a potential bottleneck for charge transport[13]. Experiments with two different linkage groups, as listed in table 6.1, were performed.

All structures were successfully trapped between gold nanoelectrodes. The trapping fractions are listed in table 6.2.

6.1. DNA Origami Structure Trapping

	Voltage	Frequency	Dilution	Duration	Trapping	Destruction
12HB PolyA	1 V _{rms}	12.5 MHz	5 nM	5 min	54%	0%
12HB Thiol	1 V _{rms}	12.5 MHz	5 nM	5 min	43.2%	11.4%

Table 6.2: 12HB trapping fractions. For the calculation of the concentration, it is assumed that no losses occur during the buffer exchange.

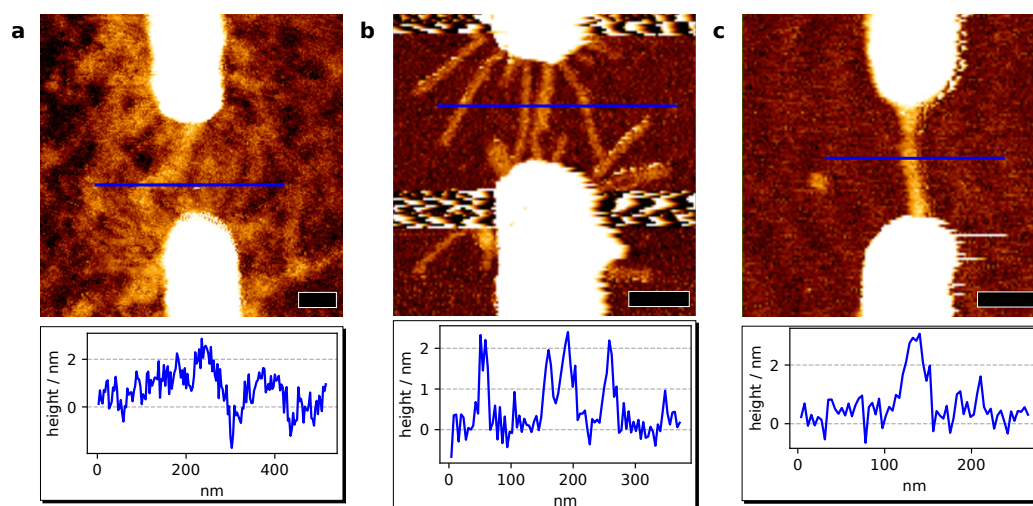


Figure 6.3: DEP-captured 12HB DNA origami structures. The AFM topographical scans show 12HB structures captured between two nanoelectrodes. The concentrations of the DNA origami structure solution were **a** 50 nM, **b** 10 nM and **c** 1 nM. In figures **a** and **b** the 12HB's have thiol- and in **c** polyA-linkers. The graphs in the inboxes show the height profiles along the blue lines. The black bars are scale bars whose length corresponds to 100 nm. All measurements were done in dry conditions. For the calculation of the concentration, it is assumed that no losses occur during the buffer exchange.

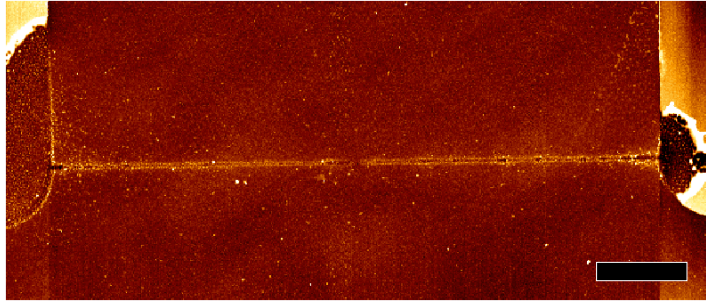


Figure 6.4: AFM topographical scan of a destroyed electrode pair after DEP preparation. The scale bar is $2 \mu\text{m}$ and the height scale 12.5 nm . DEP trapping was performed with 1 V_{rms} and 12.5 MHz using thiolized 12HB structures. The chip has five parallel connected electrodes, two of which were still intact after DEP preparation.

In a few cases, the “fingertip” electrodes were destroyed. Such an electrode is shown in figure 6.4. As can be seen, the “fingertip” part is almost completely erased. This hints to a high current throughput. Due to their smaller geometry and consequently, higher resistance, the electrodes have a high power dissipation. The resulting temperature rise leads to the destruction of the electrode. A similar phenomenon was regularly observed earlier, when chips were not protected from electrostatic discharge (ESD). Therefore, while handling the chips, the contacts of the sample holder were short wired and grounded. The person handling the chips is grounded as well to prevent ESD. As is the case with the electrode in figure 6.4, parallel electrodes were often observed to be left intact. A high current, due to the trapping of a low-resistant object might therefore be an alternative explanation. Shen et al. [10], observed similar phenomena. This will be discussed further below.

The impedance spectrum of a chip with a captured 12HB thiol structures is shown in figure 6.5. In both cases the measured impedance was not that of an ohmic resistor.

6.1.2 DNA Origami Structure with Protective Coating

Figure 6.6 shows AFM images of trapped 30HB structures for three DNA origami structure solution concentrations. By systematic investigations for various DNA origami structure solution concentrations, an optimum value for single DNA origami structure trapping was found at 1 nM , for both 30HB structure types.

Trapping fractions of both the uncoated 30HB and 30HB PLL samples are shown in table 6.3. The fractions for the thiolized, uncoated 30HB DNA origami structures

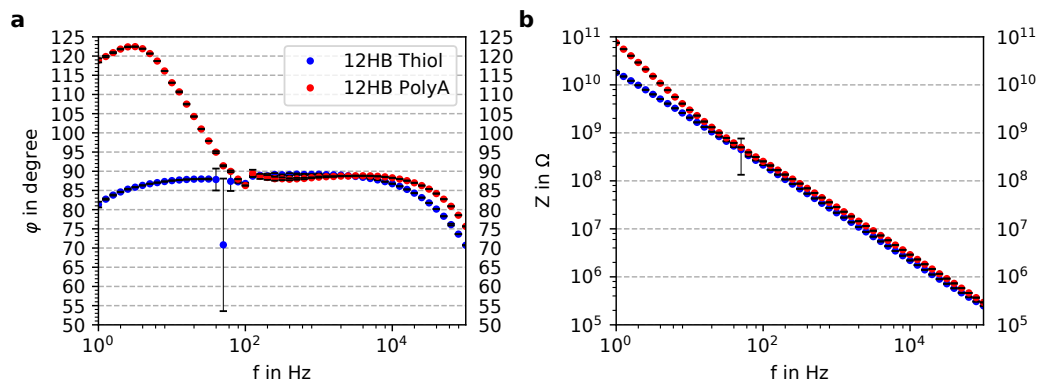


Figure 6.5: Impedance spectra of 12HB DNA origami structures with different linkage groups. Figure **a** shows the phase and **b** the impedance values over the frequency. The blue and red lines represent chips with a captured 12HB Thiol and a captured 12HB PolyA structures respectively. Uncertainty bars represent the 95% CI.

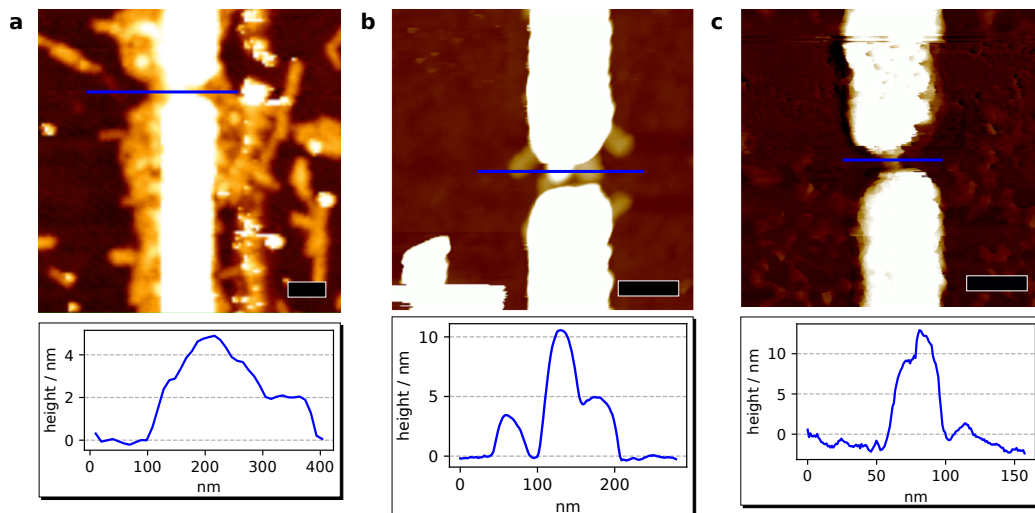


Figure 6.6: DEP captured 30HB DNA origami structures. The AFM topographical scans show 30HB structures captured between two nanoelectrodes. The concentrations of the DNA origami structure solution were **a** 20 nM, **b** 5 nM and **c** 1 nM. In **a** uncoated 30HB were used. The structures in **b** and **c** have a PLL coating. The inlays show the cross sections along the blue lines. The scale bars are 100 nm. All measurements were done in dry conditions. For the calculation of the concentration, it is assumed that no losses occur during the buffer exchange.

DNA Origami Structure Experiments

	Voltage	Frequency	Dilution	Duration	Trapping	Destruction
30HB	1 V _{rms}	12.5 MHz	1 nM	3 min	43,75%	12,5%
30HB PLL	1 V _{rms}	12.5 MHz	1 nM	3 min	16,67%	54,16%

Table 6.3: 30HB Trapping fractions. For the calculation of the concentration, it is assumed that no losses occur during the buffer exchange.

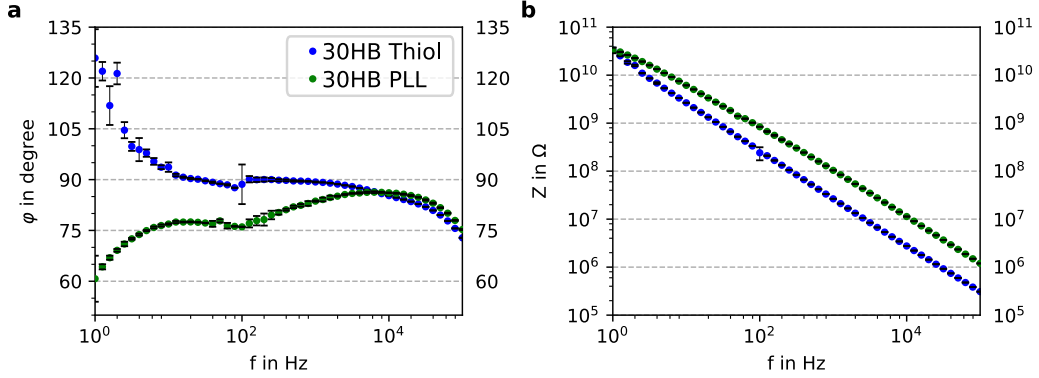


Figure 6.7: Impedance spectra of 30HB origami structure with and without PLL coating. Figure **a** shows the phase and **b** the impedance values against the frequency. The blue and red lines represent chips with a captured 30HB and a captured 30HB PLL structure respectively. Error bars represent the 95% CI.

are nearly identical to those of the thiolized 12HB structures (see table 6.2). The PLL coated samples, on the other hand, had much higher fractions of destroyed electrodes.

The spectra of a captured 30HB and a 30HB PLL DNA origami structures are shown in figure 6.7. Both samples show non-ohmic behavior.

6.1.3 DEP with a series resistor

So far, none of the captured DNA origami structure showed signs of ohmic conductivity in their impedance spectra. The destroyed electrodes during the DEP trapping are, however, results of high electrical currents. To restrict high currents, a series resistor R_s was used, as shown in figure 6.8. The voltage drop at the gap can be compensated by increasing U_0 . The maximum output voltage of the signal generator is 20 V_{pp}. This limits R_s to a maximum of 39 k Ω for trapping at 12.5 MHz. At higher resistance values U_{gap} would be too low for DEP trapping.

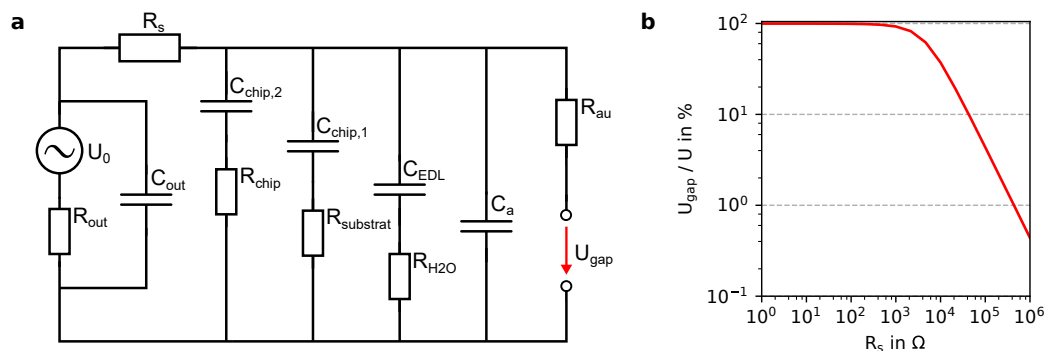


Figure 6.8: Circuit and gap voltage for a series resistor. The circuit in image **a** is comprised of the equivalent circuits for a chip with a water droplet and the included series resistor R_s . The resulting voltage at the gap U_{gap} is depicted in image **b**. The values were calculated using LTspice at 12.5 MHz.

DEP trapping was done using a series resistor of 39 k Ω , $U_0 = 20 V_{\text{pp}}$ at 12.5 MHz with the 30HB and the 30HB PLL samples. Both DNA origami structures were used in a 1 nM concentration. Incubation time with the applied voltage was 10 min. In addition to the 'fingertip' electrodes, trapping was performed using wider 'arrowhead' shaped electrodes. These were designed for higher ampacity.

Trapping with the 'fingertip' electrodes gained similar results as without the series resistor. The destruction of the electrodes was, however, more localized, as seen in figure 6.9.

DEP trapping when using the 'arrowhead' electrodes did also yield cases of destroyed electrodes. This time, however, chips with successfully captured DNA origami structures were measured with ohmic conductivity. This was only the case for the PLL coated structures. Figure 6.12 shows two gaps with captured 30HB PLL DNA origami structures. The resistance of the electrode gaps with captured 30HB PLL DNA origami structures lies typically in the low M Ω range. Impedance spectra of several samples with 30HB PLL are shown in figure 6.10. Figure 6.11 shows the spectrum of a chip after preparation and 258 h later. Over that time, the ohmic resistance increased by 12.9 %.

In one instance a 150 M Ω resistance was measured. The corresponding electrode gap is shown in images 6.12 b and c. This gap was most likely destroyed by high currents. However, the remaining electrode gap was still close enough to produce sufficiently high electric fields for DEP trapping. The ohmic feature is therefore

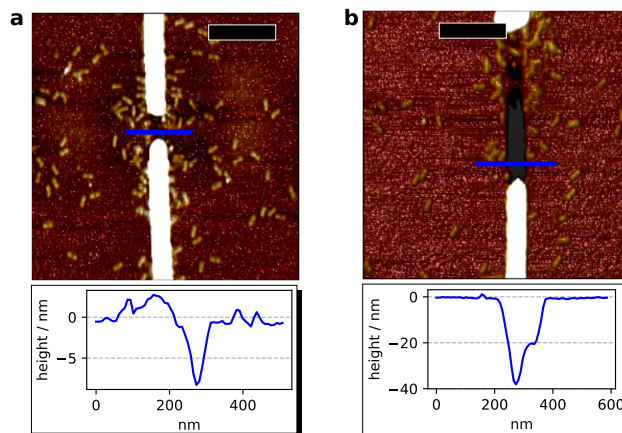


Figure 6.9: Localized destruction of 'fingertip' electrodes. The AFM topographical scans show 'fingertip' nanoelectrodes after DEP trapping with 30HB PLL DNA origami structures. In image **b**, the gap was originally at the position of the blue line. The inlays show the cross sections along the blue lines. The scale bars are 500 nm. All measurements were done in dry conditions.

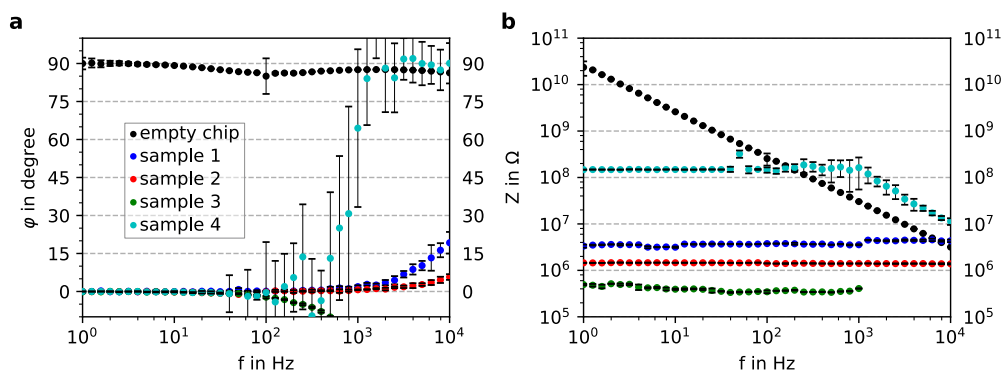


Figure 6.10: Impedance spectra of 30HB PLL DNA origami structures captured with a series resistor. Figure **a** shows the phase and **b** the impedance values against the frequency. The blue and red lines represent chips with a captured 30HB and a captured 30HB PLL structures respectively. Uncertainty bars represent the 95% CI.

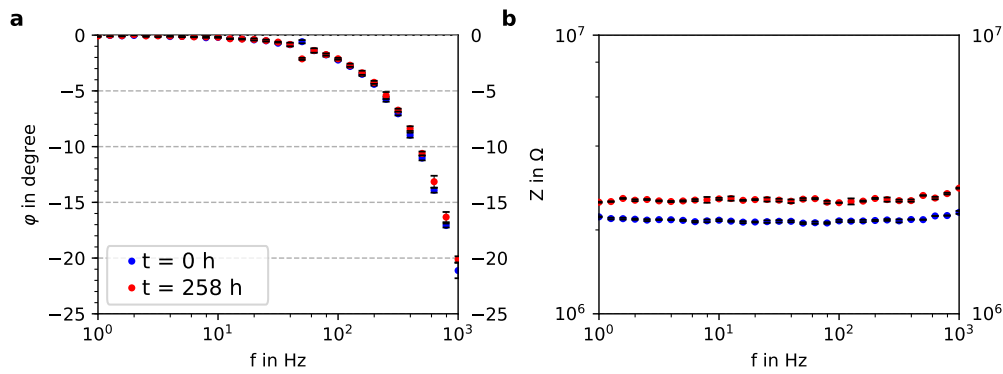


Figure 6.11: Impedance spectra of a 30HB PLL DNA origami structure. Figure **a** shows the phase and **b** the impedance values against the frequency. The spectrum in blue was measured shortly after preparation and the spectrum in red was measured after a period of 258 h. During that time the sample was kept at room temperature in dry air. The uncertainty bars represent the 95% CI.

most likely a result of a chain of linked DNA origami structures.

6.1.4 DNA overlapping with Gold Nanostructures

A more intricate way to connect DNA and gold-electrodes is to first immobilize DNA origami structures on a surface, followed by the fabrication of electrodes on top of the DNA origami structure. DEP trapping process requires the application of a voltage to attract the DNA origami structures which often results in the destruction of the electrodes. In contrast, the subsequent electrode production process does not require voltage application and, therefore, no high currents can destroy the electrodes and DNA. Also, the direct overlapping of the gold electrode with the DNA strands can potentially result in an improved electrical contact.

A requirement for this method is the knowledge of the exact position of the targeted DNA molecules. For this purpose, a cross-lattice was fabricated on a silicon-oxide surface. The surface was then reduced by treatment in an oxygen plasma. This allows the immobilization of DNA similar to immobilization on a freshly cleaved mica substrate. The prepared surface was examined with AFM to find DNA origami structures on adequate positions. Subsequently, gold electrodes were produced on the previously identified positions. The electrode fabrication requires, among other steps, the coating and removal of the surface with photoresist. This appeared to be

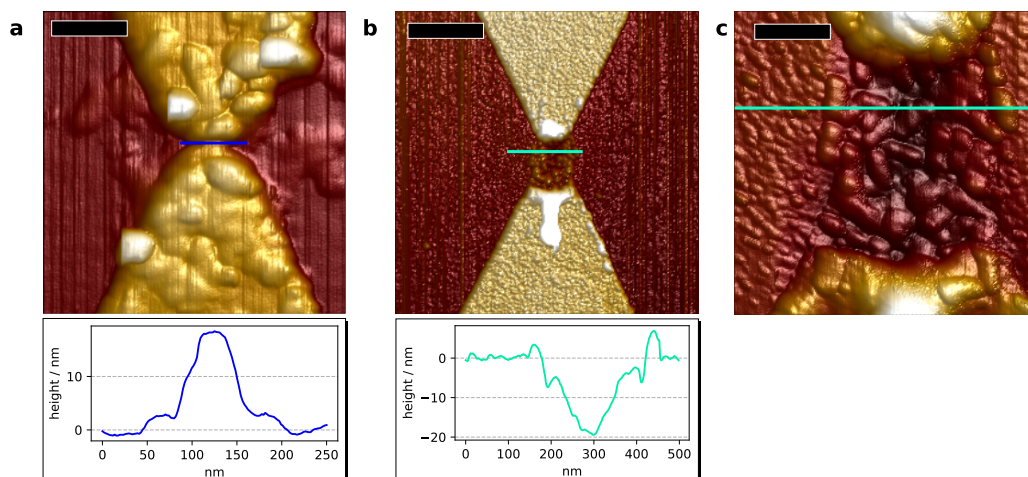


Figure 6.12: AFM topographical scans of captured 30HB PLL DNA origami structures. AFM height images of 'arrowhead' nanoelectrodes after DEP trapping with 30HB PLL structures. The inlay in image **a** shows the cross sections along the blue and that in **b** the cross section along the turquoise lines. The scale bars in images **a** and **c** correspond to 500 nm and the scale bar in image **b** corresponds to 2 μm . All measurements were done in dry conditions.

too invasive on the samples. After electrode fabrication, no traces of DNA were found on the surface. Therefore, this method proved to be inadequate for the production of suitable DNA samples.

6.2 Conclusions

DEP trapping was successful for all DNA origami structures. Depending on the DNA sample and trapping setup, major differences in the results were observed. The fractions for trapping without a series resistor are listed in the tables 6.2 and 6.3. Two observations were made that stand out. First the fractions of experiments where no trapping or destruction occurred was about 45 % for all DNA origami structures, except the 30HB PLL. The second observation concerns the fractions of destroyed electrodes. Both thiolated uncoated DNA origami structures had nearly identical destruction fractions. The coated 30HB showed a much higher fraction of destroyed electrodes. At the same time, no destruction was observed for the polyA functionalized DNA origami structures as well as in control experiments with water containing no DNA.

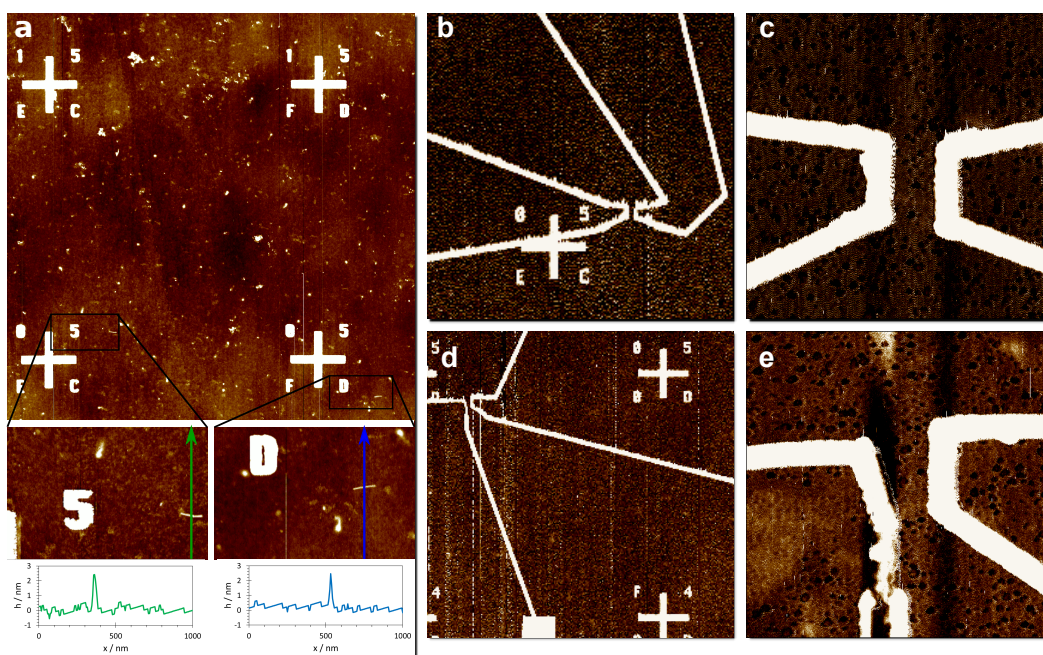


Figure 6.13: AFM topographical scans of immobilized DNA origami structures with subsequent electrode production. Figure a shows a silicon surface with a cross grid and surface immobilized 12HB structures. The images below show closeups with cross sections across the DNA origami structures. In a subsequent production step, electrodes were produced at the positions of these structures. One electrode is shown in images b and c and the other in d and e.

This indicates that the high currents leading to the destruction of the DNA origami structures are produced by conducting DNA origami structures being captured during DEP trapping. Cases where trapping occurred without destruction are probably due to poorly contacted DNA origami structures, or ones with altered structures. Therefore, the sum of the trapping fraction and the destruction fraction should be equal for all DNA origami structures. The DNA origami structure concentration was not measured but calculated assuming that no losses occurred during the buffer exchange. The more resilient structure of the 30HB_PLL structures might lead to fewer losses during buffer exchange. The resulting higher concentration would then explain the higher fractions.

All DEP sample preparations were performed in solutions of very low salt concentration. The structures of the PLL coated DNA origami structures should be least altered by the low salinity. Therefore, there would be more DNA origami structures which support high charge transport rates. This can explain the high destruction fraction for these DNA origami structures. The 12HB polyA samples did not show this phenomenon. It can therefore be concluded that the polyA functionalization is not a suitable electrical contact. The equal fractions of the thiolized, uncoated 12HB and 30HB samples are also in line with this interpretation. MD simulations (see chapter 5), however, indicate that, in a dry environment, 30HB structures are more stable than the 12HB structures.

A series resistor was used to limit high currents that lead to the destruction of the electrodes during DEP trapping. While trapping still yielded destroyed electrodes, a different picture of electrode destruction was observed. The destruction was more confined to the gap region in experiments where a current limiting resistor was used. Shen et al. [10] observed very similar results in 2015. Without a series resistor, their experiments however, yielded samples of ohmic resistances of several 10 G Ω . This was for DNA origami structures with and without thiol linkers. The key difference here is most likely that the measurements of Shen et al. took place in high relative humidity conditions (RH \sim 90 %). In these environments, 30HB are expected to have a similar stability as DNA in a liquid environment. This was shown in chapter 5.

Trapping of samples with good ohmic conductivity was eventually achieved for the 30HB PLL structures. A current limiting resistor and electrodes of higher ampacity were also essential for this achievement. The measured resistances were in the order of 500 k Ω to several M Ω . Electrode destruction did, however, still occur. This indicates that samples with even higher conductivity are possible. Preparation of

these samples would require higher current limitations during DEP trapping. Implementation of such a current limitation without voltage losses can be achieved in two ways. A series resistor can be manufactured directly before the electrodes on the micro-scale. In this case the resistor is an internal part of the sample. A second possibility would be the use of a different substrate material for the electrode chips. Glass-, or sapphire-substrates are insulating materials. The use of silicon substrates requires an insulating SiO_2 layer. This results in high capacities of the electrode chip. Avoiding these high capacities enables the usage of higher external series resistors during the DEP preparation. Afterwards, this resistor can simply be removed for conductivity measurements.

Conclusions & Outlook

In this work, the application of DNA as a radiosensitive detector material was investigated. The electrical conductivity of the DNA serves as an indicator for the amount of biological radiation damages.

Radiation experiments were performed with λ -DNA, suspended between metal electrodes. These samples were provided by the San Diego State University. The samples were irradiated with electrons and alpha particles. The former were produced by an electron gun and the latter were provided by either an ^{241}Am source or the microbeam facility of Physikaisch-Technische Bundesanstalt in Germany. The electron irradiation experiments did not yield consistent results. The main obstacle was the requirement of a vacuum for the operation of the electron gun. Unfortunately, the DNA was damaged every time when introduced into a vacuum. The damage was so severe that no ohmic resistance was measured afterwards. Further damages due to radiation were, therefore, not detectable.

Vacuum was not required for the alpha particle sources. Here the experiments were conducted in air at room temperature. In the measurement with alpha particles from an ^{241}Am source as well as the microbeam facility a decrease in conductivity over the course of the irradiation was measured. Irradiation with the ^{241}Am source was performed over 28 days. During this time, the sample resistance increased by a factor more than ten.

Microbeam irradiation was performed over 2.5 h, however, with a significantly higher particle fluence than in case of the ^{241}Am irradiation. Still, only a slight shift in phase was measured during microbeam irradiation. Potential causes of this discrepancy include the energy difference between the experiments and the amount of generated secondary particles.

The experiments showed that DNA is indeed sensitive to radiation. For the application as a detector material, a quantitative relation between the amount of DNA damage and the change in conductivity needs to be established. This requires samples with uniform initial impedance characteristics, which can allow an unambiguous comparison between irradiation experiments with varying dose and radiation quality.

The preparation of gold nanoelectrodes with single trapped DNA origami structures could be achieved. AC dielectrophoresis was used for trapping of the DNA molecules between the metal electrodes. Experiments with different geometries and functionalizations were conducted. Successful trapping was achieved for all DNA origami structure samples. Ohmic conductivity was, however, only registered for PLL covered 30HB's with thiolated ends.

Experiments reported in the literature already suggested the necessity of the thiol functionalization for charge transport. The present work investigated the use of polyA chains as a possible alternative. These showed a mechanical stability similar to thiolated DNA. However, the experimental results indicate, that the polyA chains do not support high charge transport rates.

It was known that microhydration in dry air reduces DNA conductivity. The tightly packed, multilayered structure of 30HB DNA origami structures are considered to make them more stable at low hydration levels. The resilience of multilayered DNA structures against microhydration was investigated in this work by performing MD simulations of parallel DNA strands in various conformations and hydration grades. It was found that tightly packed multilayered structures were indeed much more stable than individual or loosely packed strands. However, stable helical structures as in the case of fully hydrated states, were still only achieved for very high hydration levels.

To further increase the resilience of the DNA origami structures, they were covered with a layer of poly-L-lysine, which can stabilize DNA origami structures against buffers of low salt concentrations. With these structures, the production of samples with ohmic conductivity in dry conditions was achieved. The measured resistance values were in the range of several $\text{M}\Omega$.

A frequently observed phenomenon was the local destruction of the substrate material and electrodes after DEP trapping. The destruction was the result of high electrical currents and was observed for all thiolated structures. This indicates that the DNA origami structures can possess even higher values of electrical conductivity. Therefore, current limiting resistors must be introduced to the trapping setup. Since high frequency values are required for DEP trapping, the electrode chips need to be specially designed to have a low capacitance. Otherwise, the combination of capacity and series resistor would lead to voltage losses, which would impede DEP trapping. With such a setup, it should be possible to produce samples with optimal charge transport properties, i.e. low resistance values. This will be the subject of future experiments. The subsequent step would be to test the influence of different radiation qualities and doses on the conductivity of these samples.

Appendix

DNA Origami Structure Designs

This chapter contains the sequence maps of the two basic DNA origami structures used in this work. The maps were generated with the caDNAo software[103].

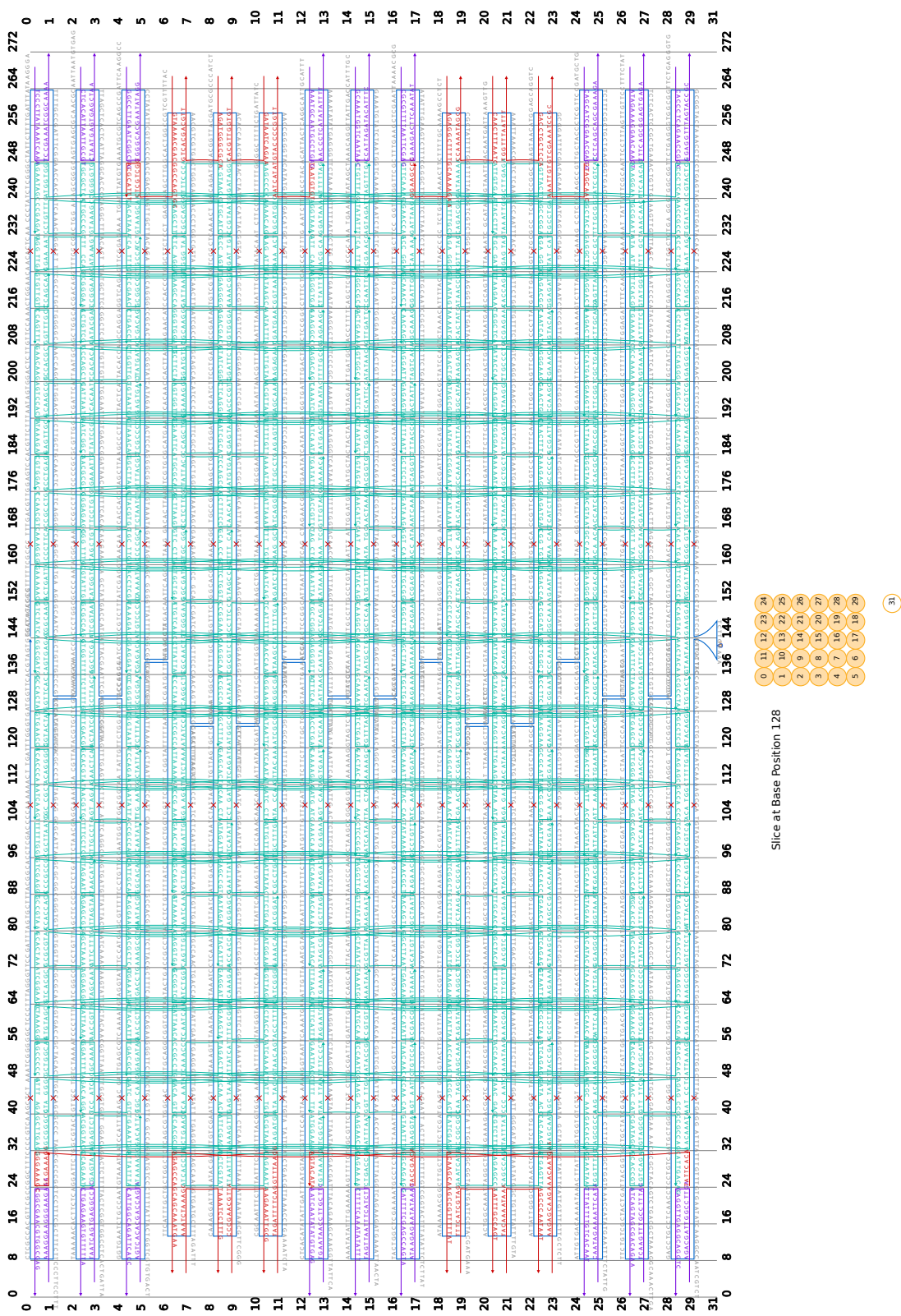


Figure A.1: caDNano design of the 30HB

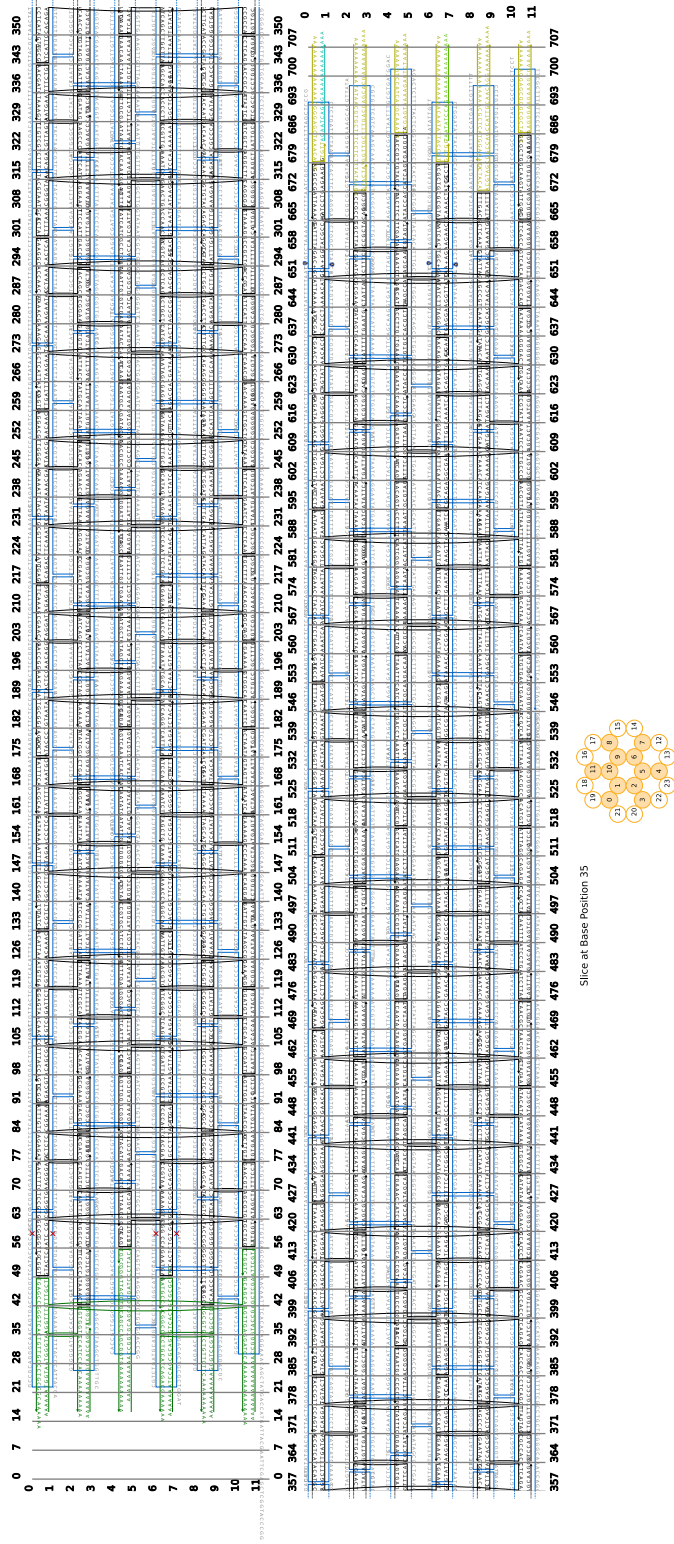


Figure A.2: caDNAno design of the 12HB origami

MD Simulation of microhydrated DNA Bundles

This chapter contains plots of the DNA helical parameters of the examined setups over the course of the MD simulations. The blue line represents the respective average value and the magenta bars the respective standard deviation. The strands were analyzed using the CURVES+[141] software package, with first and last 10 bps of the individual strands excluded from the analysis.

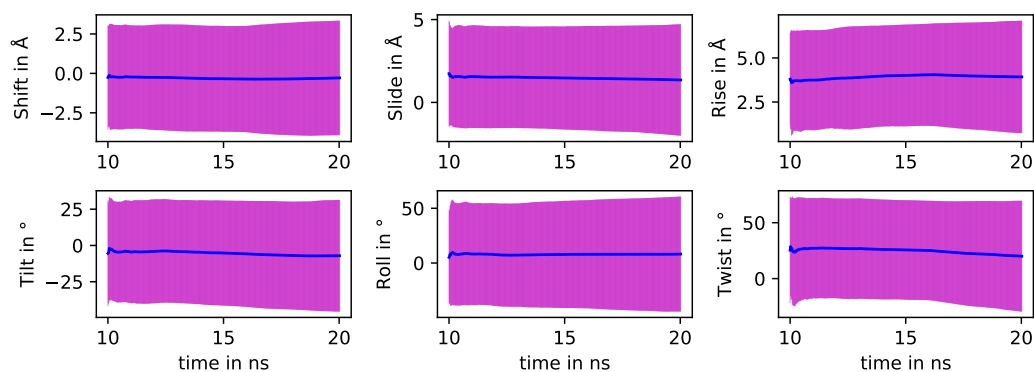


Figure B.1: Helical parameters of a microhydrated (micro1) DS

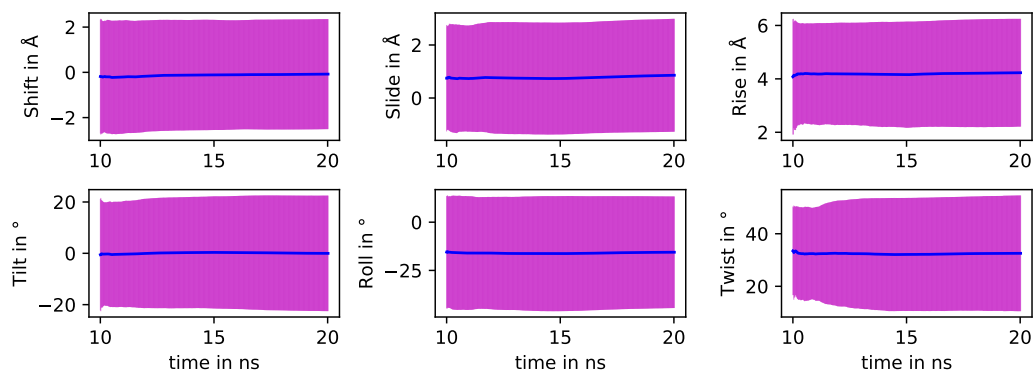


Figure B.2: Helical parameters of a microhydrated (micro2) DS

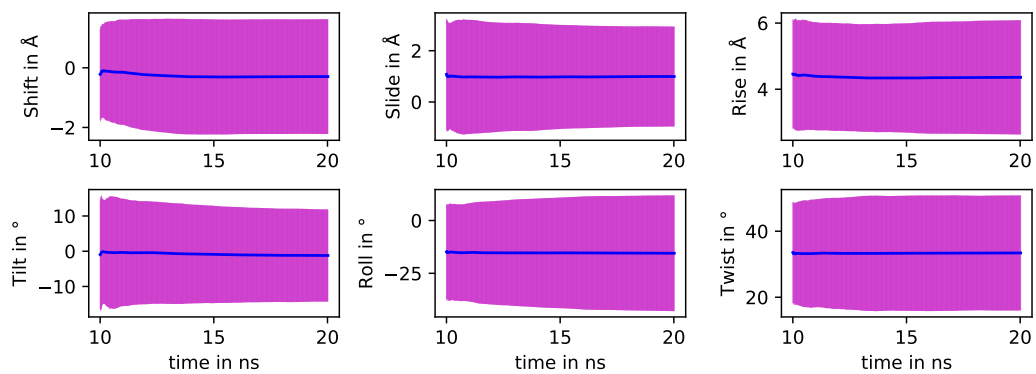


Figure B.3: Helical parameters of a microhydrated (micro3) DS

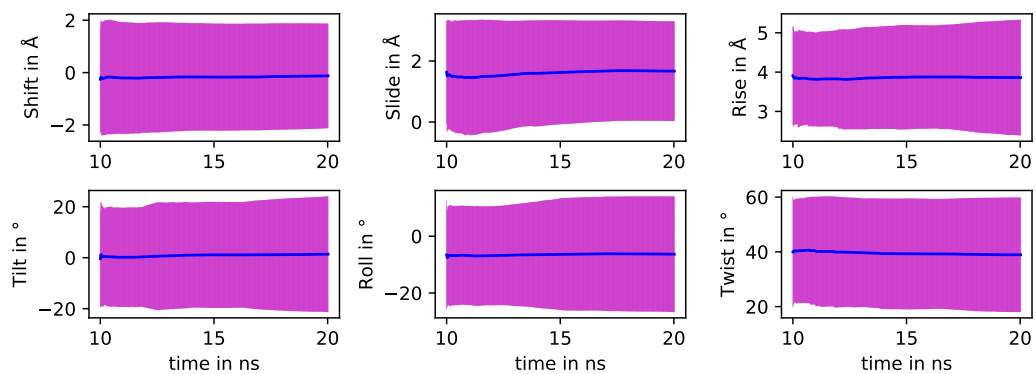


Figure B.4: Helical parameters of a microhydrated (micro4) DS

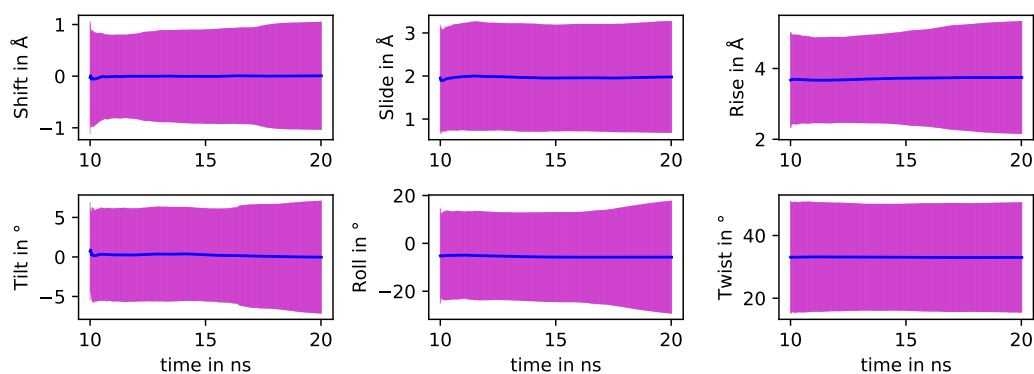


Figure B.5: Helical parameters of a microhydrated (micro5) DS

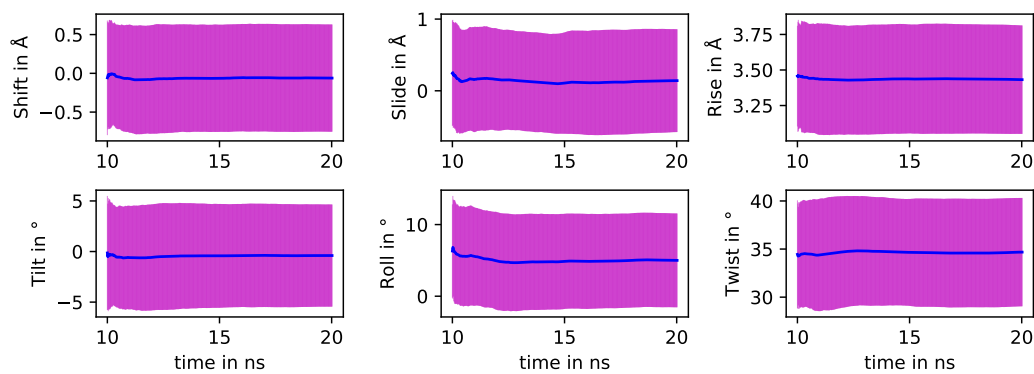


Figure B.6: Helical parameters of a fully solvated DS

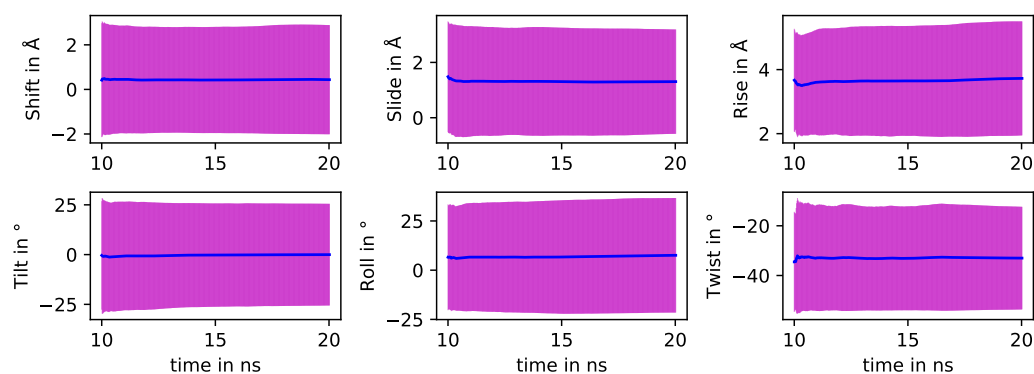


Figure B.7: Helical parameters of one of two parallel and microhydrated (micro2) DS

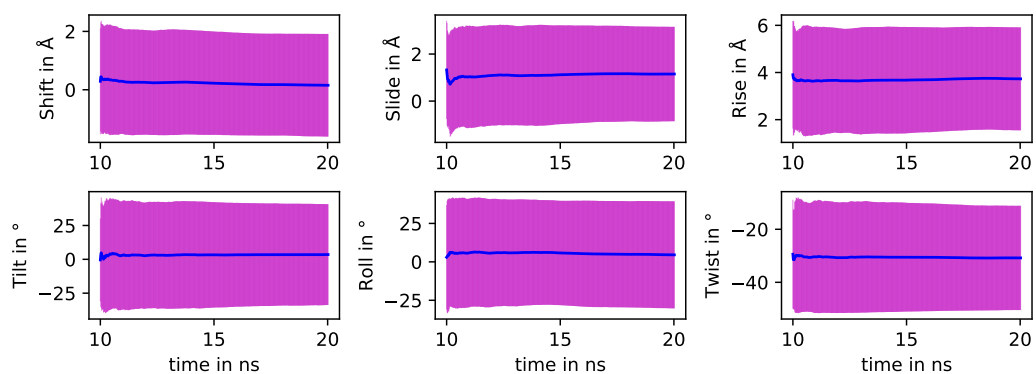


Figure B.8: Helical parameters of one of two parallel and microhydrated (micro3) DS

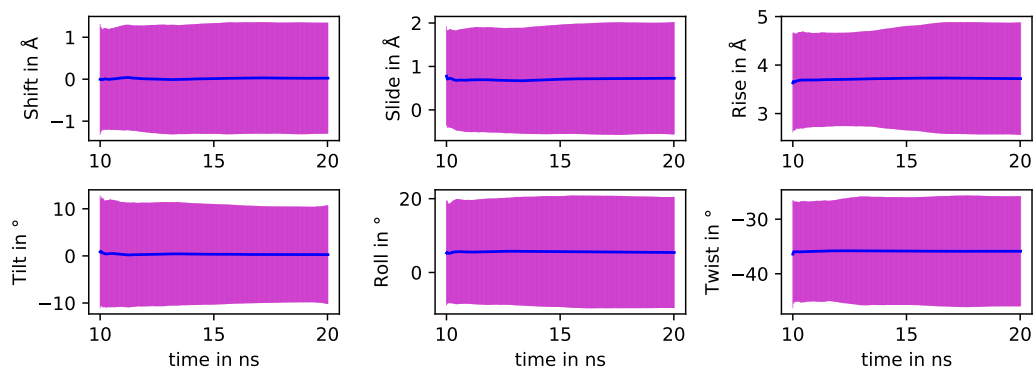


Figure B.9: Helical parameters of one of two parallel and microhydrated (micro4) DS

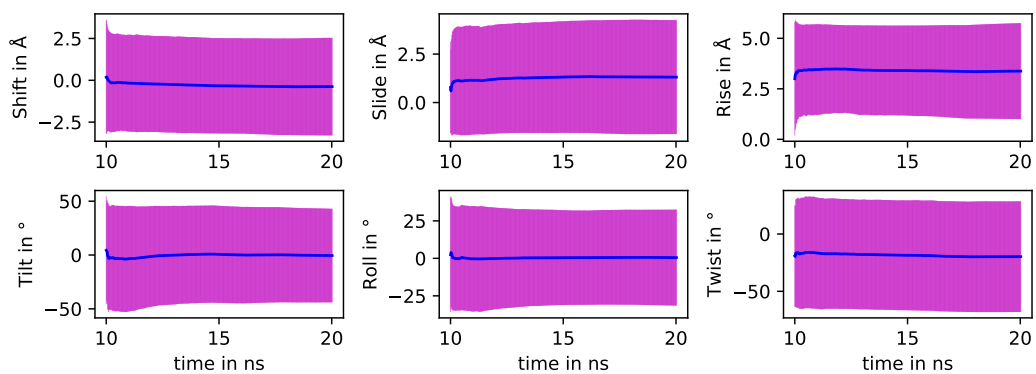


Figure B.10: Helical parameters of the center DS of three parallel and microhydrated (micro1) DS

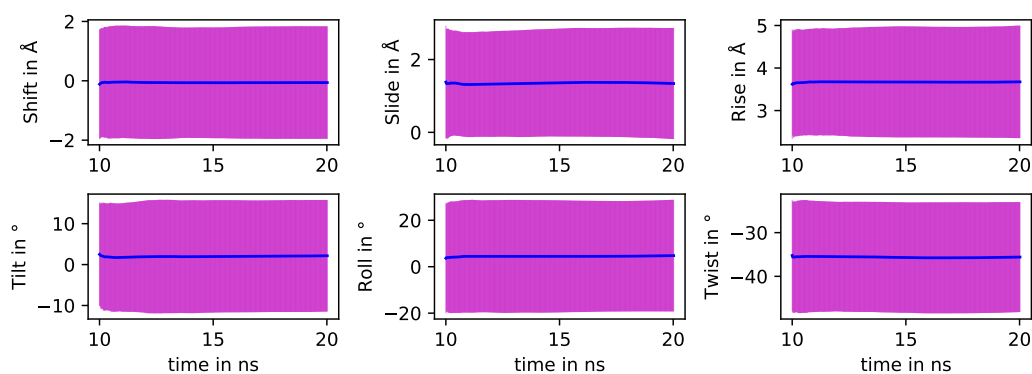


Figure B.11: Helical parameters of the center DS of three parallel and microhydrated (micro2) DS

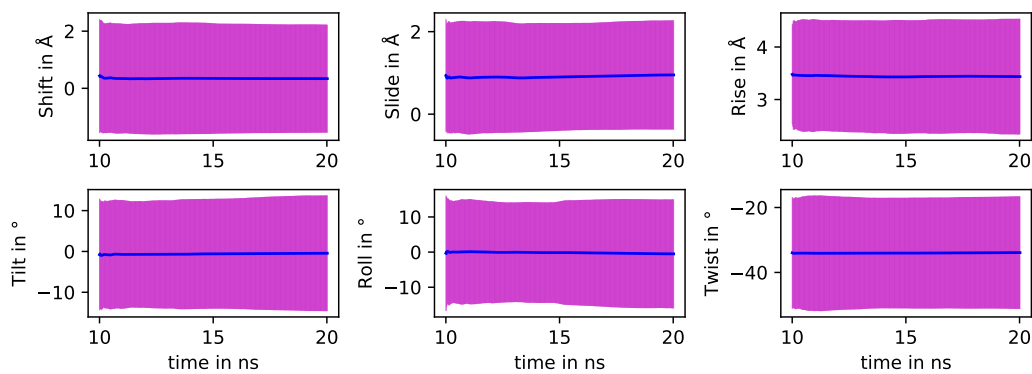


Figure B.12: Helical parameters of the center DS of three parallel and microhydrated (micro3) DS

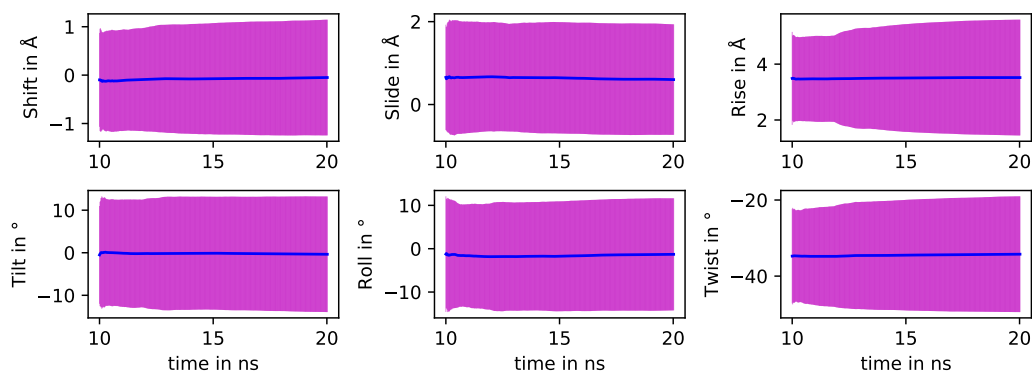


Figure B.13: Helical parameters of the center DS of three parallel and microhydrated (micro4) DS

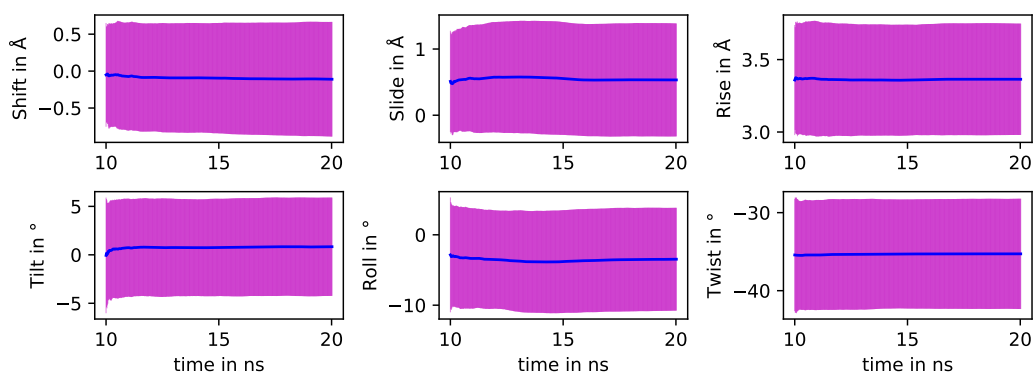


Figure B.14: Helical parameters of the center DS of three parallel and microhydrated (micro5) DS

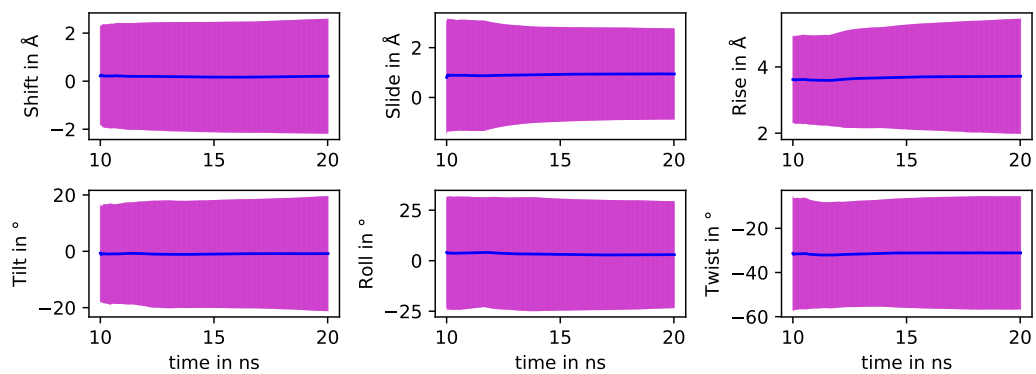


Figure B.15: Helical parameters of the center DS of a microhydrated (micro1) Tristar structure

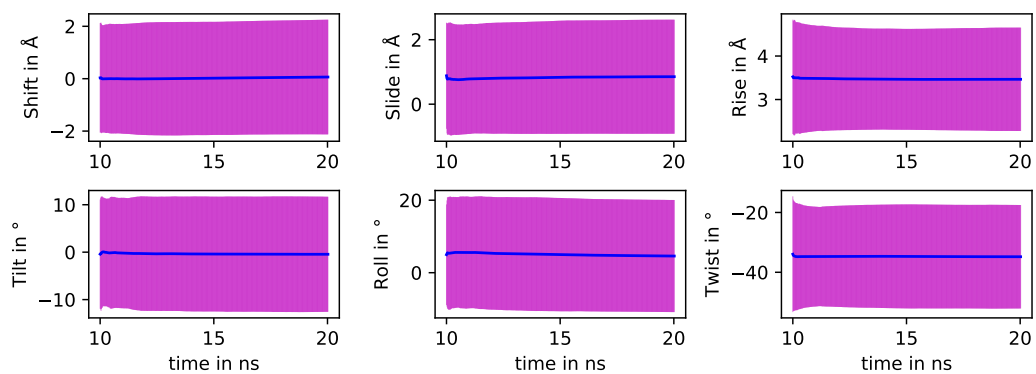


Figure B.16: Helical parameters of the center DS of a microhydrated (micro2) Tristar structure

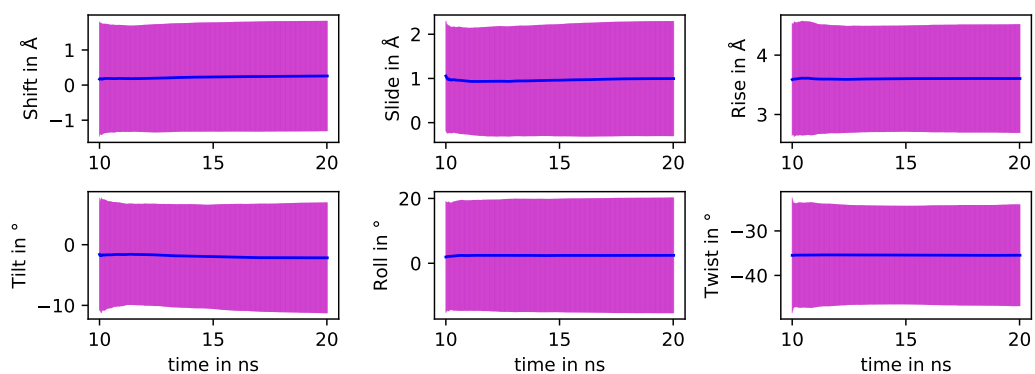


Figure B.17: Helical parameters of the center DS of a microhydrated (micro3) Tristar structure

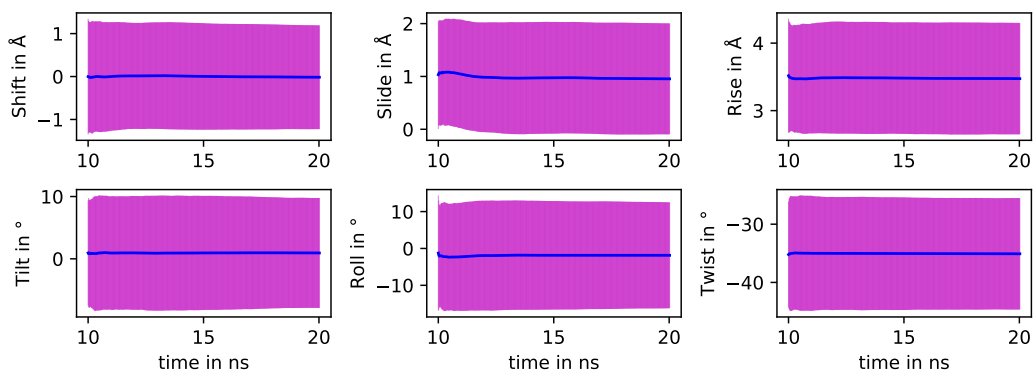


Figure B.18: Helical parameters of the center DS of a microhydrated (micro4) Tristar structure

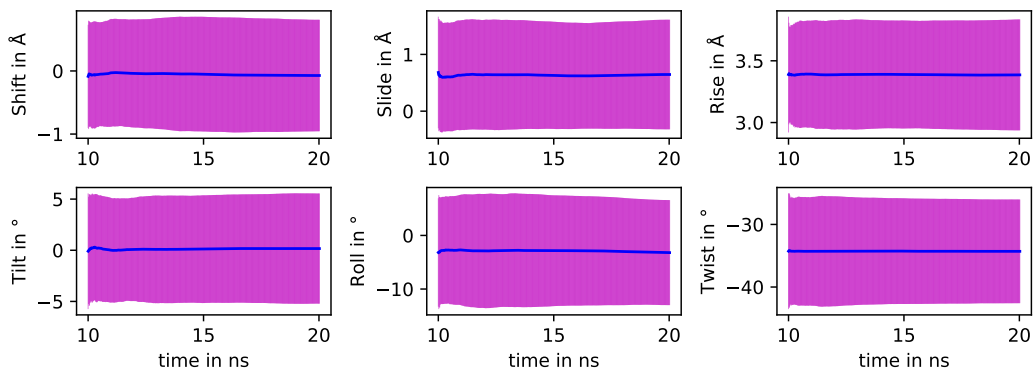


Figure B.19: Helical parameters of the center DS of a microhydrated (micro5) Tristar structure

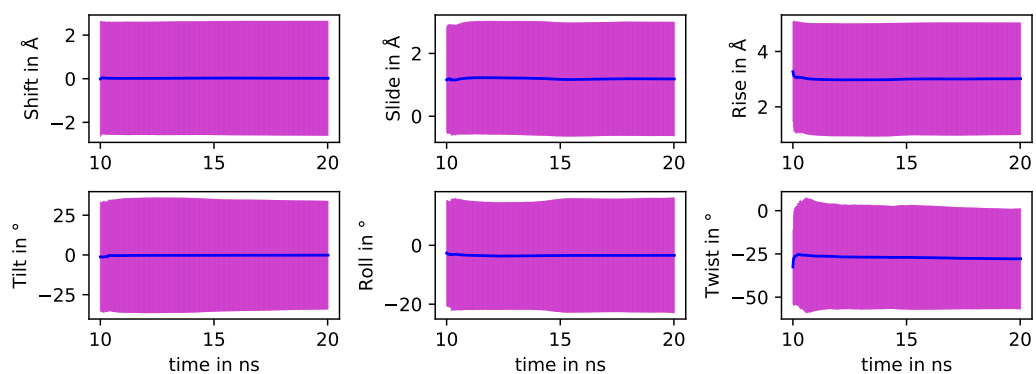


Figure B.20: Helical parameters of the center DS of a microhydrated (micro1) 9HB structure

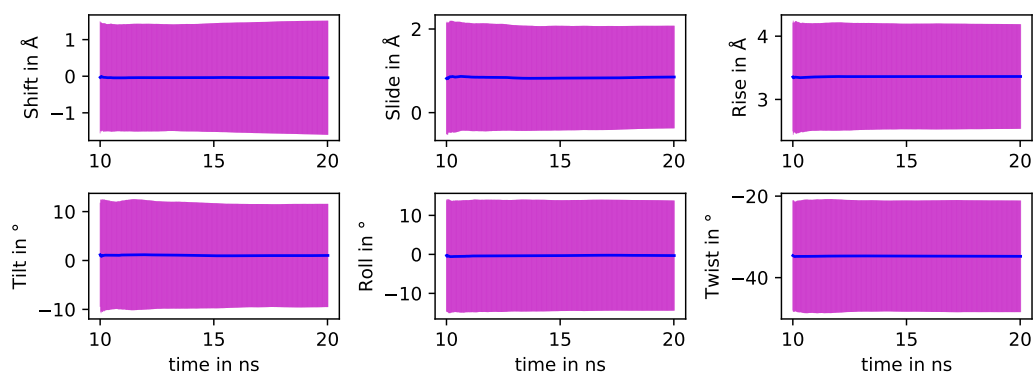


Figure B.21: Helical parameters of the center DS of a microhydrated (micro2) 9HB structure

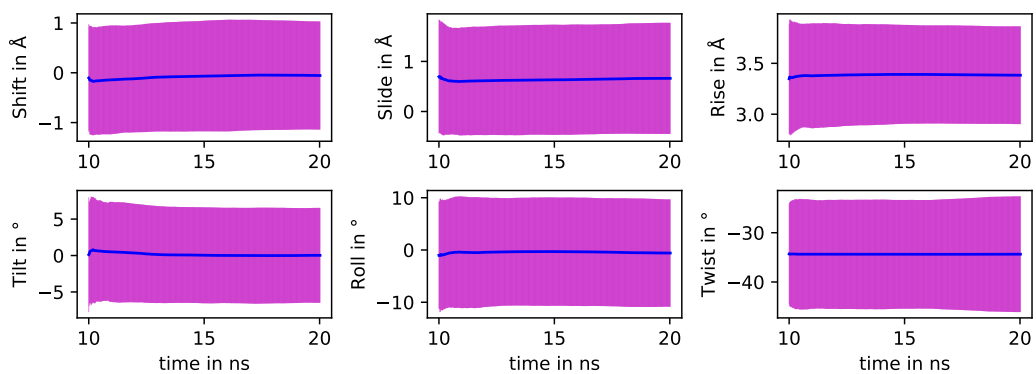


Figure B.22: Helical parameters of the center DS of a microhydrated (micro3) 9HB structure

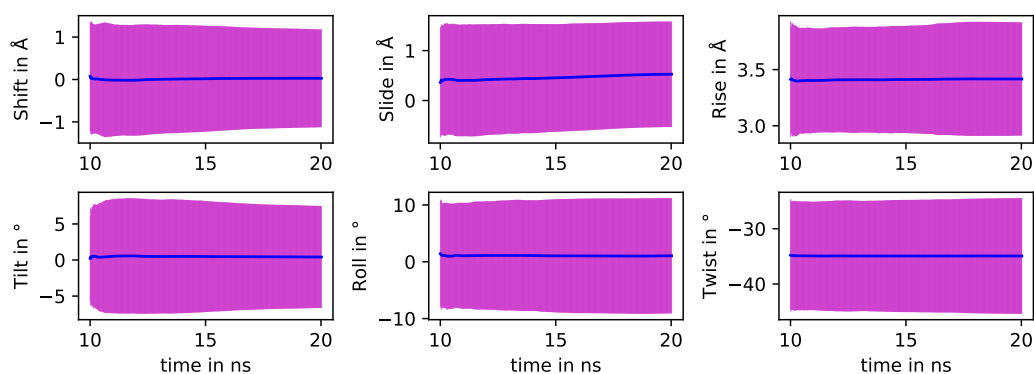


Figure B.23: Helical parameters of the center DS of a microhydrated (micro4) 9HB structure

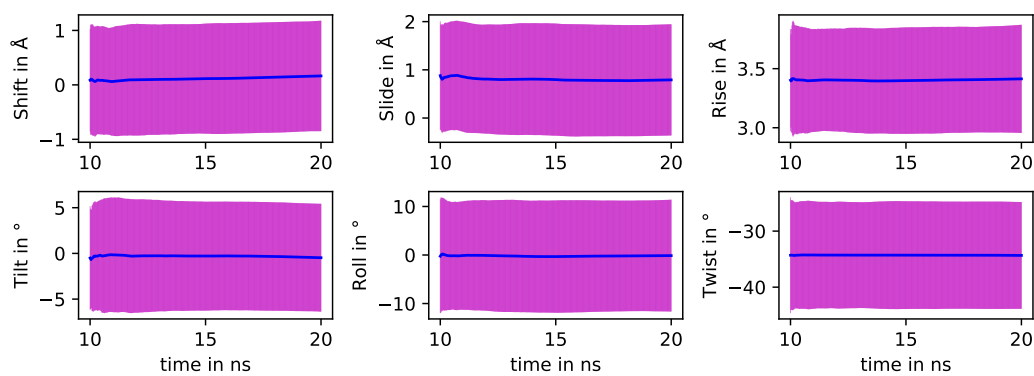


Figure B.24: Helical parameters of the center DS of a microhydrated (micro5) 9HB structure

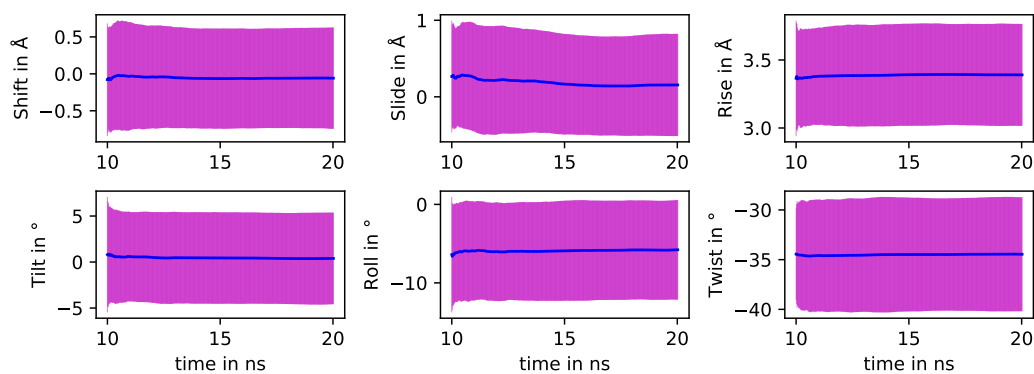


Figure B.25: Helical parameters of the center DS of a fully hydrated 9HB structure

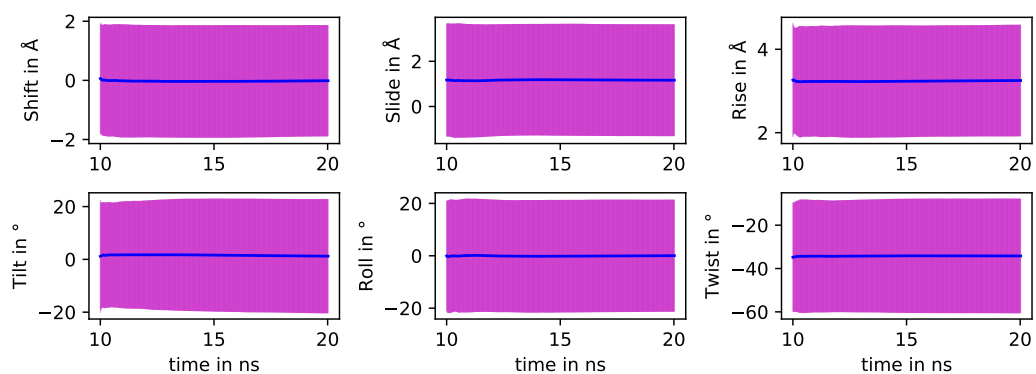


Figure B.26: Helical parameters of the center DS of a microhydrated (micro1) 25HB structure

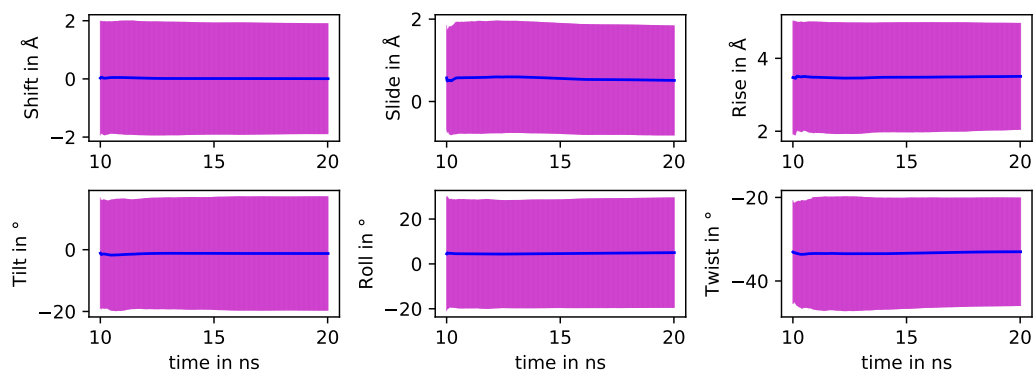


Figure B.27: Helical parameters of the center DS of a microhydrated (micro2) 25HB structure

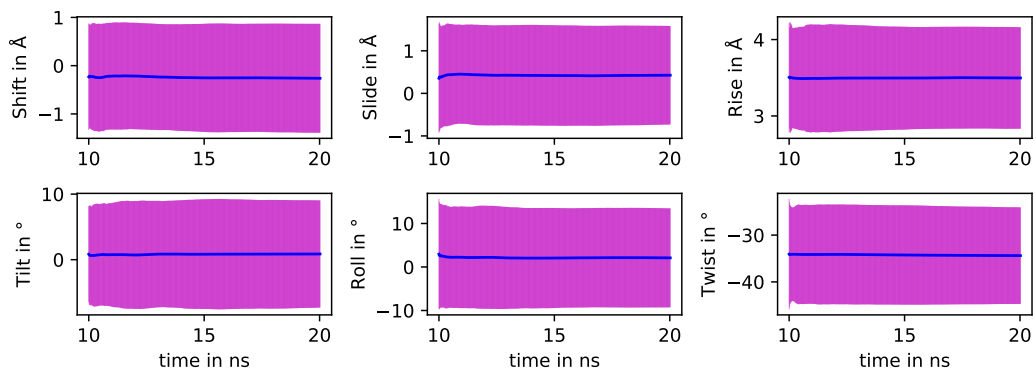


Figure B.28: Helical parameters of the center DS of a microhydrated (micro3) 25HB structure

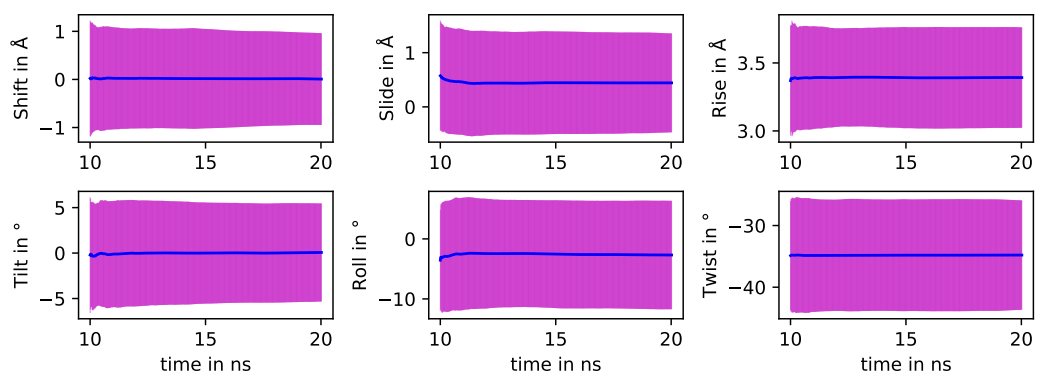


Figure B.29: Helical parameters of the center DS of a microhydrated (micro4) 25HB structure

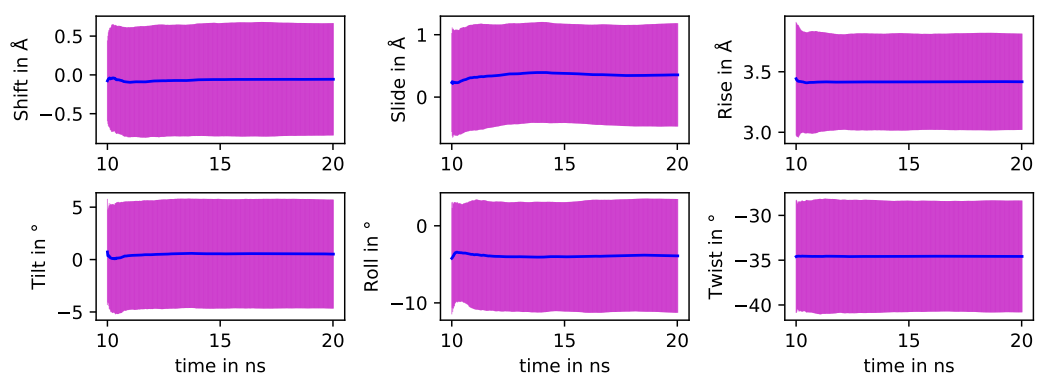


Figure B.30: Helical parameters of the center DS of a microhydrated (micro5) 25HB structure

Bibliography

- [1] *The 2007 Recommendations of the International Commission on Radiological Protection. ICRP publication 103*, volume 37, England, 2007.
- [2] Wendy J. Cannan and David S. Pederson. Mechanisms and Consequences of Double-strand DNA Break Formation in Chromatin. *Journal of Cellular Physiology*, 231(26040249):3–14, January 2016.
- [3] D. D. Eley and D. I. Spivey. Semiconductivity of organic substances. Part 9 - Nucleic acid in the dry state. *Transactions of the Faraday Society*, 58:411–415, 1962.
- [4] Danny Porath, Alexey Bezryadin, Simon de Vries, and Cees Dekker. Direct measurement of electrical transport through DNA molecules. *letters to nature*, 403:635–638, February 2000.
- [5] Hans-Werner Fink and Chrtian Schoeneberger. Electrical conduction through DNA molecules. *Nature*, 398:407–410, April 1999.
- [6] Elizabeth M. Boon and Jacqueline K. Barton. Charge transport in DNA. *Current Opinion in Structural Biology*, 12(3):320–329, June 2002.
- [7] Boleslaw T. Karwowski. The AT Interstrand Cross-Link: Structure, Electronic Properties, and Influence on Charge Transfer in dsDNA. *Molecular therapy. Nucleic acids*, 13:665–685, Dec 2018.

Bibliography

- [8] Erez Braun, Yoav Eichen, Uri Sivan, and Gdalyahu Ben-Yoseph. DNA-templated assembly and electrode attachment of a conducting silver wire. *letters to nature*, 391:775–778, February 1998.
- [9] James P. Lewis, Thomas Cheatham, Evgeni B. Starikov, and Hao Wang. Dynamically Amorphous Character of Electronic States in Poly(dA)-Poly(dT) DNA. *The Journal of Physical Chemistry B*, 107:2581–2587, February 2003.
- [10] Boxuan Shen, Veikko Linko, Hendrik Dietz, and J. Jussi Toppari. Dielectrophoretic trapping of multilayer DNA origami nanostructures and DNA origami-induced local destruction of silicon dioxide. *Electrophoresis*, 36:255–262, Jan 2015.
- [11] S. Kassegne, D. Wibowo, J. Chi, V. Ramesh, A. Narenji, A. Khosla, and J. Mokili. AC electrical characterisation and insight to charge transfer mechanisms in DNA molecular wires through temperature and UV effects. *IET Nanobiotechnology*, 9(3):153–163, 2015.
- [12] A. Yu. Kasumov, D. V. Klinov, P.-E. Roche, S. Guéron, and H. Bouchiat. Thickness and low-temperature conductivity of DNA molecules. *Applied Physics Letters*, 84(6):1007–1009, February 2003.
- [13] S. P. Liu, J. Artois, D. Schmid, M. Wieser, B. Bornemann, S. Weisbrod, A. Marx, E. Scheer, and A. Erbe. Electronic transport through short dsDNA measured with mechanically controlled break junctions: New thiol-gold binding protocol improves conductance. *physica status solidi (b)*, 250(11):2342–2348, 2013.
- [14] J. D. Watson and F. H. C. Crick. Molecular Structure of Nucleic Acids: A Structure for Deoxyribose Nucleic Acid. *Nature*, 171(4356):737–738, 1953.
- [15] Bobo Feng, Robert P. Sosa, Anna K. F. Mårtensson, Kai Jiang, Alex Tong, Kevin D. Dorfman, Masayuki Takahashi, Per Lincoln, Carlos J. Bustamante, Fredrik Westerlund, and Bengt Nordén. Hydrophobic catalysis and a potential biological role of DNA unstacking induced by environment effects. *Proceedings of the National Academy of Sciences of the United States of America*, 116(35):17169, August 2019.
- [16] Anirban Ghosh and Manju Bansal. A glossary of DNA structures from A to Z. *Acta Crystallographica Section D*, 59(4):620–626, Apr 2003.
- [17] R. E. Dickerson. Definitions and nomenclature of nucleic acid structure components. *Nucleic acids research*, 17:1797–803, Mar 1989.

-
- [18] Xiang-Jun Lu and Wilma K. Olson. 3DNA: a software package for the analysis, rebuilding and visualization of three-dimensional nucleic acid structures. *Nucleic acids research*, 31:5108–5121, Sep 2003.
- [19] W. M. Dale. *Direct and indirect effects of ionizing radiations*, chapter I, pages 1–38. Springer Berlin Heidelberg, Berlin, Heidelberg, 1966.
- [20] Clemens von Sonntag. *Free-Radical-Induced DNA Damage and Its Repair*. Springer, Berlin, Heidelberg, 2006.
- [21] Betsy M. Sutherland, Paula V. Bennett, Nela S. Cintron, Peter Guida, and Jacques Laval. Low levels of endogenous oxidative damage cluster levels in unirradiated viral and human DNAs. *Free radical biology & medicine*, 35:495–503, Sep 2003.
- [22] M. E. Lomax, L. K. Folkes, and P. O’Neill. Biological Consequences of Radiation-induced DNA Damage: Relevance to Radiotherapy. *Clinical Oncology*, 25(10):578–585, 2013. Advances in Clinical Radiobiology.
- [23] Lauren C. Colis, Paromita Raychaudhury, and Ashis K. Basu. Mutational specificity of gamma-radiation-induced guanine-thymine and thymine-guanine intrastrand cross-links in mammalian cells and translesion synthesis past the guanine-thymine lesion by human DNA polymerase ϵ . *Biochemistry*, 47:8070–8079, Aug 2008.
- [24] Mark D. Evans, Miral Dizdaroglu, and Marcus S. Cooke. Oxidative DNA damage and disease: induction, repair and significance. *Mutation research*, 567:1–61, Sep 2004.
- [25] Miral Dizdaroglu and Pawel Jaruga. Mechanisms of free radical-induced damage to DNA. *Free radical research*, 46:382–419, Apr 2012.
- [26] Franklin Hutchinson. Chemical Changes Induced in DNA by Ionizing Radiation. In Waldo E. Cohn and Kivie Moldave, editors, *Progress in Nucleic Acid Research and Molecular Biology*, volume 32 of *Progress in Nucleic Acid Research and Molecular Biology*, pages 115–154. Academic Press, 1985.
- [27] Alexandra Teresa Pires Carvalho, Maria Leonor Gouveia, Charan Raju Kanna, Sebastian K. T. S. Wärmländer, Jamie Platts, and Shina Caroline Lynn Kamerlin. Theoretical modelling of epigenetically modified DNA sequences. *F1000 Research*, 4:52, 2015.

Bibliography

- [28] D. D. Eley, G. D. Parfitt, M. J. Perry, and D. H. Taysum. The Semiconductivity Of Organic Substances. Part 1. *Transactions of the Faraday Society*, 49(0):79–86, 1953.
- [29] M. Bixon, Bernd Giese, Stephan Wessely, Thomas Langenbacher, Maria E. Michel-Beyerle, and Joshua Jortner. Long-range charge hopping in DNA. *Proceedings of the National Academy of Sciences of the United States of America*, 96(21):11713, October 1999.
- [30] Keijiro Fukui and Kazuyoshi Tanaka. Distance Dependence of Photoinduced Electron Transfer in DNA. *Angewandte Chemie International Edition*, 37(1):158–161, January 2007.
- [31] Frederick D. Lewis, Taifeng Wu, Yifan Zhang, Robert L. Letsinger, Scott R. Greenfield, and Michael R. Wasielewski. Distance-Dependent Electron Transfer in DNA Hairpins. *Science*, 277(5326):673, August 1997.
- [32] Bernd Giese, Jérôme Amaudrut, Anne-Kathrin Köhler, Martin Spormann, and Stephan Wessely. Direct observation of hole transfer through DNA by hopping between adenine bases and by tunnelling. *Nature*, 412(6844):318–320, July 2001.
- [33] Thierry Douki, Jean-Luc Ravanat, Dimitar Angelov, J. Wagner, and Jean Cadet. *Effects of Duplex Stability on Charge Transfer Efficiency Within DNA*, volume 236, chapter Long-Range Charge Transfer in DNA, pages 127–139. Springer Berlin Heidelberg, 02 2004.
- [34] Shana O. Kelley, R. Erik Holmlin, Eric D. A. Stemp, and Jacqueline K. Barton. Photoinduced Electron Transfer in Ethidium-Modified DNA Duplexes: Dependence on Distance and Base Stacking. *Journal of the American Chemical Society*, 119(41):9861–9870, October 1997.
- [35] Bernd Giese and Stefan Wessely. The Influence of Mismatches on Long-Distance Charge Transport through DNA. *Angewandte Chemie International Edition*, 39(19):3490–3491, 2000.
- [36] Daniel B. Hall and Jacqueline K. Barton. Sensitivity of DNA-Mediated Electron Transfer to the Intervening π -Stack: A Probe for the Integrity of the DNA Base Stack. *Journal of the American Chemical Society*, 119(21):5045–5046, May 1997.
- [37] Susan M. Gasper and Gary B. Schuster. Intramolecular Photoinduced Electron Transfer to Anthraquinones Linked to Duplex DNA: The Effect of Gaps and

- Traps on Long-Range Radical Cation Migration. *Journal of the American Chemical Society*, 119(52):12762–12771, December 1997.
- [38] Yongzhi Kan and Gary B. Schuster. Long-Range Guanine Damage in Single-Stranded DNA: Charge Transport through a Duplex Bridge and in a Single-Stranded Overhang. *Journal of the American Chemical Society*, 121(47):10857–10864, December 1999.
- [39] Michael. Falk, Karl A. Hartman, and R. C. Lord. Hydration of Deoxyribonucleic Acid. I. a Gravimetric Study. *Journal of the American Chemical Society*, 84(20):3843–3846, October 1962.
- [40] N. P. Armitage, M. Briman, and G. Grüner. Charge transfer and charge transport on the double helix. *physica status solidi (b)*, 241(1):69–75, January 2004.
- [41] Christophe Yamahata, Dominique Collard, Tetsuya Takekawa, Momoko Kumemura, Gen Hashiguchi, and Hiroyuki Fujita. Humidity dependence of charge transport through DNA revealed by silicon-based nanotweezers manipulation. *Biophysical journal*, 94(17827222):63–70, January 2008.
- [42] Dong Han Ha, Hyunsoo Nham, Kyung-Hwa Yoo, Hye-mi So, Hae-Yeon Lee, and Tomoji Kawai. Humidity effects on the conductance of the assembly of DNA molecules. *Chemical Physics Letters*, 355(5):405–409, April 2002.
- [43] J. Laudát and F. Laudát. Dielectric study of charge motion in DNA. *European Biophysics Journal*, 21(3):233–239, July 1992.
- [44] Ayumu Terawaki, Yoichi Otsuka, HeaYeon Lee, Takuya Matsumoto, Hidekazu Tanaka, and Tomoji Kawai. Conductance measurement of a DNA network in nanoscale by point contact current imaging atomic force microscopy. *Applied Physics Letters*, 86(11):113901, February 2005.
- [45] S. Tuukkanen, A. Kuzyk, J. J. Toppari, V. P. Hytönen, T. Ihalainen, and P. Törmä. Dielectrophoresis of nanoscale double-stranded DNA and humidity effects on its electrical conductivity. *Applied Physics Letters*, 87(18):183102, 2005.
- [46] K.-H. Yoo, D. H. Ha, J.-O. Lee, J. W. Park, Jinhee Kim, J. J. Kim, H.-Y. Lee, T. Kawai, and Han Yong Choi. Electrical Conduction through Poly(dA)-Poly(dT) and Poly(dG)-Poly(dC) DNA Molecules. *Physical Review Letters*, 87(19):198102, October 2001.

Bibliography

- [47] Mario Wolter, Marcus Elstner, and Tomas Kubar. Charge transport in desolvated DNA. *The Journal of chemical physics*, 139:125102, September 2013.
- [48] Y. L. Lyubchenko, P. I. Oden, D. Lampner, S. M. Lindsay, and K. A. Dunker. Atomic force microscopy of DNA and bacteriophage in air, water and propanol: the role of adhesion forces. *Nucleic acids research*, 21(8464697):1117–1123, March 1993.
- [49] M. M. R. Howlader A U Alam and M. J. Deen. The effects of oxygen plasma and humidity on surface roughness, water contact angle and hardness of silicon, silicon dioxide and glass. *Journal of Micromechanics and Microengineering*, 24(3), 2014.
- [50] Kohki Kawane, Kou Motani, and Shigekazu Nagata. DNA Degradation and Its Defects. *Cold Spring Harbor Perspectives in Biology*, 6(6), 2014.
- [51] H. Yamaguchi, J.-G. Siebers, A. Furukawa, N. Otagiri, and R. Osman. Molecular Dynamics Simulation of a DNA Containing a Single Strand Break. *Radiation Protection Dosimetry*, 99(1-4):103–108, 06 2002.
- [52] Juraj Kotulic Bunta, Aatto Laaksonen, Miroslav Pinak, and Toshiyuki Nemoto. DNA strand break: Structural and electrostatic properties studied by molecular dynamics simulation. *Computational Biology and Chemistry*, 30(2):112–119, 2006.
- [53] John Jr SantaLucia and Donald Hicks. The thermodynamics of DNA structural motifs. *Annual review of biophysics and biomolecular structure*, 33:415–440, 2004.
- [54] David Becker, Amanda Bryant-Friedrich, CherylAnn Trzasko, and Michael D. Sevilla. Electron Spin Resonance Study of DNA Irradiated with an Argon Ion Beam: Evidence for Formation of Sugar Phosphate Backbone Radicals. *Radiation Research*, 160(2):174–185, 2003.
- [55] Alexandra T. P. Carvalho, Leonor Gouveia, Charan Raju Kanna, Sebastian K. T. S. Wärmländer, Jamie A. Platts, and Shina Caroline Lynn Kamerlin. Understanding the structural and dynamic consequences of DNA epigenetic modifications: computational insights into cytosine methylation and hydroxymethylation. *Epigenetics*, 9:1604–1612, Dec 2014.
- [56] Kazuhiko Nakatani and Isao Saito. *Charge Transport in Duplex DNA Containing Modified Nucleotide Bases*, chapter Long-Range Charge Transfer in DNA I, pages 163–186. Springer Berlin Heidelberg, Berlin, Heidelberg, 2004.

-
- [57] K. Schneider and B. T. Chait. Increased stability of nucleic acids containing 7-deaza-guanosine and 7-deaza-adenosine may enable rapid DNA sequencing by matrix-assisted laser desorption mass spectrometry. *Nucleic acids research*, 23:1570–1575, May 1995.
- [58] Miroslav Pinak. Enzymatic recognition of radiation-produced oxidative DNA lesion. Molecular dynamics approach. In Evgeni B. Starikov, James P. Lewis, and Shigenori Tanaka, editors, *Modern Methods for Theoretical Physical Chemistry of Biopolymers*, pages 191–210. Elsevier Science, Amsterdam, 2006.
- [59] Chunang Gu and Yinsheng Wang. LC-MS/MS identification and yeast polymerase eta bypass of a novel gamma-irradiation-induced intrastrand cross-link lesion G[8-5]C. *Biochemistry*, 43:6745–6750, Jun 2004.
- [60] Yurui Xue, Xun Li, Hongbin Li, and Wenke Zhang. Quantifying thiol-gold interactions towards the efficient strength control. *Nature Communications*, 5(1):4348, July 2014.
- [61] N. Kang, A. Erbe, and E. Scheer. Electrical characterization of DNA in mechanically controlled break-junctions. *New Journal of Physics*, 10(2):023030, feb 2008.
- [62] Huijuan Zhang, Wei Xu, Xiaogang Liu, Francesco Stellacci, and John T. L. Thong. Capturing a DNA duplex under near-physiological conditions. *Applied Physics Letters*, 97(16):163702, 2010.
- [63] Linette M. Demers, Mattias Ostblom, Hua Zhang, Nak-Han Jang, Bo Liedberg, and Chad A. Mirkin. Thermal desorption behavior and binding properties of DNA bases and nucleosides on gold. *Journal of the American Chemical Society*, 124:11248–11249, Sep 2002.
- [64] Aric Opdahl, Dmitri Y. Petrovykh, Hiromi Kimura-Suda, Michael J. Tarlov, and Lloyd J. Whitman. Independent control of grafting density and conformation of single-stranded DNA brushes. *Proceedings of the National Academy of Sciences of the United States of America*, 104:9–14, Jan 2007.
- [65] Sarah M. Schreiner, David F. Shudy, Anna L. Hatch, Aric Opdahl, Lloyd J. Whitman, and Dmitri Y. Petrovykh. Controlled and Efficient Hybridization Achieved with DNA Probes Immobilized Solely through Preferential DNA-Substrate Interactions. *Analytical Chemistry*, 82(7):2803–2810, April 2010.
- [66] Sarah M. Schreiner, Anna L. Hatch, David F. Shudy, David R. Howard, Caitlin Howell, Jianli Zhao, Patrick Koelsch, Michael Zharnikov, Dmitri Y. Petrovykh,

Bibliography

- and Aric Opdahl. Impact of DNA-Surface Interactions on the Stability of DNA Hybrids. *Analytical Chemistry*, 83(11):4288–4295, June 2011.
- [67] D. M. Lilley. Structures of helical junctions in nucleic acids. *Quarterly reviews of biophysics*, 33:109–59, May 2000.
- [68] Prakash Shrestha, Tomoko Emura, Deepak Koirala, Yunxi Cui, Kumi Hidaka, William J. Maximuck, Masayuki Endo, Hiroshi Sugiyama, and Hanbin Mao. Mechanical properties of DNA origami nanoassemblies are determined by Holliday junction mechanophores. *Nucleic acids research*, 44(27387283):6574–6582, August 2016.
- [69] Richard P. Fahlman, Rajendra D. Sharma, and Dipankar Sen. The Charge Conduction Properties of DNA Holliday Junctions Depend Critically on the Identity of the Tethered Photooxidant. *Journal of the American Chemical Society*, 124(42):12477–12485, October 2002.
- [70] D. T. Odom, E. A. Dill, and J. K. Barton. Charge transport through DNA four-way junctions. *Nucleic acids research*, 29:2026–33, May 2001.
- [71] M. Ortiz-Lombardía, A. Gonzalez, R. Eritja, J. Aymami, F. Azorin, and M. Coll. Crystal structure of a DNA Holliday junction. *Nature structural biology*, 6:913–917, Oct 1999.
- [72] Brandt F. Eichman, Miguel Ortiz-Lombardía, Joan Aymami, Miquel Coll, and Pui Shing Ho. The Inherent Properties of DNA Four-way Junctions: Comparing the Crystal Structures of Holliday Junctions. *Journal of Molecular Biology*, 320(5):1037–1051, 2002.
- [73] Herbert A. Pohl. The Motion and Precipitation of Suspensoids in Divergent Electric Fields. *Journal of Applied Physics*, 22(7):869–871, 1951.
- [74] Ronald Pethig. *The Clausius-Mossotti Factor*, chapter 6, pages 119–144. John Wiley & Sons, Ltd, 2017.
- [75] Richard W. Clarke, Joe D. Piper, Liming Ying, and David Klenerman. Surface conductivity of biological macromolecules measured by nanopipette dielectrophoresis. *Physical review letters*, 98:198102, May 2007.
- [76] A. Castellanos, A. Ramos, A. González, N. G. Green, and H. Morgan. Electrohydrodynamics and dielectrophoresis in microsystems: scaling laws. *Journal of Physics D: Applied Physics*, 36(20):2584–2597, oct 2003.

-
- [77] H. Helmholtz. Über einige Gesetze der Vertheilung elektrischer Ströme in körperlichen Leitern mit Anwendung auf die thierisch-elektrischen Versuche. *Annalen der Physik*, pages 211–233, January 1853.
- [78] Green, Ramos, Gonzalez, Morgan, and Castellanos. Fluid flow induced by nonuniform ac electric fields in electrolytes on microelectrodes. I. Experimental measurements. *Physical review. E, Statistical physics, plasmas, fluids, and related interdisciplinary topics*, 61:4011–8, Apr 2000.
- [79] Jie Wu, Yuxing Ben, and Hsueh-Chia Chang. Particle detection by electrical impedance spectroscopy with asymmetric-polarization AC electroosmotic trapping. *Microfluidics and Nanofluidics*, 1:161–167, 05 2005.
- [80] Kimmo Laitinen. Fluid dynamics in DEP trapping of DNA origamis and their functionalization. Master’s thesis, University of Jvaskylä, April 2009.
- [81] Otto Stern. Zur Theorie der elektrolytischen Doppelschicht. *Zeitschrift für Elektrochemie und angewandte physikalische Chemie*, 30(21):508–516, 1924.
- [82] L. D. Landau and E. M. Lifshitz. *Fluid Mechanics*. Pergamon Press, 1987.
- [83] A. Ramos, H. Morgan, N. G. Green, and A. Castellanos. Ac electrokinetics: a review of forces in microelectrode structures. *Journal of Physics D: Applied Physics*, 31(18):2338–2353, sep 1998.
- [84] Mostafa H. Sharqawy. New correlations for seawater and pure water thermal conductivity at different temperatures and salinities. *Desalination*, 313:97–104, 2013.
- [85] P. D. Grossman and J. C. Colburn. *Capillary Electrophoresis: Theory and Practice*. Academic Press, 1992.
- [86] Errol G. Lewars. *Computational Chemistry*. Springer, third edition, 2016.
- [87] Thomas P. Senftle, Sungwook Hong, Md Mahbubul Islam, Sudhir B. Kylasa, Yuanxia Zheng, Yun Kyung Shin, Chad Junkermeier, Roman Engel-Herbert, Michael J. Janik, Hasan Metin Aktulga, Toon Verstraelen, Ananth Grama, and Adri C. T. van Duin. The ReaxFF reactive force-field: development, applications and future directions. *npj Computational Materials*, 2(1):15011, 2016.
- [88] Ulrich Essmann, Lalith Perera, Max L. Berkowitz, Tom Darden, Hsing Lee, and Lee G. Pedersen. A smooth particle mesh Ewald method. *The Journal of Chemical Physics*, 103(19):8577–8593, 1995.

Bibliography

- [89] Loup Verlet. Computer "Experiments" on Classical Fluids. I. Thermodynamical Properties of Lennard-Jones Molecules. *Physical Review*, 159:98–103, Jul 1967.
- [90] David Fincham. Choice of timestep in molecular dynamics simulation. *Computer Physics Communications*, 40(2):263–269, 1986.
- [91] H. J. C. Berendsen, J. P. M. Postma, W. F. van Gunsteren, A. DiNola, and J. R. Haak. Molecular dynamics with coupling to an external bath. *The Journal of Chemical Physics*, 81(8):3684–3690, 1984.
- [92] Paul W. K. Rothemund. Folding DNA to create nanoscale shapes and patterns. *Nature*, 440(7082):297–302, March 2006.
- [93] Anqin Xu, John N. Harb, Mauri A. Kostianen, William L. Hughes, Adam T. Woolley, Haitao Liu, and Ashwin Gopinath. DNA origami: The bridge from bottom to top. *MRS Bulletin*, 42(12), 2017.
- [94] Mengyu Zhao, Yahong Chen, Kexin Wang, Zhaoxuan Zhang, Jason K. Streit, Jeffrey A. Fagan, Jianshi Tang, Ming Zheng, Chaoyong Yang, Zhi Zhu, and Wei Sun. DNA-directed nanofabrication of high-performance carbon nanotube field-effect transistors. *Science*, 368(6493):878–881, 2020.
- [95] Jakob Bach Knudsen, Lei Liu, Anne Louise Bank Kodal, Mikael Madsen, Qiang Li, Jie Song, Johannes B. Woehrstein, Shelley F. J. Wickham, Maximilian T. Strauss, Florian Schueder, Jesper Vinther, Abhichart Krisanaprasit, Daniel Gudnason, Anton Allen Abbotsford Smith, Ryosuke Ogaki, Alexander N. Zelikin, Flemming Besenbacher, Victoria Birkedal, Peng Yin, William M. Shih, Ralf Jungmann, Mingdong Dong, and Kurt V. Gothelf. Routing of individual polymers in designed patterns. *Nature Nanotechnology*, 10(10):892–898, 2015.
- [96] JÃCergen J. Schmied, Andreas Gietl, Phil Holzmeister, Carsten Forthmann, Christian Steinhauer, Thorben Dammeyer, and Philip Tinnefeld. Fluorescence and super-resolution standards based on DNA origami. *Nature Methods*, 9(12):1133–1134, 2012.
- [97] Nathan D. Williams, Ane Landajuela, Ravi Kiran Kasula, Wenjiao Zhou, John T. Powell, Zhiqun Xi, Farren J. Isaacs, Julien Berro, Derek Toomre, Erdem Karatekin, and Chenxiang Lin. DNA-Origami-Based Fluorescence Brightness Standards for Convenient and Fast Protein Counting in Live Cells. *Nano Letters*, 20(12):8890–8896, December 2020.

- [98] Sarah E. Ochmann, Carolin Vietz, Kateryna Trofymchuk, Guillermo P. Acuna, Birka Lalkens, and Philip Tinnefeld. Optical Nanoantenna for Single Molecule-Based Detection of Zika Virus Nucleic Acids without Molecular Multiplication. *Analytical Chemistry*, 89(23):13000–13007, December 2017.
- [99] Youngeun Choi, Carsten Schmidt, Philip Tinnefeld, Ilko Bald, and Stefan Rädiger. A new reporter design based on DNA origami nanostructures for quantification of short oligonucleotides using microbeads. *Scientific Reports*, 9(1):4769, 2019.
- [100] Petteri Piskunen, Boxuan Shen, Sofia Julin, Heini Ijäs, J. Jussi Toppari, Mauri A. Kostianen, and Veikko Linko. DNA Origami-Mediated Substrate Nanopatterning of Inorganic Structures for Sensing Applications. *JoVE*, (151):e60313, 2019.
- [101] Guillaume Thomas, Cheikh Tidiane Diagne, Xavier Baillin, Thierry Chevolleau, Thomas Charvolin, and Raluca Tiron. DNA Origami for Silicon Patterning. *ACS Applied Materials & Interfaces*, 12(32):36799–36809, August 2020.
- [102] Cheikh Tidiane Diagne, Christophe Brun, Didier Gasparutto, Xavier Baillin, and Raluca Tiron. DNA Origami Mask for Sub-Ten-Nanometer Lithography. *ACS Nano*, 10(7):6458–6463, July 2016.
- [103] Shawn M. Douglas, Adam H. Marblestone, Surat Teerapittayanon, Alejandro Vazquez, George M. Church, and William M. Shih. Rapid prototyping of 3D DNA-origami shapes with caDNAno. *Nucleic Acids Research*, 37(15):5001–5006, June 2009.
- [104] Jürgen J. Schmied, Mario Raab, Carsten Forthmann, Enrico Pibiri, Bettina Wünsch, Thorben Dammeyer, and Philip Tinnefeld. DNA origami-based standards for quantitative fluorescence microscopy. *Nature Protocols*, 9(6):1367–1391, June 2014.
- [105] Th. Weimann, H. Scherer, H. Wolf, V. A. Krupenin, and J. Niemeyer. A new technology for metallic multilayer single electron tunneling devices. *Microelectronic Engineering*, 41-42:559–562, 1998. International Conference on Micro- and Nanofabrication.
- [106] Ana Cuervo, Pablo D. Dans, José L. Carrascosa, Modesto Orozco, Gabriel Gomila, and Laura Fumagalli. Direct measurement of the dielectric polarization properties of DNA. *Proc Natl Acad Sci USA*, 111(35):E3624, September 2014.

Bibliography

- [107] Sampo Tuukkanen, Anton Kuzyk, Jussi Toppari, Hannu Häkkinen, Vesa Hytönen, Einari Niskanen, Marcus Rinkiö, and Päivi Törmä. Trapping of 27 bp-8 kbp DNA and immobilization of thiol-modified DNA using dielectrophoresis. *Nanotechnology*, 18(29):295204, June 2007.
- [108] Thermo Scientific, IC Controls. *Conductivity measurements in high purity water samples below 10 μ Siemens/cm*, 2012.
- [109] Hugo L. Bianchi, Horacio R. Corti, and Roberto Fernandez-Prini. The Conductivity of Dilute Aqueous Solutions of Magnesium Chloride at 25 $\hat{\text{A}}^{\circ}\text{C}$. *Journal of Solution Chemistry*, 17(11), November 1988.
- [110] C. G. Malmberg and A. A. Maryott. Dielectric Constant of Water from 0 $\hat{\text{A}}^{\circ}\text{C}$ to 100 $\hat{\text{A}}^{\circ}\text{C}$. *Journal of Research of the National Bureau of Standards*, 56(1), January 1956.
- [111] Nir Gavish and Keith Promislow. Dependence of the dielectric constant of electrolyte solutions on ionic concentration: A microfield approach. *Physical Review E*, 2016.
- [112] D. Wibowo. DNA molecular wire-based nanoelectronics: New insight and high frequency AC electrical characterization. Master's thesis, San Diego State University, 2014.
- [113] Xu Zhang, Tony Gouriye, Kristian Göeken, Mark R. Servos, Ron Gill, and Juewen Liu. Toward Fast and Quantitative Modification of Large Gold Nanoparticles by Thiolated DNA: Scaling of Nanoscale Forces, Kinetics, and the Need for Thiol Reduction. *Journal of Physical Chemistry C*, 117(30):15677–15684, August 2013.
- [114] Thermo Fisher Scientific. *Rapid DNA Ligation Kit*, 2020.
- [115] New England Biolabs. *Lambda DNA*, 2020.
- [116] Biozym Scientific. *End-It DNA End-Repair Kit*, 2020.
- [117] I. R. Lehman. DNA Ligase: Structure, Mechanism, and Function. *Science*, 186(4166):790–797, 1974.
- [118] C. R. Cosens. A balance-detector for alternating-current bridges. *Proceedings of the Physical Society*, 46(6):818–823, nov 1934.
- [119] Walter C. Michels and Norma L. Curtis. A Pentode Lock-In Amplifier of High Frequency Selectivity. *Review of Scientific Instruments*, 12(9):444–447, 1941.

-
- [120] Zurich Instruments. Principles of lock-in detection and the state of the art. White Paper, 2016.
- [121] Bert Voigtlaender. *Scanning Probe Microscopy*. Springer-Verlag Berlin Heidelberg, 2015.
- [122] Gianaurelio Cuniberti, Luis Craco, Danny Porath, and Cees Dekker. Backbone-induced semiconducting behavior in short DNA wires. *Physical Review B*, 65:241314, Jun 2002.
- [123] Keysight Technologies Inc., Santa Rosa, California. *33210A Waveform/Function Generator*.
- [124] Ametek (R) Scientific Instruments. *7230 General Purpose DSP Lock-in Amplifier*.
- [125] Zurich Instruments AG, Zurich, Switzerland. *MFLI 500 kHz / 5 MHz Lock-in Amplifier*.
- [126] SPECS Surface nano Analysis GmbH, Voltastrasse 5, 13355 Berlin / Germany. *EQ 22/35 Electron Source*, 2020.
- [127] James F. Ziegler, M. D. Ziegler, and J. P. Biersack. SRIM - The stopping and range of ions in matter. *Nuclear Instruments and Methods in Physics Research Section B: Beam Interactions with Materials and Atoms*, 268:1818–1823, 2010.
- [128] Klaus-D. Greif, Hein J. Brede, Dieter Frankenberg, and Ulrich Giesen. The PTB single ion microbeam for irradiation of living cells. *Nuclear Instruments and Methods in Physics Research Section B: Beam Interactions with Materials and Atoms*, 217(3):505–512, 2004.
- [129] Florian Heimbach, Alexander Arndt, Heidi Nettelbeck, Frank Langner, Ulrich Giesen, Hans Rabus, Stefan Sellner, J. Toppari, Boxuan Shen, and Woon Yong Baek. Measurement of changes in impedance of DNA nanowires due to radiation induced structural damage: A novel approach for a DNA-based radiosensitive device. *The European Physical Journal D*, 71, 08 2017.
- [130] Zahra Ahmadi Ganjeh, Mohammad Eslami-Kalantari, Mahdy Ebrahimi Loushab, and Ali Asghar Mowlavi. Simulation of direct DNA damages caused by alpha particles versus protons. *Nuclear Instruments and Methods in Physics Research Section B: Beam Interactions with Materials and Atoms*, 473:10–15, June 2020.

Bibliography

- [131] J. Stroud. Make-NA Server. <http://structure.usc-edu/make-na/server.html>, 2019.
- [132] H. J. C. Berendsen, J. R. Grigera, and T. P. Straatsma. The missing term in effective pair potentials. *The Journal of Physical Chemistry A*, 91(24):6269–6271, November 1987.
- [133] Alexander D. MacKerell Jr., Nilesh Banavali, and Nicolas Foloppe. Development and current status of the CHARMM force field for nucleic acids. *Biopolymers*, 56(4):257–265, 2000.
- [134] Berk Hess, Henk Bekker, Herman J. C. Berendsen, and Johannes G. E. M. Fraaije. LINCS: A linear constraint solver for molecular simulations. *Journal of Computational Chemistry*, 18(12):1463–1472, 1997.
- [135] Giovanni Bussi, Davide Donadio, and Michele Parrinello. Canonical sampling through velocity rescaling. *The Journal of chemical physics*, 126:014101, Jan 2007.
- [136] M. Parrinello and A. Rahman. Crystal Structure and Pair Potentials: A Molecular-Dynamics Study. *Physical Review Letters*, 45:1196–1199, Oct 1980.
- [137] M. Guéron and G. Weisbuch. Polyelectrolyte theory. I. Counterion accumulation, site-binding, and their insensitivity to polyelectrolyte shape in solutions containing finite salt concentrations. *Biopolymers*, 19(2):353–382, 1980.
- [138] J. Conrad, M. Troll, and B. H. Zimm. Ions around DNA: Monte Carlo estimates of distribution with improved electrostatic potentials. *Biopolymers*, 27:1711–1732, Nov 1988.
- [139] Zhi-Jie Tan and Shi-Jie Chen. Nucleic acid helix stability: effects of salt concentration, cation valence and size, and chain length. *Biophysical journal*, 90(16299077):1175–1190, February 2006.
- [140] Mario Wolter, Marcus Elstner, and Tomáš Kubař. On the Structure and Stretching of Microhydrated DNA. *Journal of Physical Chemistry*, 115(41):11238–11247, October 2011.
- [141] Christophe Blanchet, Marco Pasi, Krystyna Zakrzewska, and Richard Lavery. CURVES+ web server for analyzing and visualizing the helical, backbone and groove parameters of nucleic acid structures. *Nucleic acids research*, 39(21558323):W68–W73, July 2011.

-
- [142] O. F. Borisova, A. K. Shchyolkina, B. K. Chernov, and N. A. Tchurikov. Relative stability of AT and GC pairs in parallel DNA duplex formed by a natural sequence. *FEBS Letters*, 322(3):304–306, 1993.
- [143] M. Semenov, T. Bolbukh, and V. Maleev. Infrared study of the influence of water on DNA stability in the dependence on AT/GC composition. *Journal of Molecular Structure*, 408-409:213–217, 1997. *Molecular Spectroscopy and Molecular Structure 1996*.
- [144] Anna K. Shchyolkina, Olga F. Borisova, Michael A. Livshits, Galina E. Pozmogova, Boris K. Chernov, Reinhard Klement, and Thomas M. Jovin. Parallel-Stranded DNA with Mixed AT/GC Composition: Role of trans G \ddot{A} · C Base Pairs in Sequence Dependent Helical Stability. *Biochemistry*, 39(33):10034–10044, August 2000.
- [145] Linda A. Zotti, Thomas Kirchner, Juan-Carlos Cuevas, Fabian Pauly, Thomas Huhn, Elke Scheer, and Artur Erbe. Revealing the Role of Anchoring Groups in the Electrical Conduction Through Single-Molecule Junctions. *Small*, 6(14):1529–1535, 2010.
- [146] Nandhini Ponnuswamy, Maartje M. C. Bastings, Bhavik Nathwani, Ju Hee Ryu, Leo Y. T. Chou, Mathias Vinther, Weiwei Aileen Li, Frances M. Anastassacos, David J. Mooney, and William M. Shih. Oligolysine-based coating protects DNA nanostructures from low-salt denaturation and nuclease degradation. *Nature communications*, 8:15654, May 2017.
- [147] Saminathan Ramakrishnan, Georg Krainer, Guido Grundmeier, Michael Schlierf, and Adrian Keller. Cation-Induced Stabilization and Denaturation of DNA Origami Nanostructures in Urea and Guanidinium Chloride. *Small*, 13(44):1702100, 2017.
- [148] Hyojeong Kim, Sumedh P. Surwade, Anna Powell, Christina O’Donnell, and Haitao Liu. Stability of DNA Origami Nanostructure under Diverse Chemical Environments. *Chemistry of Materials*, 26(18):5265–5273, September 2014.
- [149] Charlotte Kielar, Yang Xin, Boxuan Shen, Mauri A. Kostianen, Guido Grundmeier, Veikko Linko, and Adrian Keller. On the Stability of DNA Origami Nanostructures in Low-Magnesium Buffers. *Angewandte Chemie International Edition*, 57(30):9470–9474, January 2020.
- [150] Veikko Linko, Boxuan Shen, Kosti Tapio, J. Jussi Toppari, Mauri A. Kos-

Bibliography

tiainen, and Sampo Tuukkanen. One-step large-scale deposition of salt-free DNA origami nanostructures. *Scientific Reports*, 5(1):15634, October 2015.

Danksagung

An dieser Stelle möchte ich mich bei allen bedanken, die zur erfolgreichen Fertigstellung dieser Arbeit beigetragen haben. Zum einen meinem Doktorvater Philip Tinnefeld von der LMU und meinen Betreuern hier an der PTB Woon Yong Baek und Ulrich Giesen. Außerdem möchte ich Hans Rabus danken, der dieses Projekt ermöglicht hat. Grundsätzlich gilt mein Dank allen Mitarbeitern des Fachbereichs 6.5 der PTB. Besonders hervorheben möchte ich davon Heike Nittmann, die mir viele experimentelle Arbeiten abgenommen hat. Auch meinem ehemaligen PTB Kollegen Alexander Arndt, der mir vor allem in der Anfangszeit viele Hilfestellungen gegeben hat, möchte ich an dieser Stelle danken. Weitere PTB Mitarbeiter, denen ich gerne für ihre Unterstützung danken möchte sind Alexander Ruhz, Frank Pohlenz, Thomas Weimann, Peter Hinze und Amado Bautista, sowie meinen Freunden und Kollegen Marion Bug und Johannes Rahm. Von der Tinnefeld Gruppe möchte ich mich bei Johann Bohlen bedanken und auch bei Izabela Kaminska, die mittlerweile an der polnischen Akademie der Wissenschaften tätig ist. Für ihre großartige Unterstützung bezüglich des DEP Einfangs möchte ich mich auch bei meinen finnischen Kollegen Jussi Toppari und Kosti Tapio bedanken. Und natürlich möchte ich nicht zuletzt all meinen Freunden und meiner Familie, die mir in dieser Zeit zur Seite gestanden sind, meinen herzlichen Dank aussprechen.